

INFORMATION TO USERS

This manuscript has been reproduced from the microfilm master. UMI films the text directly from the original or copy submitted. Thus, some thesis and dissertation copies are in typewriter face, while others may be from any type of computer printer.

The quality of this reproduction is dependent upon the quality of the copy submitted. Broken or indistinct print, colored or poor quality illustrations and photographs, print bleedthrough, substandard margins, and improper alignment can adversely affect reproduction.

In the unlikely event that the author did not send UMI a complete manuscript and there are missing pages, these will be noted. Also, if unauthorized copyright material had to be removed, a note will indicate the deletion.

Oversize materials (e.g., maps, drawings, charts) are reproduced by sectioning the original, beginning at the upper left-hand corner and continuing from left to right in equal sections with small overlaps. Each original is also photographed in one exposure and is included in reduced form at the back of the book.

Photographs included in the original manuscript have been reproduced xerographically in this copy. Higher quality 6" x 9" black and white photographic prints are available for any photographs or illustrations appearing in this copy for an additional charge. Contact UMI directly to order.

U·M·I

University Microfilms International
A Bell & Howell Information Company
300 North Zeeb Road, Ann Arbor, MI 48106-1346 USA
313/761-4700 800/521-0600

Order Number 9410838

The influence of dust on the absorptivity of radiant barriers

Noboa, Homero Luis, Ph.D.

Texas A&M University, 1993

U·M·I
300 N. Zeeb Rd.
Ann Arbor, MI 48106

**THE INFLUENCE OF DUST ON THE ABSORPTIVITY OF RADIANT
BARRIERS**

A Dissertation

by

HOMERO LUIS NOBOA

Submitted to the Office of Graduate Studies of
Texas A&M University
in partial fulfillment of the requirements for the degree of

DOCTOR OF PHILOSOPHY

December 1993

Major Subject: Mechanical Engineering

**THE INFLUENCE OF DUST ON THE ABSORPTIVITY OF RADIANT
BARRIERS**

A Dissertation

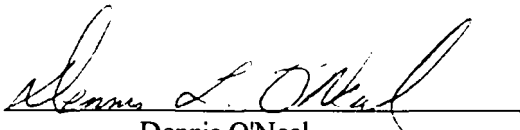
by

HOMERO LUIS NOBOA

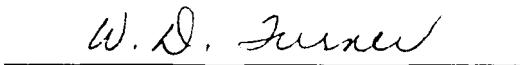
Submitted to Texas A&M University
in partial fulfillment of the requirements
for the degree of

DOCTOR OF PHILOSOPHY

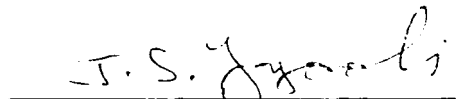
Approved as to style and content by



Dennis O'Neal
(Chair of Committee)



W. D. Turner
(Member)



Jamal Seyed-Yagoobi
(Member)



Larry D. Degelman
(Member)



for G. P. Peterson
(Head of Department)

December 1993

Major Subject: Mechanical Engineering

ABSTRACT

The Influence of Dust on the Absorptivity of Radiant Barriers. (December 1993)

Homero Luis Noboa, Eng., Escuela Politécnica Nacional;

M. S., Texas A&M University

Chair of Advisory Committee: Dr. Dennis O'Neal

The purpose of this project was to model and quantify the increase of the absorptivity of radiant barriers caused by the accumulation of dust on the surface of radiant barriers.

This research was the continuation of a previous work by the author at Texas A&M University in which a radiation energy balance inside the attic enclosure was developed. The particles were considered as flat, circular planes, all having the same radii. That early model showed that there was a linear relationship between the fraction of area of the foil covered by dust and the mean absorptivity of the dusty radiant barrier.

In the present work, it was found that the assumption of treating the dust particles as plane circles, underestimated the effective area of the particles by about 20 %. Experimental measurements indicated that dust particles achieved the same temperature as the radiant barrier.

The new model used the linear relationship just described, and simulated the dust particles as flat circular planes having random radii and laying in random locations within the radiant barrier surface.

The new model calculated the fraction of radiant barrier area covered by particles using a digital array in which the clean barrier was represented as zeroes and the dust particles were represented as a set of ones appropriately dimensioned inside the array.

The experimentation used natural dust and Arizona Road Test Dust. Using an infrared emissometer, the emissivities (absorptivities) of the clean and dusty barriers were measured and using an electronic scale, the dust loading was measured.

An electron microscope was used to experimentally find the fraction of radiant barrier covered by the dust particles to correlate the experimentally found absorptivity with the experimentally found fraction of dust coverage.

The limited experimental data available were also used to correlate the absorptivity of the dusty radiant barrier with the time of dust accumulation and the location of the barrier inside the attic. A linear relationship between the absorptivity and the time of dust accumulation was found that can be applied to predict future barrier effectiveness based upon the rate of dust accumulation for a given location.

To my beloved Monina de mi Corazón.

To my beloved parents.

To Anita and Felipe.

To my in-laws.

ACKNOWLEDGMENTS

My first thoughts of gratitude are to my God, from Whom I received the wisdom and courage to make this work and who let me find Dr. Dennis O'Neal as my advisor. Dr. O'Neal's guidance, encouragement, and hard work have made it possible for me to complete this work in the very short time frame set for it, for what I am in perpetual gratitude. I express my thanks to Dr. W. D. Turner for his help and advise through the development of this work. It has been my pleasure to have him as member of my graduate committee. I also express my thanks to Dr. Jamal Seyed-Yagoobi, Dr. Larry Degelman and Dr. David Ellis for serving as members of my graduate committee; their suggestions were very helpful for my work.

Only my love could, if possible, repay the effort and sacrifice that my beloved wife has endured during all these years. She made the lives of all the members of my family shine with love and care. Her understanding and encouragement were the tools I used to overcome the problems and frustrations in the work.

I express my gratitude to my parents who always supported me and gave me love from the distance, to my beloved children Anita Maria and Felipe Homero, who reminded me of how good it is to laugh and how important it is, from time to time, to stop and smell the flowers of the road, and to my in-laws whose support and love were always present.

I want to thank Mario Medina who gave me many important ideas and shared his excellent simulation program with me to do some of the work reported here. I also thank Richard Curry who contributed in many ways to the success of this work.

I express my thanks to Carlos Ortiz of the Aerosol Technologies Laboratory, James Long and Randy Scott of the Electron Microscope Center where a portion of the experimental work was done. The training I received from them allowed me to complete the research using state of the art analytical tools.

The research reported here was sponsored by the State of Texas through the Texas Higher Education Coordinating Board, Energy Research and Applications

Program; Texas A&M University; ASHRAE; and the Escuela Politécnica Nacional of Quito-Ecuador.

TABLE OF CONTENTS

	Page
ABSTRACT.....	iii
DEDICATION.....	v
ACKNOWLEDGMENTS.....	vi
TABLE OF CONTENTS.....	viii
LIST OF FIGURES.....	xi
LIST OF TABLES.....	xv
NOMENCLATURE.....	xvi
1. INTRODUCTION.....	1
2. LITERATURE REVIEW.....	10
2.1. Introduction.....	10
2.2. Early Studies.....	12
2.3. Recent Publications.....	13
2.4. Conclusions.....	23
3. MODEL ASSUMPTIONS.....	25
3.1. Introduction.....	25
3.2. Analysis of Assumptions: Dust Particles Are Plane Areas.....	27
3.2.1. Monte Carlo Method.....	27
3.2.2. Analytical Equations.....	34
3.2.3. Analysis of Results.....	48
3.3. Assumption Analysis: Dust Particles Are at the Same Temperature as the Radiant Barrier.....	51
3.4. Model Methodology and Results.....	55
4. DUST CHARACTERIZATION.....	59
4.1. Introduction.....	59
4.2. Dust Characterization.....	59
4.3. Summary.....	66
5. MODEL TO PREDICT THE ABSORPTIVITY OF DUSTY RADIANT BARRIERS.....	68
5.1. Introduction.....	68
5.2. Analytical Approach.....	68

	Page
5.3. Graphical Method.....	69
5.4. AutoCAD Solution.....	70
5.4.1. Accuracy of Solid Volume Calculations	71
5.4.2. Model Description	74
5.4.3. Model Results.....	76
5.5. Fortran Solution.....	77
5.5.1. Program Description.....	78
5.5.2. Initialization Procedure	79
5.5.3. Drawing of the Dust Particles in the Memory Array	79
5.5.4. Finding the Area Covered by Dust	85
5.6. Summary.....	85
6. EXPERIMENTAL ANALYSIS	86
6.1. Introduction	86
6.2. Instrumentation	86
6.3. Natural Dust Collection.....	89
6.4. Experimentation Using Arizona Test Dust	90
6.5. Weight Measurements	91
6.6. Emissivity Measurements	91
6.7. Electron Microscope Analysis	93
6.7.1. Electron Microscope Basic Operating Principle.....	93
6.7.2. Experimental Procedure Using the SEM	97
6.7.3. Electron Microscope Image Processing.....	98
6.8. Determination of the Radiant Barrier Sample Area	99
6.9. Statistical Analysis of the Measurements.....	100
6.9.1. Weighing Measurements	101
6.9.2. Emissivity Measurements.....	101
6.9.3. Fraction of Area Covered by Dust Measurements.....	102
6.10. Analysis of the Experimental Results	105
7. MODEL VALIDATION	109
7.1. Introduction	109
7.2. Sensitivity Analysis.....	109
7.2.1. Sensitivity to the Dust Density	109
7.2.2. Sensitivity to the Particle Size Distribution of the Dust.....	110

	Page
7.3. Model Validation Using the Data of Fraction of Foil Area Covered by Dust.....	111
7.4. Model Validation with Dust Loading-Absorptivity Data	123
7.5. Comparison of the Present Model with the Early Model	125
7.6. Dust Influence on the Radiant Barrier Effectiveness.....	125
7.7. Time Dependence on the Radiant Barrier Absorptivity.....	127
7.8. Location Dependence on the Radiant Barrier Absorptivity.....	129
7.9. Summary.....	130
8. SUMMARY, CONCLUSIONS, AND RECOMMENDATIONS.....	131
8.1. Summary and Conclusions.....	131
8.2. Recommendations	134
REFERENCES.....	136
VITA.....	144

LIST OF FIGURES

	Page
Figure 1.1. Percent of consumption of energy by residential and commercial sectors in the U. S.....	1
Figure 1.2. Gross consumption of energy in the residential and commercial sectors in the U. S.....	2
Figure 1.3. Growth of percent of electric energy consumption corresponding to air conditioning.....	3
Figure 1.4. Wavelength distribution of blackbody radiation at 313 K.	5
Figure 2.1. Horizontal radiant barrier configuration.	11
Figure 2.2. Truss radiant barrier configuration.	11
Figure 3.1. Geometry for using the Monte Carlo method.	29
Figure 3.2. Flow chart of subroutine MCar to calculate the view factor from the roof to spheres and disks using the Monte Carlo method.	33
Figure 3.3. Comparison of shape factors from the roof to the sphere with the shape factor from the roof to the disk using the Monte Carlo method.	34
Figure 3.4. Shape factor between a finite sphere and a rectangle.	35
Figure 3.5. Comparison of tabulated and calculated values of the shape factor from a sphere to a rectangular plane using Equation (3.22).	36
Figure 3.6. Geometry to calculate the shape factor from a disk to a right triangle.	38
Figure 3.7. Comparison of tabulated and calculated values of the shape factor from a circle to a right triangle using Equation (3.25) with $X = 0.25$	39
Figure 3.8. Comparison of tabulated and calculated values of the shape factor from a circle to a right triangle using Equation (3.25) with $X = 0.50$	40

Figure 3.9. Comparison of tabulated and calculated values of the shape factor from a circle to a right triangle using Equation (3.25) with $X = 0.75$	41
Figure 3.10. Geometry to calculate the shape factor from an infinitesimal plane to a right triangle.....	43
Figure 3.11. Geometry to calculate the shape factor between two parallel planes.....	44
Figure 3.12. Flow chart of subroutine analytic to calculate the shape factor from the roof to spheres and disks using Equations (3.22), (3.25), and (3.29).....	45
Figure 3.13. Flow chart of program MCar to calculate shape factors from the roof to the particles using the Monte Carlo method and analytical formulas.....	46
Figure 3.14. Comparison of the shape factors from the roof to the spheres calculated using the Monte Carlo method and Equation (3.22).....	47
Figure 3.15. Comparison of the shape factors from the roof to the disks calculated using the Monte Carlo method and Equation (3.25).....	48
Figure 3.16. Comparison of the shape factor from the roof to a sphere with the shape factor from the roof to a disk a function of the sphere and disk diameters.....	49
Figure 3.17. Ratio of the shape factor from a sphere to the roof to the shape factor from a disk to the roof as a function of the sphere and disk diameters.....	50
Figure 3.18. Experimental set-up to analyze the temperature difference between the dust particles and the barrier's material.....	53
Figure 3.19. Typical temperature variation of the temperature recording of paint and a thermocouple under the barrier in the same spot.....	54
Figure 3.20. Typical temperature variation of the temperature recording of dust and a thermocouple under the barrier in the same spot.....	55

	Page
Figure 3.21. Early model of dust accumulation on top of HRB. No superposition present.	56
Figure 3.22. Early model of dust accumulation on top of HRB. Superposition present.	57
Figure 4.1. Particle size distribution of fine dust on a mass basis.	61
Figure 4.2. Particle size distribution of coarse dust on a mass basis.	62
Figure 4.3. Particle size distribution of fine dust on a number of particles basis.	65
Figure 4.4. Particle size distribution of coarse dust on a number of particles basis.	66
Figure 5.1. Typical dust particle superposition.	69
Figure 5.2. Representation of dust particles of different radius in a sample area of 25 mm ²	75
Figure 5.3. 3-D Representation of dust particles to be used in AutoCAD.	76
Figure 5.4. General flow chart of the program Dust.	78
Figure 5.5. Flowchart of subroutine DrawCircle.	81
Figure 5.6. Setting of pixels on the border of the circle.	83
Figure 6.1. Photograph of a radiant barrier sample.	90
Figure 6.2. Equipment used to measure the emissivity of the radiant barriers.	93
Figure 6.3. Schematic drawing of the electron and x-ray optics of a SEM.	95
Figure 6.4. Typical image obtained after digitizing the SEM pictures.	99
Figure 6.5. Experimental emissivity vs. dust accumulation for fine dust.	106
Figure 6.6. Experimental emissivity vs. dust accumulation for coarse dust.	107
Figure 6.7. Experimental emissivity vs. dust accumulation for natural dust.	108
Figure 7.1. Absorptivity vs. dust accumulation with dust density as parameter.	110
Figure 7.2. Absorptivity vs. dust loading for the coarse and fine dust.	111
Figure 7.3. Experimental vs. calculated absorptivity for radiant barrier samples with natural dust.	112

Figure 7.4. Experimental vs. calculated absorptivity for radiant barrier samples with Arizona Road Test Dust.	113
Figure 7.5. Experimental vs. calculated absorptivity for all the radiant barrier samples.	114
Figure 7.6. Electron microscope photograph and measured loading, absorptivity and fraction of foil covered by dust for sample #7.	116
Figure 7.7. Simulation of 5,300 dust particles with data of measured loading, calculated absorptivity and fraction of foil covered by dust.	116
Figure 7.8. Electron microscope photograph and measured loading, absorptivity and fraction of foil covered by dust for sample #5.	117
Figure 7.9. Simulation of 138,500 dust particles with data of measured loading, calculated absorptivity and fraction of foil covered by dust.	117
Figure 7.10. Simulation of 20,000 particles on top of a 1 mm ² sample.	119
Figure 7.11. Simulation of 40,000 particles on top of a 1 mm ² sample.	120
Figure 7.12. Simulation of 60,000 particles on top of a 1 mm ² sample.	121
Figure 7.13. Simulation of 80,000 particles on top of a 1 mm ² sample.	122
Figure 7.14. Comparison of experimental with predicted absorptivity vs. dust loading for coarse dust.	124
Figure 7.15. Comparison of experimental with predicted absorptivity vs. dust accumulation for coarse dust.	125
Figure 7.16. Radiant barrier effectiveness vs. dust loading.	126
Figure 7.17. Change in absorptivity as a function of time.	128
Figure 7.18. Location dependence on the radiant barrier absorptivity.	129

LIST OF TABLES

	Page
Table 4.1. Particle size distribution of fine dust in mass basis.....	60
Table 4.2. Particle size distribution of coarse dust in mass basis.....	60
Table 4.3. Particle size distribution of fine dust in number of particles basis.....	63
Table 4.4. Particle size distribution of coarse dust in number of particles basis.....	64
Table 5.1. Typical output of AutoCAD SOLMASSP command.....	73
Table 5.2. Evaluation of the procedure to calculate the area of a circle using AutoCAD.....	76
Table 6.1. Schedule of radiant barrier samples installation and collection.....	90
Table 6.2. Fraction of area covered by particles data for ten different probes at 500X magnification.....	103
Table 6.3. Statistics of the fraction of area covered by particles for ten different probes at 500X magnification.....	103
Table 6.4. Fraction of area covered by particles data for thirteen different locations in one probe at 500X magnification.....	104
Table 6.5. Statistics of the fraction of area covered by particles for thirteen different locations on one probe at 500X magnification.....	104
Table 7.1. Results of modeling 20,000 particles on top of a 1 mm ² sample.....	119
Table 7.2. Results of modeling 40,000 particles on top of a 1 mm ² sample.....	120
Table 7.3. Results of modeling 60,000 particles on top of a 1 mm ² sample.....	121
Table 7.4. Results of modeling 80,000 particles on top of a 1 mm ² sample.....	122
Table 7.5. Regression analysis results of experimental vs. model absorptivities for all the barrier samples.....	127

NOMENCLATURE

SYMBOL	DESCRIPTION
A	area
a	direction of the bundle in the X-coordinate, constant in quadratic equation
b	direction of the bundle in the Y-coordinate, constant in quadratic equation
C	dimension of the attic floor, coordinate of the particle
CountPix	Variable to count the number of pixels set to one
c	direction of the bundle in the Z-coordinate
f	fraction of area or number of particles
H	distance from the roof to the attic floor
L	loading, length of the bundle in Monte Carlo method
l	integer to define the subdivision level used in AutoCAD SOLMASSP command
MaxX, MaxY	maximum number of rows and columns of the array in the model
MinBit, MaxBit	minimum and maximum bits to be changed to one in the model
Nd	number of subdivisions
np	number of particles
ptr, ptrBit	variable pointer to locate the first integer to be modified, same in pixels
q	heat
R	radius, random number
RadPix	radius of the particle in pixels
s	standard deviation
SF	shape factor
T	test period, X-Y component of the bundle direction in Monte Carlo method
V	voltage
X, Y, Z	dummy variables in Equations 3.22 through 3.34
\bar{x}	mean
YLow, YHigh	starting and ending rows where pixels were to be drawn

SYMBOL	DESCRIPTION
α	absorptivity
ε	emissivity
ϕ	dummy variable of integration in Equation 3.25
φ	circumferential angle
λ	radiation wavelength
σ_0	characteristic roughness
θ	cone angle

Super / Subscripts

b	barrier
c	ceiling = attic floor, clean
d	dust, disk
ex	expected
db	dusty radiant barrier
h	high
l	low
p	particle
r	roof
s	sphere, sample
x	X direction
y	Y direction
z	Z direction
φ	circumferential angle
θ	cone angle
0	coordinate of the center of the sphere
1	coordinate in the origin of the bundle
2	coordinate of the point where the bundle crosses the attic floor
"	flux

1. INTRODUCTION

In the United States, the estimated energy consumption in the residential and commercial sectors in 1990 was 30.8 exa joules ($1 \text{ EJ} = 10^{18} \text{ J}$) which corresponded to 36 % of the total energy consumed (Figure 1.1). The annual growth rate in these sectors is about 1.5 percent a year (Energy Information Administration: EIA, 1991). Figure 1.2 shows the energy consumption in the residential and commercial sector from 1973 to 1990.

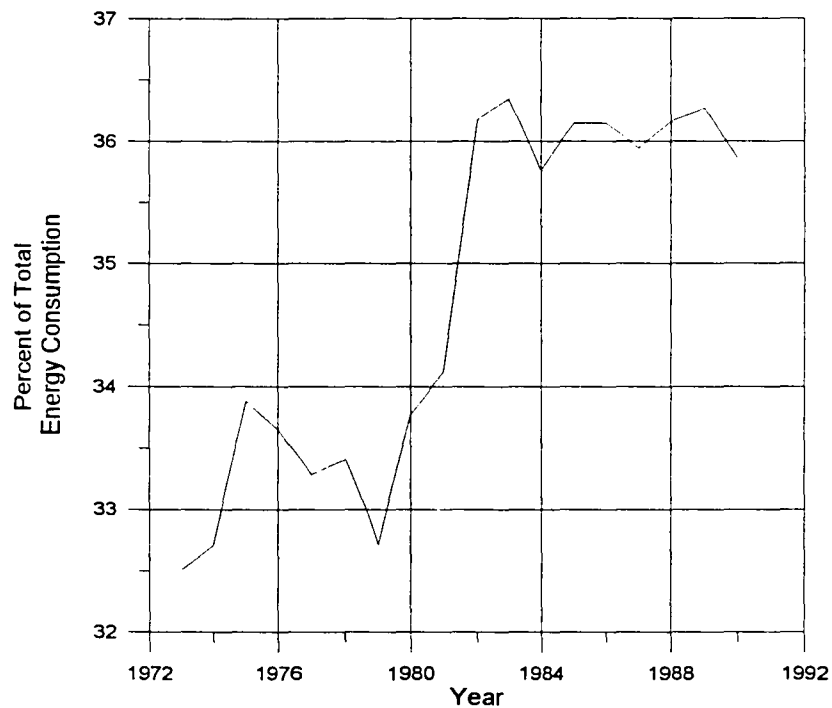


Figure 1.1. Percent of consumption of energy by residential and commercial sectors in the U. S.

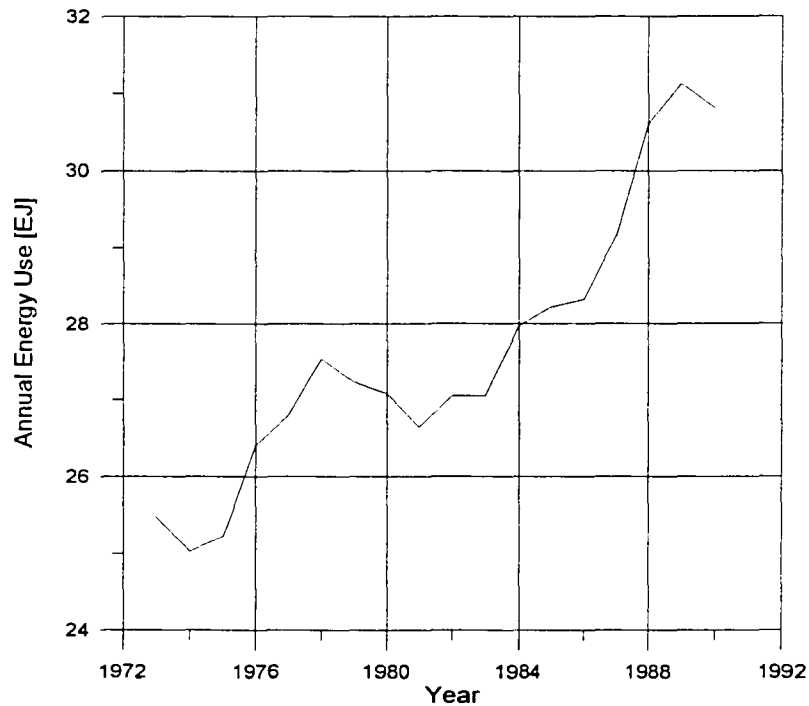


Figure 1.2. Gross consumption of energy in the residential and commercial sectors in the U. S.

The share of electric energy use corresponding to air conditioning has been steadily increasing over the past four decades. In 1968, air conditioning energy was 3 % of U. S. electric energy consumption. By 1980, cooling required 12.5 % of all electricity generated. By the year 2000, air conditioning is projected to reach 16.7 % of total electrical consumption, (Figure 1.3) (Bachman, 1985). The improvement of the standard of living in the U. S. has allowed the population of the country to afford, in larger numbers than ever, the use of air conditioning in residences. From 1973 to 1983 the number of houses with individual room air conditioners grew from 22,418,00 to 24,996,000 (11.5 % increase). The number of houses with central air conditioning systems grew from 11,858,000 to 24,234,000 (104.4 % increase) and the number of houses without any kind of air conditioner dropped from 36,884,000 to 34,214,00 (7.2 % decrease) (U. S. Bureau of Census, 1991).

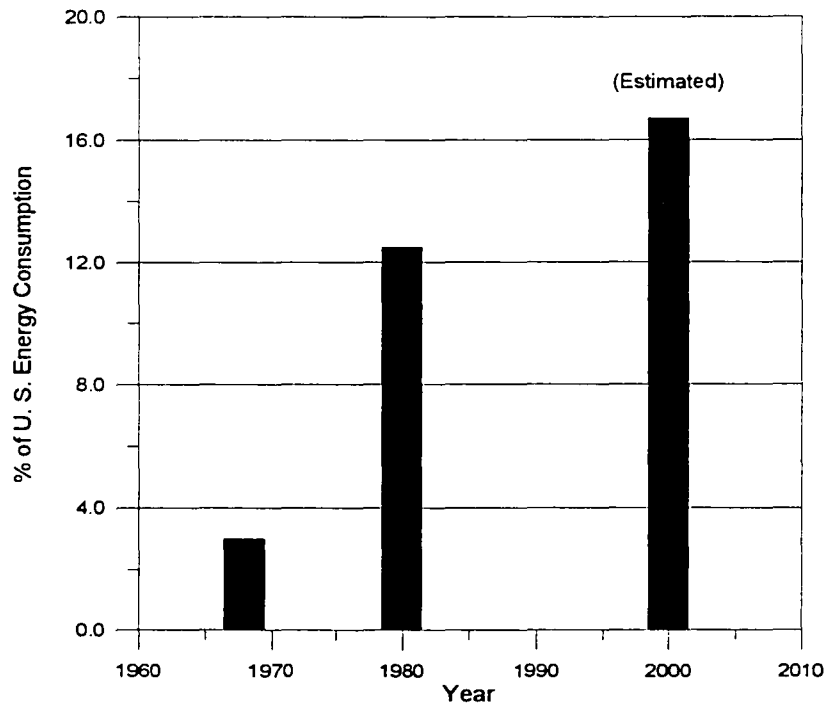


Figure 1.3. Growth of percent of electric energy consumption corresponding to air conditioning.

One way to reduce the energy consumption in the residential sector is to improve building thermal performance. This goal can be achieved with improved air leakage control in the building and with an increase of the thermal resistance of the building envelope. Improving the thermal resistance would require the use of new and better construction materials and also require optimization of the building design to achieve maximum thermal performance.

In the past two decades, a substantial amount of research has been conducted on the topic of insulation systems for buildings and major improvements have been achieved. New construction techniques and materials provide a much better thermal performance in residential buildings compared with the construction used 20 years ago.

In residences, the solar heat absorbed by the roof and subsequently transferred to the attic space is a major contributor to the cooling loads in the summer. The

improvement of the thermal performance of the attic in residential buildings plays a key role in the improvement of the overall thermal performance of the structure.

Four major heat gain prevention systems have been developed to reduce the heat flux through the attic: (1) additional insulation in the roof and ceiling to reduce conduction, (2) water spray cooling systems (Bachman, 1985, Smith and Smith, 1985), (3) ventilation of the attic, and (4) radiant barriers.

The most popular approach for reducing attic heat gain in the summer and heat losses in winter is to use fibrous insulation (e.g. fiberglass, cellulose, rock wool) in the floor of the attic (Hardy and Moon, 1989) which reduces the heat transfer by conduction. Several investigators (Hall, 1986, Katipamula and O'Neal, 1986, Katipamula et al. 1985, Fairey, 1983) have shown that thermal radiation from the roof deck to the attic floor is the primary mode of heat transfer in attics. Any device or system designed to reduce radiation heat transfer in the attic should be effective in reducing the heat gain through the roof. This is the concept behind the radiant barrier. In this work, a radiant barrier is defined as a thin, sheet-like material with at least one surface of low absorptivity (or high reflectivity) facing an air space.

The external surface of a building is usually at a different temperature than the ambient air. During a summer day, the external surface of the building is hotter because it gains solar energy at a higher rate than is dissipated through conduction to the attic interior and convection to the indoor and outdoor air. The energy radiated is primarily emitted in the long-wave range of the spectrum (4 to 40 μm), as can be seen in Figure 1.4. Radiant barriers can prevent as much as 95 percent of the infrared radiation from the attic deck from being transferred to the insulation.

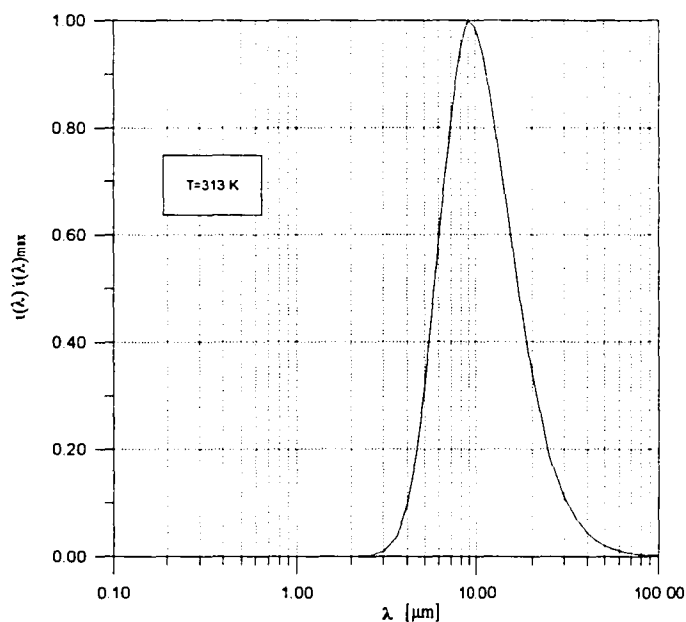


Figure 1.4. Wavelength distribution of blackbody radiation at 313 K.

Two things are needed for radiant barriers to work: (1) an empty (air) space between the exterior wall and the insulation and (2) a low absorptivity surface to block the infrared radiation. Therefore, an attic space is specially suitable for the application of radiant barriers. To fully understand how the radiant barrier works, it is necessary to understand the attic heat transfer process as a whole.

During a typical summer afternoon, the roof surface temperature may reach 75 °C (Medina, 1992). Energy is conducted across the roofing material resulting in high temperatures on the inside of the roof decking. At this point, three processes occur: first, the largest portion of the heat transfer is due to thermal radiation from the attic deck to the fibrous insulation on the top of the ceiling and some heat is radiated to other attic surfaces. Second, a small portion of heat is usually transferred by convection to the attic air. Third, heat is transferred down through the attic air by conduction.

When the outside temperature is highest, no less than 40 percent of the energy that enters the conditioned space through the ceiling is the direct result of radiant

energy from the attic deck (Medina, 1992). This heat transfer occurs primarily in the 4 to 40 μm wavelength of the infrared spectrum (Figure 1.4). The insulation material is heated in such a manner that its temperature is higher than the attic air which is then heated by upward convection from the insulation. Radiation penetrates the fibrous insulation producing a non-linear temperature distribution within the insulation, thus effectively reducing the thermal resistance of the insulation. This is why the radiant barriers are more effective, percentage wise, when used with lower R-values of insulation. Heat is then transferred by conduction from the insulation material to the ceiling which acts as a "hot plate" warming the conditioned air space and radiating heat directly to the occupants. The radiation impact on the total attic heat transfer explains why experimental studies have shown that positive ventilation of attics is not economically justified and has only a small effect in reducing heat gain through the attics (Katipamula et al., 1985).

In winter, heat is conducted from the warm ceiling of the conditioned space through the insulation material. The top of the insulation loses heat by two means: (1) convection due to warm air moving to colder upper regions of the attic, and (2) radiation from the warmer attic floor to the colder roof decking. Once the energy reaches the roof, it is transferred to the exterior by conduction through the decking and finally by convection and radiation to the atmosphere. Unlike the summer condition, the convection component of the total heat transfer is large, with radiation accounting for only a small part of the total heat transfer. Therefore, a radiant barrier will be less beneficial in winter than in summer. Levins and Karnitz (1988) reported only a 3.5 % reduction of heating loads with a radiant barrier in combination with R-30 attic insulation and a 9.3 % heating load reduction when R-11 attic insulation was used. Their study also indicated that moisture formation on the underside of radiant barrier could be a potential problem in winter in cold climates.

Inside the attic, due to the presence of the ceiling joists, the air flow is disturbed and turbulent flow is likely to occur. The use of horizontal radiant barriers reduce the roughness of the attic floor, promote laminar flow, and promote air stratification inside the attic. If laminar flow is present, the heat transfer by convection from the attic air to the ceiling is much lower than the heat transfer by convection when turbulent flow occurs. On the other hand, if air stratification occurs, lower

temperatures in the air near the ceiling would be present. In conclusion, from the convective heat transfer point of view, the presence of the radiant barrier reduces the convection heat transfer from the attic air to the ceiling by promoting laminar flow, reducing the heat transfer coefficient and by promoting air stratification with the corresponding reduction in the air temperature adjacent to the ceiling.

Aluminum foil has been used extensively as radiant barrier material due to its low cost. Aluminum oxidizes with a thin, transparent layer of oxide that prevents the oxidation process from continuing. The oxide layer maintains the absorptivity of the material close to 0.02 during extended periods of time. If the barrier is installed horizontally in a ventilated attic, dust will accumulate on the radiant barrier and the dust can increase the absorptivity of the barrier and reduce its thermal performance.

Experimental, engineering, and economic studies have been performed to quantify the performance of radiant barriers as well as to make accurate economic assessments of savings produced by them (Joy, 1958; Fairey, 1983, 1985, Katipamula et al., 1985; Katipamula and O'Neal, 1986; Levins and Karnitz, 1986a, 1986b, 1987a, 1987b, 1987c; Hall, 1988a, 1988b; Levins et al., 1990; Medina et al., 1992a, 1992b; Medina 1992).

The purpose of this work was to quantify the increase of the absorptivity of the radiant barrier due to dust accumulation and to improve the prediction capability of existing models developed to predict the energy savings produced by the use of radiant barriers. Accurate estimation of how dust affects the absorptivity of radiant barriers could allow for a better estimation of how long radiant barriers could remain in an attic and still be effective.

This research was the continuation of a previous work by the author (Noboa, 1991). Using the results from the early work, a model to predict the area of coverage of dust in horizontal radiant barriers was developed. The model performed a graphical calculation of the area covered by dust and once the area ratio was calculated, the absorptivity of the radiant barrier was found using a linear relationship between the absorptivities of the dust and the barrier and the ratio of area covered by dust.

The absorptivity of the dusty barrier could then be used to predict the reduction of the performance of the radiant barrier as a function of the amount of dust accumulated in the barrier. Finally, an empirical correlation to relate the absorptivity of the dusty radiant barrier with time was developed.

Section 2 presents a review of the literature relevant to radiant barriers, giving special attention to the experimental reports, to the modeling efforts and to the studies dealing with the influence of dust on the absorptivity of horizontal radiant barriers. The review started with a 1916 study by Dickson and Van Dusen who made the first recorded work in radiation insulation and finished with the latest developments made at Texas A&M by Medina et al. (1992).

Section 3 describes the previous work developed at Texas A&M University to model the influence of dust in the absorptivity of horizontal radiant barriers. The assumptions and limitations of that model are described and evaluated.

Section 4 deals with the dust characterization and describes the procedure followed to transform experimental data of particle size distribution given on a weight basis to a number of particles basis. This transformation was required for later use of this information in the model.

Section 5 describes the model developed in which a digital representation of the radiant barrier was made in the memory of a computer. The dust particles were simulated as an ordered set of ones in the array. The area covered by dust was found counting the number of ones in the array.

Section 6 describes the experimental procedure followed to find the relationship between the mass of dust accumulated versus the barrier absorptivity. This section also describes the experimentation to find the ratio of area covered by dust to the area of the barrier. The later experimentation was made using an electron microscope.

Section 7 deals with the comparison of the analytical and experimental results. This section describes an empirical model developed to correlate the dust

accumulation in time. Section 8 presents the conclusions and recommendations of this work.

2. LITERATURE REVIEW

2.1. Introduction

The idea of using a low absorptivity, high reflectivity material to block thermal radiation in building materials has been around since the beginning of the century (Dickson and Van Dusen referenced in Goss and Miller, 1989). Early studies deal with reflective materials used in building construction materials and structures (Nichols, 1921; Schad, 1931; Gregg, 1932, Mason, 1933). More recent literature deals with the use of reflective materials in attics to block the solar radiation coming from the roof deck to the house ceiling (Joy, 1958; Fairey, 1983, 1985, Katipamula et al., 1985; Katipamula and O'Neal, 1986; Levins and Karnitz, 1986, 1987a, 1987b, 1987c; Hall, 1988a, 1988b; Yarbrough et al., 1989; Levins et al., 1990; Medina et al., 1992a, 1992b; Medina 1992).

Radiant barriers are usually installed in three distinct configurations. The first is called a horizontal radiant barrier (HRB), in which the reflective (low absorptivity) material is placed on top of the attic joist and attic insulation as shown in Figure 2.1. If the radiant barrier has only one low absorptivity side, it must be placed with the low absorptivity side facing up, towards the attic air. It is stressed that in the HRB configuration it is the absorptivity of the material the property of interest. This clarification is made, because in the literature, the property generally used for any barrier configuration is the emissivity. In the case of the surface receiving thermal radiation, the correct name for the property is the absorptivity and in the surfaces with outgoing thermal radiation, the correct name of the property is emissivity.

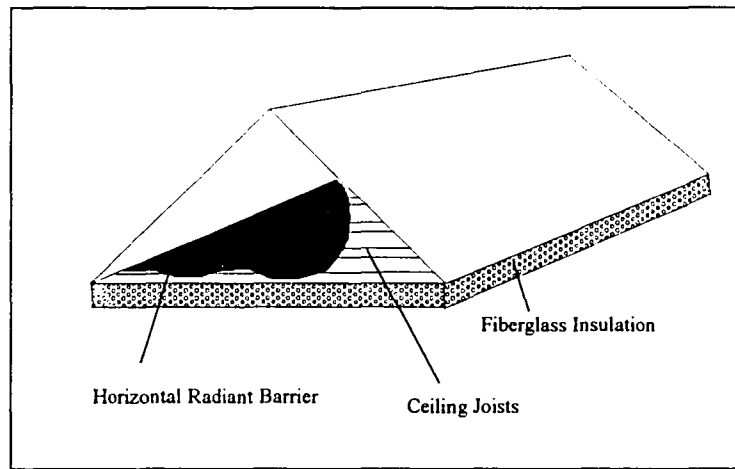


Figure 2.1. Horizontal radiant barrier configuration.

The second configuration is called the truss radiant barrier (TRB) and consists of reflective (low emissivity) material attached to the deck rafters as shown in Figure 2.2. In this configuration, an extra air space is created between the roof deck and the radiant barrier, which increases the overall thermal resistance of the attic. If one-sided radiant barrier is used, it should be installed with the low emissivity side facing downwards so no dust accumulation can occur on the low emissivity side of the material. It is also stressed for this and the next case, that the property of interest is the emissivity and not the absorptivity of the material.

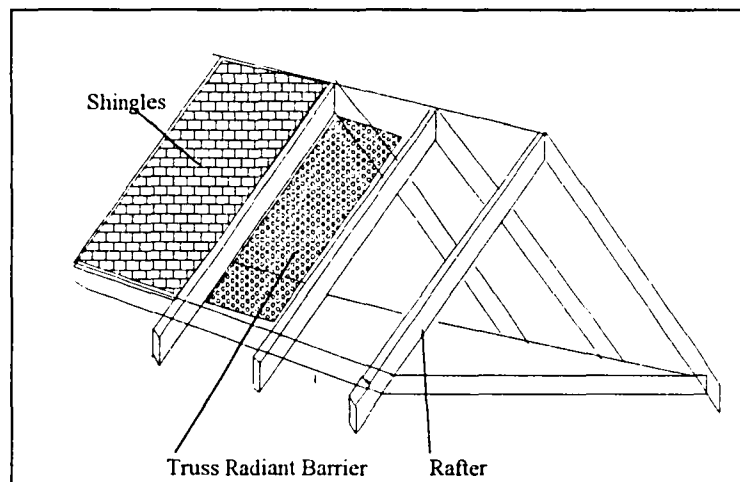


Figure 2.2. Truss radiant barrier configuration.

The third and last configuration is called draped radiant barrier (DRB) in which the radiant barrier is stapled or glued to the roof deck (plywood) so no new air space is created. This configuration is mostly used for new construction where the radiant barrier is applied to the plywood in the factory to make the procedure more economical.

In the radiant barrier analysis, it is customary to represent the radiant barrier performance as an effectiveness defined in terms of the ceiling heat flux reduction (Medina et al, 1992a, 1992b). The effectiveness is defined as the reduction of energy that is produced by the radiant barrier during the cooling period divided by the energy entering the conditioned space without the barrier. In symbolic form,

$$\text{Effectiveness} = \frac{\int_T q''_{\text{control}} dt - \int_T q''_{\text{barrier}} dt}{\int_T q''_{\text{control}} dt} \times 100 \quad (2.1)$$

Where

q''_{control} : Ceiling heat flux without the barrier (Control) [W / m²]

q''_{barrier} : Ceiling heat flux with the radiant barrier [W / m²]

T : Test Period used in the experiment [s]

Equation (2.1) also defines the ceiling heat flux reduction due to the use of the radiant barrier.

2.2. Early Studies

Dickson and Van Dusen at the U. S. Bureau of Standards in 1916 (Goss and Miller, 1989) were probably the pioneers in using reflective surfaces to block radiation heat transfer in buildings. The authors found that the use of a low emissivity material like aluminum foil (high reflectivity), produced lower heat transfer rates across the wall when compared to paper covering the wall's surfaces.

Nicholls (1921) discussed the heat transfer mechanism when reflective materials were used in enclosures. He calculated the radiation contribution to the overall heat transfer process.

During the decade of the 1930s, several papers focused on enclosures containing reflective surfaces (Schad, 1931; Gregg, 1932; Queer, 1932; Mason, 1933; Wilkes and Paterson, 1937) and reflective insulation (Wilkes, 1939; Wilkes et al., 1940). Wilkes (1939) stated that the most common material used to block thermal radiation was aluminum foil. It was used in many different configurations: sheets, corrugated cardboard, and crumpled. It is important to differentiate those early uses of aluminum foil as a radiation shield in building materials from the later use of reflective materials in attics. In the early years, reflective surfaces were used to block radiation in single or multiple enclosures in walls where no air ventilation was provided. In attics, air flow is an important part of the overall heat transfer process.

2.3. Recent Publications

Joy (1958) was a pioneer in using highly reflective aluminum foil on top of the insulation material in the attic floor. Joy reported results from experiments performed in steady-state conditions on two 3.66 x 4.96 m attics. One attic had a flat roof and the other had end gables. Joy reported heat flux reductions near 50 % in the flat roof attic and approximately 28 % in the triangular, gabled attic. Joy concluded that air ventilation further reduced the heat transfer in the flat roof attic but had a small influence in the gabled attic. Joy's studies produced the "Table of Effective Resistance of Ventilated Attics" found in the *ASHRAE Handbook of Fundamentals* (1989). This table, based on steady state experimental data, cannot be easily applied to a real attic because solar loads on the roof are transient.

The first experimental study of the influence of dust on radiant barrier performance was reported by Lotz (1964). He showed that in South Africa dust accumulated at a rate of 28.6 % area coverage per year, with an estimated full coverage in approximately five years.

Lotz was the first researcher to quantify dust loading in terms of the mass of dust per unit area of radiant barrier. Since his research, it is customary to measure

dust loading in units of milligrams of dust per square centimeter of radiant barrier [mg / cm²].

Lotz did not measure the absorptivity of the radiant barriers. However, degradation was quantified as energy savings related to dust accumulation. For a dust loading of 0.54 mg / cm², the radiant barrier performance degradation was 30 %. For a dust loading equal to 1.61 mg / cm², the degradation was 60 %. Dust loading was strongly influenced by local and seasonal conditions.

McQuiston et al. (1984) reported the results of an experimental study at the Engineering Laboratory at the Oklahoma State University Campus where the laboratory was divided into two 58 m² sections. One section was insulated with 15.2 cm of aluminum foil backed mineral wool with the reflective surface acting as a HRB. The other section had the same insulation without the aluminum foil backing. Summer experiments showed a reduction of approximately 20 % in ceiling heat flux. The winter experiments showed a heat flux reduction between 5 to 10 %. It is important to note that the inner side of the ceiling facing the conditioned space had been painted with aluminum paint so its emissivity was 0.3. This fact might explain the low heat flux percent reduction. The author does not mention any analysis of the cross-effect occurring in one side of the building due to the use of the barrier in the other side. Due to the use of the barrier, it is likely that the temperature of the attic space would experience an increase so the energy gain in the side without the barrier had been influenced by the presence of barrier in the other side of the building.

Fairey (1983, 1985) divided the Laboratory Building at the Florida Solar Energy Center (FSEC) in Cape Canaveral, into three sections. Each section was approximately 4.9 m² using forced ventilation and an average insulation with a resistance value of 3.35 m²K / W (R-19). The average ceiling heat flux reduction due to the use of radiant barrier was 43 %. Fairey concluded that with the TRB configuration, the effectiveness is equal for both one and two sided barrier.

Katipamula et al. (1985) conducted a steady state experimental study of roof insulation using an attic simulator. They found that ventilation of the heated space reduced the temperature of the outer layer of the attic insulation by about 7 °C. The

reduction in the heat flux was about 15 % for a 53 °C roof temperature and 8.9 cm of insulation. The experimental research also found that the use of a radiant barrier reduced the total heat flux through the insulation by as much as 50 %. Their study also showed that radiation had an important effect on the thermal insulation properties of fibrous materials due to the penetration of infrared radiation into the low density fibrous insulation. Because of the radiant energy penetration into the insulation, it was recommended that radiation to fibrous materials should not be treated as a surface phenomena. Radiation in a scattering and absorbing medium seemed to be the best approach to analyze this phenomena. Their study showed that the radiation penetrating the insulation generates a non-linear temperature gradient within the fibrous materials, and this produced an effective thermal conductivity higher than the manufacturer's specification.

Katipamula and O'Neal (1986) and Katipamula et al. (1987) reported the results of research on the performance of radiant barriers using an attic simulator. In the report of steady state experiments, the authors stressed the importance of the location of the barrier in the attic. Three radiant barrier locations were studied: under the roof deck, underneath the rafters and on top of the ceiling insulation. The location directly over the ceiling insulation provided the greatest heat flux reduction. Katipamula and O'Neal also showed that the radiant barrier was more effective as the roof temperature increased. For example, with deck temperature of 49 °C, a HRB placed 15.2 cm below the roof deck, produced 53 % reduction of heat flux. When the temperature was increased to 60 °C the reduction was 66 %.

Levins and Karnitz (1986, 1987a, 1987b, 1987c) and Levins, Karnitz and Knight (1986) made a series of energy measurements of houses with attics containing radiant barriers. Three houses were tested to compare their performance when radiant barriers were used. Although they found that radiant barriers reduced attic heat transfer, their methods had several serious problems. First, the measured cooling loads showed significant variation between the test houses even though the houses were supposedly identical. Without radiant barriers, the houses differed by as much as 50 % in energy use. It was hypothesized that the differences were due to dissimilarity in the envelope construction, in the values of the coefficient of performance of the air conditioners and in the air leakage rates. These differences cannot be overlooked and

influence the interpretation of the final results. The results had to be normalized with respect to the control house to compensate for the measured differences without the barrier. Only two 6.4 by 6.4 cm. heat flux meters were used for each house. It was not clear from the study how representative the heat flux measurements were of the total heat transfer in the houses.

The results of the experiments using $3.35 \text{ m}^2\text{K/W}$ resistance fiberglass insulation showed that the HRB produced a 35 % ceiling flux reduction in summer and an electric energy savings (cooling load reduction) of 21 %. The size of the electric savings was much larger than could be expected considering the size of the ceiling heat flux reduction. The authors explained this incongruent result by the calibration problems stated above. The HRB produced 10 % ceiling heat flux savings in winter. The TRB produced ceiling heat flux savings of 13 % in the cooling season and produced an increase on the energy heating consumption of 3 %.

The authors also evaluated the performance of radiant barriers with different values of thermal resistance of the insulation. For insulation with a resistance of $1.94 \text{ m}^2\text{K/W}$, the cooling heat flux reduction was 16 % for the HRB and 11 % for the TRB. For insulation with resistance of $5.28 \text{ m}^2\text{K/W}$, the cooling heat flux reduction was about 2 %.

Hall (1986) reported a study on radiant barrier performance using small test cells in Chattanooga, Tennessee. Ceiling heat flux gain during the cooling season was reduced by 30 to 40 %. Hall stated that radiant barriers proved useful in the winter when significant heat flow reductions could be achieved. The roof deck temperatures in the summer days were, in the worst case, only $4.4 \text{ }^\circ\text{C}$ warmer when radiant barrier was used. These results helped clarify early questions about the potential danger of the use of radiant barrier to the roofing materials, specifically the roof shingles. Such small temperature increase represents no problem to the shingles. Attic ventilation was not studied, and there was no quantitative or qualitative information about the impact of dust on the radiant barrier performance.

Lear et al. (1987) performed side-by-side experiments at the University of Florida in Gainesville. The houses had identical floor plans but differed in the attic

ventilation method. The control house had an attic with soffit/gable louver combination while the test house had full ridge/continuous soffit ventilation arrangement plus a set of soffit and gable louvers. Both attics were naturally vented; however, the control attic had a soffit/gable louver combination; whereas, the test attic had full ridge/continuous soffit ventilation plus a set of soffit and gable louvers. Because of the ventilation differences, it was not unexpected to find that the test house had an integrated ceiling heat flux about 30 % lower than the control house. For comparison purposes, the results had to be normalized with respect to the control house. The radiant barrier was a TRB made of aluminum foil with one side covered with craft paper. In experiments performed in 12 hour periods (from 10:00 to 22:00 H), no difference was noticed when the low emissivity side of the barrier was placed facing the attic air or facing the roof. In both cases, a reduction of 40 % of integrated ceiling heat flux was measured. The time period chosen to perform the experiments explains the rather high energy savings obtained in the test.

Yarbrough in 1987 (Levins and Hall, 1990), was the first to relate the absorptivity of radiant barriers with dust accumulation. Using Arizona Road Test Dust for the experimentation, he developed an exponential curve fit for the absorptivity as a function of dust loading. Although Fairey et al. (1988) said that Yarbrough's (1987) data did not show any noticeable sensitivity to dust particle size. Later works (Levins et al., 1990) showed that absorptivity was strongly influenced by dust composition.

Fairey et al. (1988) developed two models for predicting the energy savings associated with the use of radiant barriers in attics. The first model was a steady-state energy balance for attics with flat roofs. The model considered attic ventilation assuming that the air flow between the floor and the deck was driven by buoyancy and the flow was parallel to the ceiling joist and roof rafters. The parametric study showed that the radiant barrier absorptivity and the inlet air temperature had the greatest influence. The model predicted that an increase in the absorptivity of the radiant barrier from 0.1 to 0.3 reduced the percent savings in heat flux from 40 to 17 %. The model agreed with published data (Joy, 1958) for insulation levels corresponding to a resistance of $1.29 \text{ m}^2\text{K/W}$. However, the model deviated from Joy's data for insulation levels greater than $3.35 \text{ m}^2\text{K/W}$.

Hall (1988a) tested the performance of radiant barriers with different insulation materials. He reported similar results with glass fiber, cellulose, or rock wool, as long as the insulation had the same R-value. He concluded that radiant barrier behavior was independent of the type of insulation material used in the attic. The savings reported were greater with lower R-values. In side-by-side testing, dust accumulation appeared to have very little effect on the radiant barrier performance. The reported heat flux with dust on the radiant barrier was "remarkably similar" to the heat flux of a radiant barrier without dust. The author stated the necessity of more research in this issue. Using a single sided radiant barrier and a black plastic layer over the insulation, Hall tried to separate the convective and the radiative effect on the performance of the radiant barrier. He showed that the energy saving related with the radiant barrier use was due to the reflective quality of the material.

In another report, Hall (1988b) continued the study of the key issues in radiant barriers, reporting results on dust accumulation, attic ventilation and ceiling insulation on their performance. This report showed that degenerated radiant barriers with absorptivities as high as 0.5 still reduced heat flow nearly 20 %. Variation in venting type did not change radiant barrier performance. Side-by-side testing showed that insulation with a resistance value of $1.95 \text{ m}^2\text{K/W}$ (R-11) with a radiant barrier performed nearly as well as $5.28 \text{ m}^2\text{K/W}$ (R-30) without a radiant barrier. $3.35 \text{ m}^2\text{K/W}$ (R-19) insulation with a radiant barrier performed better than $5.28 \text{ m}^2\text{K/W}$ (R-30) insulation without a radiant barrier. With or without radiant barriers, large increases in attic ventilation produced only a small reduction in ceiling heat flux.

Ober and Volckhausen (1988) tested the performance of radiant barriers in a duplex with attics containing soffit/ridge vents. Tracer gas was used to measure the attic ventilation. Two different air flow patterns were tested using and removing baffles to provide ventilation between the wall and the underside of the roof. Twenty percent heat flux reduction was measured with both types of ventilation using TRB.

Wilkes (1988) developed a model for simulating attics with and without radiant barriers that was based on a system of energy balances. The heat transfer

equations for conduction, convection and radiation were formulated and a system of equations was developed. The Gauss-Jordan elimination method was used to solve the system with no convergence problems reported. The program compared well with limited experimental data. Upon validation, the model could be used to extrapolate the experimental results to long term analysis.

Cook et al. (1989) reported on the contamination of the radiant barrier material by dust and its influence on the barrier's thermal performance. The paper included three main topics. The first section reports the relationships between the amount of dust present on the foil (dust loading) and the emittance of the dusty surface. The second section relates the time that foil samples had been exposed to dust with the absorptivity of the surface and the third section reports the result of modeling calculations to determine the effect of increasing emittance on the ceiling heat flux.

In the first set of experiments, three dust types were used: (1) Arizona test dust, (2) dust collected from the interior of residential houses, and (3) dust collected inside residential attics. The experiments using Arizona test dust differed from Noboa (1991) and from Levins and Hall (1990) because the dust absorptivity was reported as 0.674. Noboa and Levins and Hall reported 0.82. Cook et al. presented the results in the form of an exponential equation previously developed by Hall (1988b).

In the second section, the authors reported the experimental procedure carried out to relate the absorptivity of dusty aluminum foil with the time that the foil had been exposed to dust inside the attic of houses in the Chicago area in an urban region with paved roads and well developed landscaping. No correlations or any further analysis were presented. The authors observed a linear relationship between the area of dust coverage to the absorptivity of the dusty radiant barrier of the form,

$$\alpha_{db} = f_p \alpha_d + \alpha_b \cdot (1 - f_p) \quad (2.2)$$

where

- α_{db} : Absorptivity of the dusty radiant barrier
- α_d : Absorptivity of the dust particles
- α_b : Absorptivity of the barrier (0.03)
- f_p : Fraction of the foil area covered by particles

This equation was used to predict the absorptivity of dust samples subject to dust accumulation. The experimental process included the use of the electron microscope, and the area of dust coverage was calculated from particle diameter data on the assumption that the particles were spherical. Large differences between the calculated and experimental absorptivities were reported for some of the experiments. In the paper, the differences were explained as the result of differences in the particle size distribution of the dust, particularly on the Hobart and Valparaiso specimens, which had a much larger fraction of particles above 10 μm . The assumed absorptivity of the particles and the error introduced in the calculation of the area of coverage could better explain those differences. Equation (2.1) was later corroborated by Noboa (1991) in an analytical analysis.

Cook et al. hypothesized that the variables influencing the resulting absorptivity were the dust loading [mg/cm^2], the mean diameter of the dust particles, the absorptivity of the clean barrier and the absorptivity of the dust. They then used the Wilkes (1988) model to calculate the effect of the emittance on the heat flux savings for HRB.

The researchers also made reference to experimental work using electron microscopy analysis reported in a 1989 Master's thesis by J. C. Cook Jr. of the Department of Chemical Engineering of the Tennessee Technological University. Upon investigation, it was found that the thesis was never completed.

Wilkes (1989) reported the Oak Ridge National Laboratory effort in developing an automated code to model attics containing radiant barriers. His model took into account all the heat transfer mechanisms present in attics and showed good

agreement with experimental data. The program was based on the model developed by Peavy (1979) and later extended by Wilkes (1983). The model allowed the radiant surfaces to have variable absorptivity, but dust accumulation was not included explicitly. The data agreed well with the simulation.

Levins and Hall (1990) presented the results of an experimental study to measure the effects of dust on the performance of radiant barriers when installed on top of attic insulation. The tests did not include dust size influence on radiant barrier performance or absorptivity. The authors stated that the reduction in attic heat transfer resulting from the use of radiant barrier was much less sensitive to dust accumulation than the absorptivity of the barrier. These observations may reflect the fact that the barrier may also have blocked infiltration paths through the ceiling. Even with a large amount of dust, radiant barriers still significantly reduced ceiling heat fluxes. The experiments provided the following results: Clean radiant barrier produced a reduction of the total heat input to the house one of 14.3 %, while for house two the total heat input reduction was 9.3 %. Radiant barrier with a dust loading of 0.74 mg / cm² ($\epsilon = 0.185$) produced a total house heat input reduction of 7.1 %, while for house two with a dust load of 0.34 mg / cm² ($\epsilon = 0.125$) produced a total house heat input reduction of 7.1 %.

Levins et al. (1990) reported an experimental study on the effect of ventilation and dust accumulation on the performance of radiant barriers. They found that artificially applied dust did not adhere to the radiant barrier as well as natural dust. Natural pollutants, such as pollen and hydrocarbons, adhere better to the barrier than Arizona road dust used in the experiments. Although data acquisition problems were reported in the experiments carried out over a seven day test period, results showed that 0.34 mg / cm² of dust increased heat flow by 12.6 %, while 0.74 mg / cm² of dust increased heat flow in the attic by a 28.4 %. The authors suggested that a dusty radiant barrier still was more effective than no radiant barrier. This research did not provide data correlating dust loading and percent of barrier's area covered by dust.

Noboa (1991) developed an analytical model to predict the absorptivity of the dusty radiant barrier. The geometrical model was a triangular enclosure in which the temperatures of the enclosing surfaces were known. The dust particles were assumed

to have an absorptivity of 0.82 and the radiant barrier was assumed to have an absorptivity of 0.02. The dust particles were simulated as circles of uniform diameter equal to the mean diameter of the Arizona road test dust used in the experiments. In the model, the dust particles were placed on the nodes of a uniform array located over the entire attic floor, and for modeling various dust loadings, the array was made coarser or finer according to the required number of particles to be simulated. In this model, dust superposition occurred when the distance between the particles was less than the mean diameter of the particles.

The thermal model was developed using the "Net Radiation Method". The solution of a system of equations describing the radiation heat transfer provided the heat flux for each element of the enclosure. Finally, replacing the radiant barrier and the dust particles for an equivalent surface corresponding to the dusty radiant barrier provided the means to calculate the absorptivity of this dusty radiant barrier.

Experimentation was carried out using a reflection emissometer to measure the increase of the absorptivity of aluminum radiant barrier when known quantities of dust were artificially applied to it. The experimental results showed good agreement with the theoretical model.

A linear relationship between the absorptivity and the area of dust coverage was found. This simple relationship can be used to determine the overall absorptivity of a radiant barrier if the area of dust coverage can be determined.

Winiarski (1992) developed a quasi-steady state model to predict attic heat transfer and energy savings in residences using radiant barriers as a part of an M. S. project. The model agreed well with experimental data when the results were corrected for the transient effect of heat absorbed and released by the material of the attic enclosure.

Medina et al. (1992a) tested the performance of radiant barriers in unoccupied test houses with identical floor plans of 3.66 x 3.66 m during the cooling season. The baseline calibration showed that the two houses responded similarly to weather changes. Medina performed HRB and TRB experiments with different attic

ventilation rates. Results showed that the radiant barrier effectiveness was sensitive to air flow changes up to $1.3 \text{ l}/(\text{s} \cdot \text{m}^2)$. At higher velocities, the ceiling heat flux reduction remained constant regardless of the increase in the air flow rate. The reported ceiling flux reductions were approximately 34 % for non-vented attics and 28 % for vented attics. Medina et al. (1992b) also performed winter experiments in which the experiments showed that the HRB produced larger reductions than the TRB (17 and 14 %, respectively).

Medina (1992) reported a complete experimental and analytical study of radiant barriers in which a heat and mass transfer transient model was developed to predict ceiling heat flux through the attic space in residences and to estimate savings in cooling and heating loads produced by the use of radiant barriers. The model accounted for transient conduction, convection and radiation, and incorporated moisture and air transport across the attic. Environmental variables such as solar loads and sky temperatures were also estimated. The model calculated ceiling heat fluxes and various surfaces temperatures with hourly weather data as input. Medina showed that the barrier effectiveness is a continuous, almost linear, function of the absorptivity.

Even though an extensive literature search was conducted to find references on particle interaction in radiation heat transfer, the only references available are those related with particles suspended in gases, that make the gas (usually a flame) a participating media that are not relevant to the present research.

2.4. Conclusions

Based on the literature, the following conclusions were drawn:

1. Radiant barriers do contribute to a reduction of the cooling and heating loads when compared to houses without radiant barriers. The ceiling heat flux reduction varies from approximately 40-45 % when insulation with a resistance value of $1.95 \text{ m}^2\text{K}/\text{W}$ to approximately 15-20 % when the insulation resistance is $5.28 \text{ m}^2\text{K}/\text{W}$.

2. The ceiling heat flux reductions depend upon the barrier absorptivity, attic geometry, attic ventilation and insulation level.
3. A clean HRB is 5 to 10 % more effective than the TRB, and the former uses less material for any installation. The HRB absorptivity degrades due to dust accumulation.
4. HRB effectiveness was independent of the absorptivity of the under side absorptivity of the barrier.
5. TRB effectiveness was independent of the following parameters: (1) The barrier construction with one or two sides of low emissivity. (2) The installation procedure, using the low emissivity side faced up or down.
6. Radiant barrier effectiveness was independent of the kind of insulation material used in the attic as long as the thermal resistance values of the insulation were the same.
7. Cooling season energy reductions were higher than heating season energy reductions, i. e., approximately 35 % reduction for summer and approximately 15 % for winter when radiant barrier was used with insulation with a resistance value of $3.35 \text{ m}^2\text{K} / \text{W}$.
8. Several steady-state and transient models have been developed using finite element, finite differences, response factors, and transfer functions methods. The transfer function models are easier to make, faster to run and provide accurate results (Medina, 1992).
9. The only analytical work developed to predict the dusty barrier's absorptivity is the work by Noboa (1991). That work and Cook (1989) suggest that the absorptivity of the dusty radiant barrier is a function of the fraction of area covered by dust, the absorptivity of the clean radiant barrier and the mean absorptivity of the dust.

3. MODEL ASSUMPTIONS

3.1. Introduction

One of the main objectives of this research was to develop a numerical model to predict the absorptivity degradation of the HRB due to dust accumulation. This work was built upon research conducted earlier by Noboa (1991) at Texas A&M University as a part of an M. S. project. A formal analysis of the assumptions and restrictions used in the numerical work that apply to the present research is covered in this section.

1. The surfaces were assumed flat, diffuse, gray, opaque, and planes. Radiation properties for nonmetals are much less available and detailed than for metals (Siegel and Howell, 1981). However, nonmetals are generally characterized by large values of total hemispherical emissivity and absorptivity at moderate temperatures. Directional emissivity will decrease for angles greater than 45° . From available data for typewriter paper (made from wood) the reflectivity, measured at 75° of angle of reflection, grows from 0.1 at 0° to 0.25 at 45° of angle of incidence (Siegel and Howell, 1981). For angles of reflection less than 75° , the variation is insignificant. From this very limited data, one could conclude that nonmetals in general and wood in particular could be treated as diffuse surfaces.

The optical roughness σ_0 / λ is defined as the ratio of a characteristic roughness height (usually the root mean-square, rms. roughness σ_0) to the wavelength of the radiation. The characteristic roughness was estimated for plywood to be $200 \mu\text{m}$ and the radiation wavelength $10 \mu\text{m}$, so the optical roughness σ_0 / λ was estimated to be 20. When $\sigma_0 / \lambda > 1$, there are multiple reflections in the cavities (Siegel and Howell, 1981). As a result, the hemispherical absorptivity and emissivity increases with respect to the properties of the polished material. Because the emissivity of the material was measured with an hemispherical emissometer, the optical roughness of the material was properly considered in the model.

The rafters of a typical attic usually account for less than 5 % of the attic area and are made from wood similar to the roof deck. Their influence in the geometrical model should be minimal.

Finally, it is known (Siegel and Howell, 1981) that for nonmetals, wavelength dependence of radiative properties is generally weak, and it was reasonable to assume that the attic surfaces were gray.

2. It was assumed that the roof deck was radiating thermal energy uniformly and diffusely with an emissivity given as ϵ_r . While there may be differences in emissivities within the attic deck materials, these were assumed to be small enough that the deck was homogeneous.
3. The radiant barrier was assumed to be made of aluminum foil with an absorptivity α_b . The decking surfaces inside the attic are emitting energy diffusely, so, even though polished metal surfaces produce specular reflection, the reflected radiation is going to be as diffuse as the incoming radiation. Additionally, the barrier usually had so many wrinkles that the absorptivity and reflectivity were considered diffuse. Aluminum foil is the material of choice as radiant barrier due to its low absorptivity and low cost.
4. All the dust particles had an absorptivity α_d .
5. The air in the attic was a non-participating medium.
6. Energy interchange occurred only by radiation between the attic surfaces and the dust particles. A model to simulate the heat transfer in the attic must take into account all heat transfer mechanisms. For the purpose of defining the influence of dust on the absorptivity of the radiant barrier, only radiation needed to be considered.
7. The dust particles were plane areas.

8. No heat transfer occurred between two different dust particles. Because the particles were assumed to be planes, they cannot "see" each other from a radiation stand point.
9. Dust particles and the radiant barrier were at the same temperature.

From these assumptions, the last three deserved special attention, and further analysis follows.

3.2. Analysis of Assumptions: Dust Particles Are Plane Areas

The dust particles considered in this research range in size from less than one to 200 micrometers in diameter. By comparison, the dimensions of the attic roof or floor are several meters in length and width. Because of the small dimensions of the particles, it was assumed that they were viewed by the roof as flat surfaces.

To validate this assumption, a computer program was developed to compare the shape factors from a plane (roof) to spheres of varying diameters and from the same plane to disks with the same diameters of the spheres, located in an enclosure similar to a typical attic. Two approaches were taken: the Monte Carlo method was used, and the numerical results obtained using this method were compared with analytical formulas obtained in the literature. The final goal was to be able to compare those shape factors as a function of the diameter of the particles.

3.2.1. Monte Carlo Method

The Monte Carlo method was defined by Kahn (1956) with the following salient ideas:

"The expected score of a player in any reasonable game of chance, however complicated, can in principle be estimated by averaging the results of a large number of plays of the game. Such estimation can be rendered more efficient by various devices which replace the game with another known to have the same expected score. The new game may lead to a more efficient estimate by being less erratic, that is, having a score of lower variance, or by being cheaper to play with the equipment on hand. There are obviously many problems about probability that can be viewed as problems of calculating the expected score of a game. Still more, there are problems that do not concern probability but are none the less equivalent

for some purposes to the calculation of an expected score. The Monte Carlo method refers simply to the exploitation of these remarks."

This definition provides a good outline for the use of the method. What has to be done for solving a specific problem is to set up a game or model that has the same behavior, and hence is expected to produce the same outcome, as the physical problem that the model simulates. Make the game as simple and fast as possible. Use any available methods to reduce the variance of the average outcome of the game. Play the game many times and find the average outcome.

Siegel and Howell (1981) described the procedure to use the Monte Carlo method in thermal radiation problems. Following their outline, and assuming the surfaces were gray, opaque and diffuse, a computer program was written to calculate the shape factors from the roof to circles and spheres having the same diameter.

The program simulated shooting bundles of radiating energy from the attic roof. To reduce the random numbers generated, the roof was swept in the X and Y directions in equal steps dx and dy (Siegel and Howell, 1981). From each point of the roof, a bundle of energy was "shot" in a random direction. Once the direction was set, the bundle was tracked down to find out if it hit the sphere (or the disk). If the bundle missed the particle, the trajectory was further studied to find out if it hit the attic floor or, if the bundle missed both the particle and the floor. The shape factor from the roof to the sphere, SFr-s was calculated as the ratio of the number of hits to the sphere to the total number of bundles. Similarly, the shape factors from the roof to the disk, SFr-d and the shape factor from the roof to the attic floor (ceiling), SFr-c were calculated as the ratio of the numbers of hits on the target to the total number of bundles.

The direction of the bundle of energy from the surface was defined by the angles θ and φ , (Figure 3.1). These angles were calculated using the following expressions (Siegel and Howell, 1981):

$$\theta = \sin^{-1} (R_{\theta}) \quad (3.1)$$

$$\varphi = 2 \cdot \pi \cdot R_{\varphi} \quad (3.2)$$

R_θ is a random number between zero and one used for calculating θ , and R_ϕ is a different random number between zero and one used for calculating ϕ .

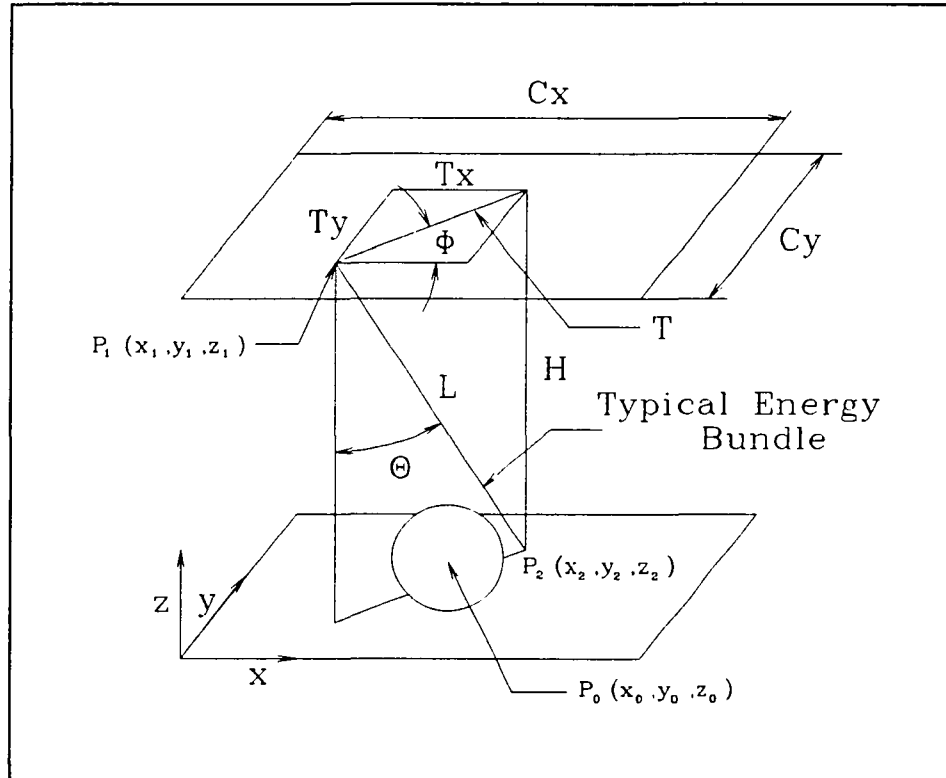


Figure 3.1. Geometry for using the Monte Carlo method.

Noting that the coordinates of the center of the sphere were $P_0 = (x_0, y_0, z_0)$, the coordinates of the origin of the bundle were $P_1 = (x_1, y_1, z_1)$ and the coordinates of the point where the bundle crosses the ceiling plane were $P_2 = (x_2, y_2, z_2)$.

The lengths L , T , T_x , and T_y ; and the direction of the bundle (a , b , c) were calculated using the following relationships:

$$L = \frac{H}{\cos(\theta)} \quad (3.3)$$

$$T = \frac{L}{\sin \Theta} \quad (3.4)$$

$$T_x = T \cos(\varphi) \quad (3.5)$$

$$T_y = T \sin(\varphi) \quad (3.6)$$

$$a = \frac{T_x}{L} \quad (3.7)$$

$$b = \frac{T_y}{L} \quad (3.8)$$

$$c = -\frac{H}{L} \quad (3.9)$$

The distance from the ray to the center of the sphere was calculated as (Standard Mathematical Tables, 1967):

$$\text{Distance} = \sqrt{\frac{\left| \begin{array}{cc} y_0 - y_1 & z_0 - z_1 \\ b & c \end{array} \right|^2 + \left| \begin{array}{cc} z_0 - z_1 & x_0 - x_1 \\ c & a \end{array} \right|^2 + \left| \begin{array}{cc} x_0 - x_1 & y_0 - y_1 \\ a & b \end{array} \right|^2}{a^2 + b^2 + c^2}} \quad (3.10)$$

If the distance was less than the radius of the sphere, then the bundle hit the sphere; otherwise, the bundle missed it. Next, the program calculated the coordinates where the bundle crossed the ceiling plane. If the coordinates were within the boundaries of the ceiling, the bundle struck the ceiling, otherwise it missed. In counting the bundles that strike the ceiling, care was taken not to count the bundles that have already struck the sphere. Appropriate counters kept the number of hits in each surface.

The procedure was repeated for the case of the disk lying on the ceiling floor, but for this case, it was necessary to find the coordinates of the point P_2 where the bundle crosses the ceiling (floor of the attic). These coordinates were:

$$x_2 = x_1 + T_x \quad (3.11)$$

$$y_2 = y_1 + T_y \quad (3.12)$$

$$z_2 = 0 \quad (3.13)$$

The distance from the point the ray crossed the ceiling plane to the center of the disk was:

$$\text{Distance} = \sqrt{(x_2 - x_1)^2 + (y_2 - y_1)^2} \quad (3.14)$$

If this distance was less than the radius of the disk, the ray struck the disk; otherwise, it missed. A different set of counters kept the number of hits for this case and the shape factor was calculated using the ratio between the hits to the total number of bundles (Figure 3.2).

When all the bundles have been emitted, the shape factors from the roof to the sphere, to the disk and to the ceiling were calculated as:

$$\text{SFr} - s = \frac{\text{Hits to the Sphere}}{\text{Total Bundles}} \quad (3.15)$$

$$\text{SFr} - d = \frac{\text{Hits to the Disk}}{\text{Total Bundles}} \quad (3.16)$$

$$\text{SFr} - c = \frac{\text{Hits to the Ceiling}}{\text{Total Bundles}} \quad (3.17)$$

The view factor from the roof to the clean ceiling (whole attic floor) was calculated as:

$$\text{SFr} - cc = \frac{(\text{Hits to the Ceiling} + \text{Hits to the Sphere})}{\text{Total Bundles}} \quad (3.18)$$

The other shape factors were calculated using the reciprocity relationship:

$$\text{SFs} - r = \frac{\text{SFr} - s \cdot A_r}{A_s} \quad (3.19)$$

$$SF_{d-r} = \frac{S_{fr} - d \cdot A_r}{A_d} \quad (3.20)$$

$$SF_{cc-r} = \frac{S_{fr} - cc \cdot A_r}{A_{cc}} \quad (3.21)$$

The flow chart corresponding to the subroutine MCar, which calculated the shape factors from the roof to a sphere and from the roof to a circular disk using the Monte Carlo method is shown in the Figure 3.2.

The roof was modeled with dimensions 4.0 m by 6.0 m and the distance from the roof to the attic floor was 1 m. The program calculated the shape factors for the particle radius decreasing from 0.5 m until the number of hits reduced to zero. The program emitted 3,600,000,000 bundles and took 20 hours of CPU in the super computer to calculate the shape factors for 11 different sizes of spheres and circles. For the chosen geometry and number of bundles, for a radius less than 6.1×10^{-5} m, the number of hits to the particles (spheres or circles) reduced to zero. The shape factor from the roof to the particle could not be evaluated for any smaller spheres. Figure 3.3 shows the results obtained with the Monte Carlo method.

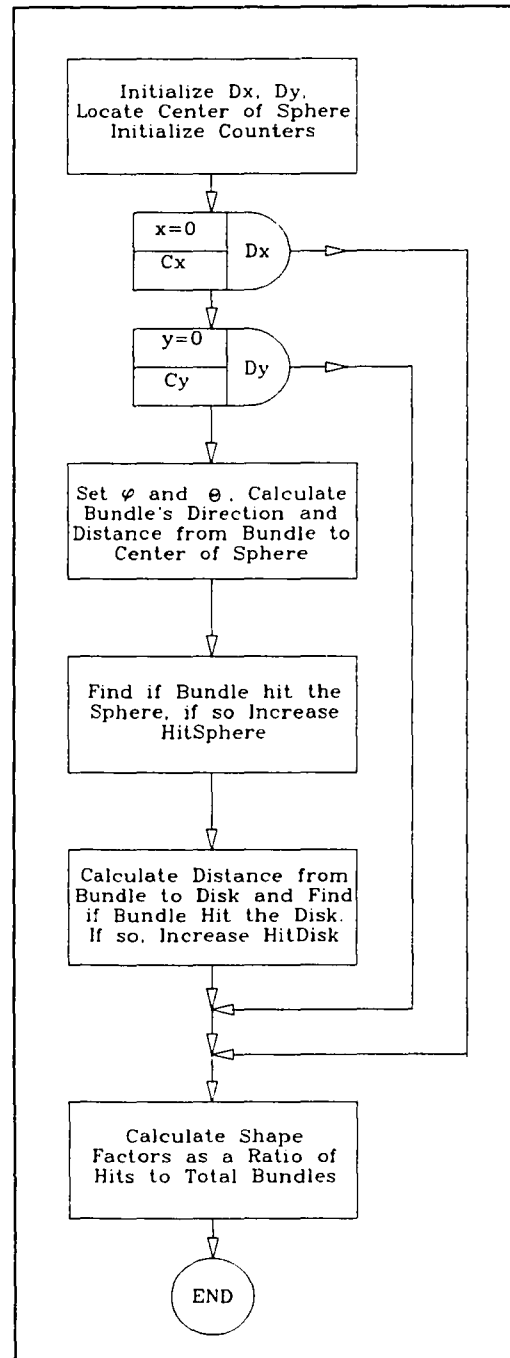


Figure 3.2. Flow chart of subroutine MCar to calculate the view factor from the roof to spheres and disks using the Monte Carlo method.

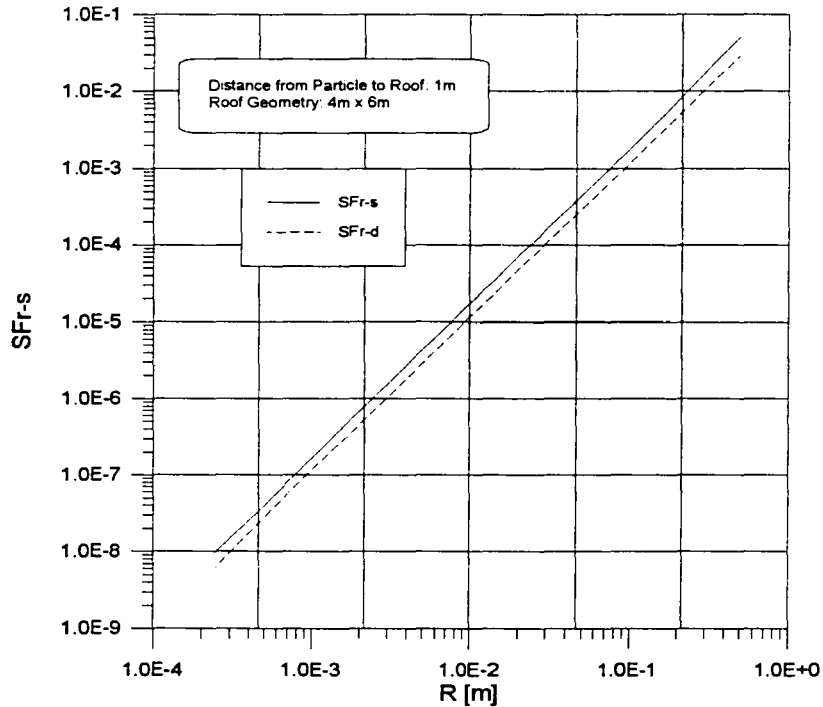


Figure 3.3. Comparison of shape factors from the roof to the sphere with the shape factor from the roof to the disk using the Monte Carlo method.

3.2.2. Analytical Equations

Because of the limitations using the Monte Carlo simulation to calculate the shape factors for very small particles, a literature review was conducted to see if any closed form, analytical expressions could be used to estimate the differences in the view factors from the roof to a sphere and from the roof to a circle. Four relevant analytical expressions were found and they are described next.

The shape factor from a sphere to a rectangle in which the center of the sphere lies along the normal to one corner of the rectangle, Figure 3.4 was developed by Tripp et al. (1962) as:

$$F_{12} = \frac{1}{4\pi} \sin^{-1} \left[\frac{1}{1 + Y^2 + Z^2 + Y^2 Z^2} \right]^{\frac{1}{2}} \quad (3.22)$$

Where,

$$Y = \frac{H}{C_x} \quad (3.23)$$

$$Z = \frac{H}{C_y} \quad (3.24)$$

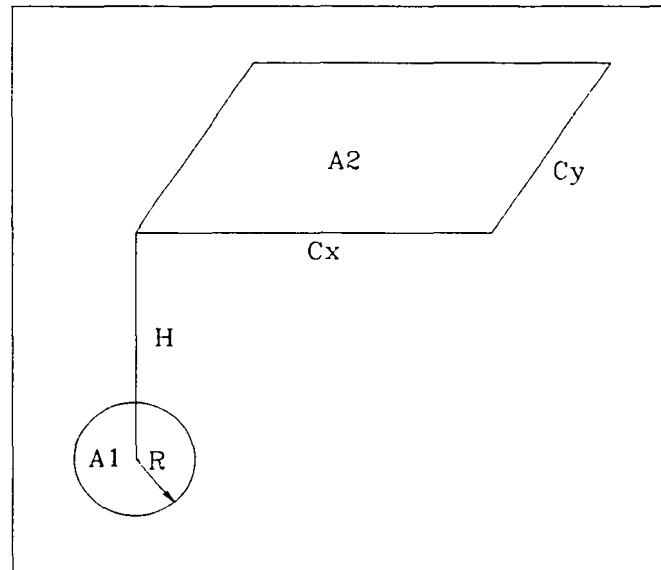


Figure 3.4. Shape factor between a finite sphere and a rectangle.

Equation (3.22) was programmed in a computer program and the results from these calculations were compared with the tables of shape factors published by Tripp et al. (1962). An exact agreement was found between the calculated and the published values (Figure 3.5).

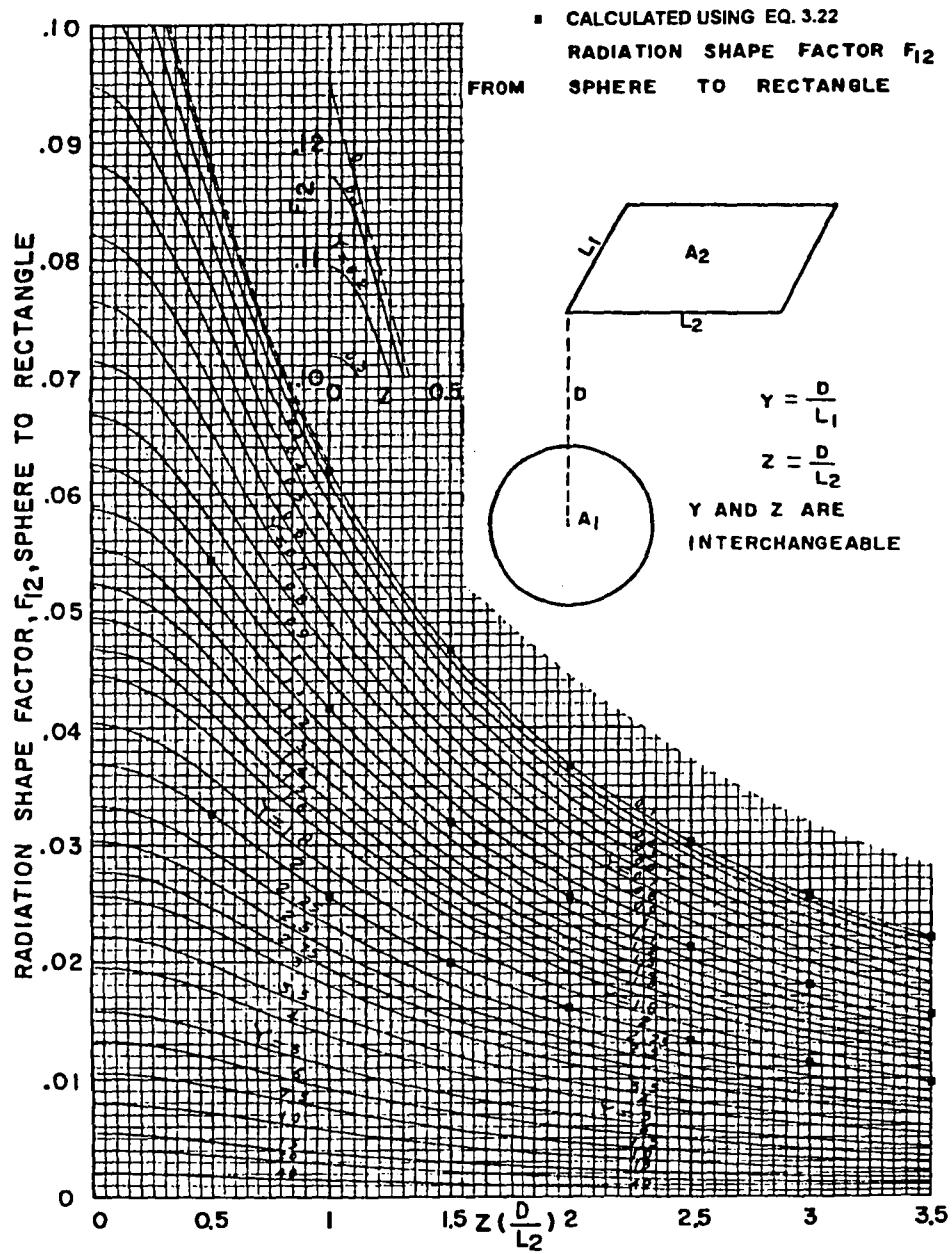


Figure 3.5. Comparison of tabulated and calculated values of the shape factor from a sphere to a rectangular plane using Equation (3.22).

The shape factor from a disk to a rectangular surface in which the center of the circle lies along the normal to one corner of the rectangle was equal to two times the shape factor from the circle to the right triangle formed by drawing one diagonal with origin in the corner normal to the center of the circle (Figure 3.6).

The shape factor from a disk to a right triangle was found by Tripp et al. (1962). This equation was valid only for the given geometry, and according to Figure 3.6 it was defined as:

$$F_{12} = \frac{1}{4\pi X^2} \left[\frac{1}{YZ} + (1 + X^2) \tan^{-1} \left(\frac{Z}{Y} \right) - \int_0^{\tan^{-1} \left(\frac{Z}{Y} \right)} \frac{1}{Z^2} \sqrt{\left(Z^2 + X^2 Z^2 + \frac{1}{\cos^2(\phi)} \right)^2 - \frac{4X^2 Z^2}{\cos^2(\phi)}} d\phi \right] \quad (3.25)$$

where ϕ is a dummy variable of integration and,

$$X = \frac{R}{H} \quad (3.26)$$

$$Y = \frac{H}{Cx} \quad (3.27)$$

$$Z = \frac{H}{Cy} \quad (3.28)$$

To find this shape factor, the integral in Equation (3.25) must be evaluated numerically.

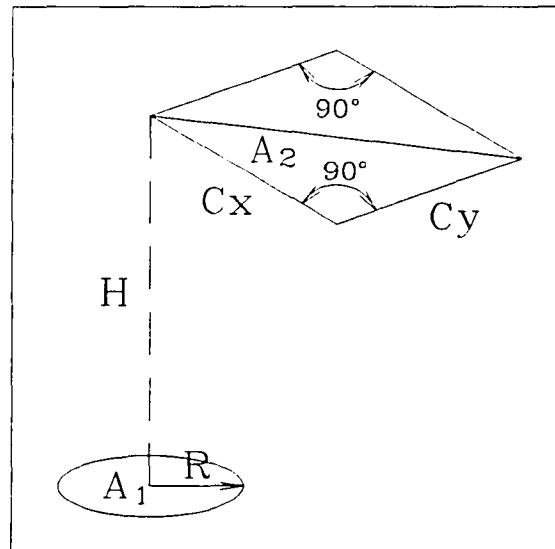


Figure 3.6. Geometry to calculate the shape factor from a disk to a right triangle.

Equation (3.25) was also programmed and the results of the program were compared with the values tabulated in the paper by Tripp. An exact agreement was also found between the published and the calculated values (Figures 3.7 through 3.9).

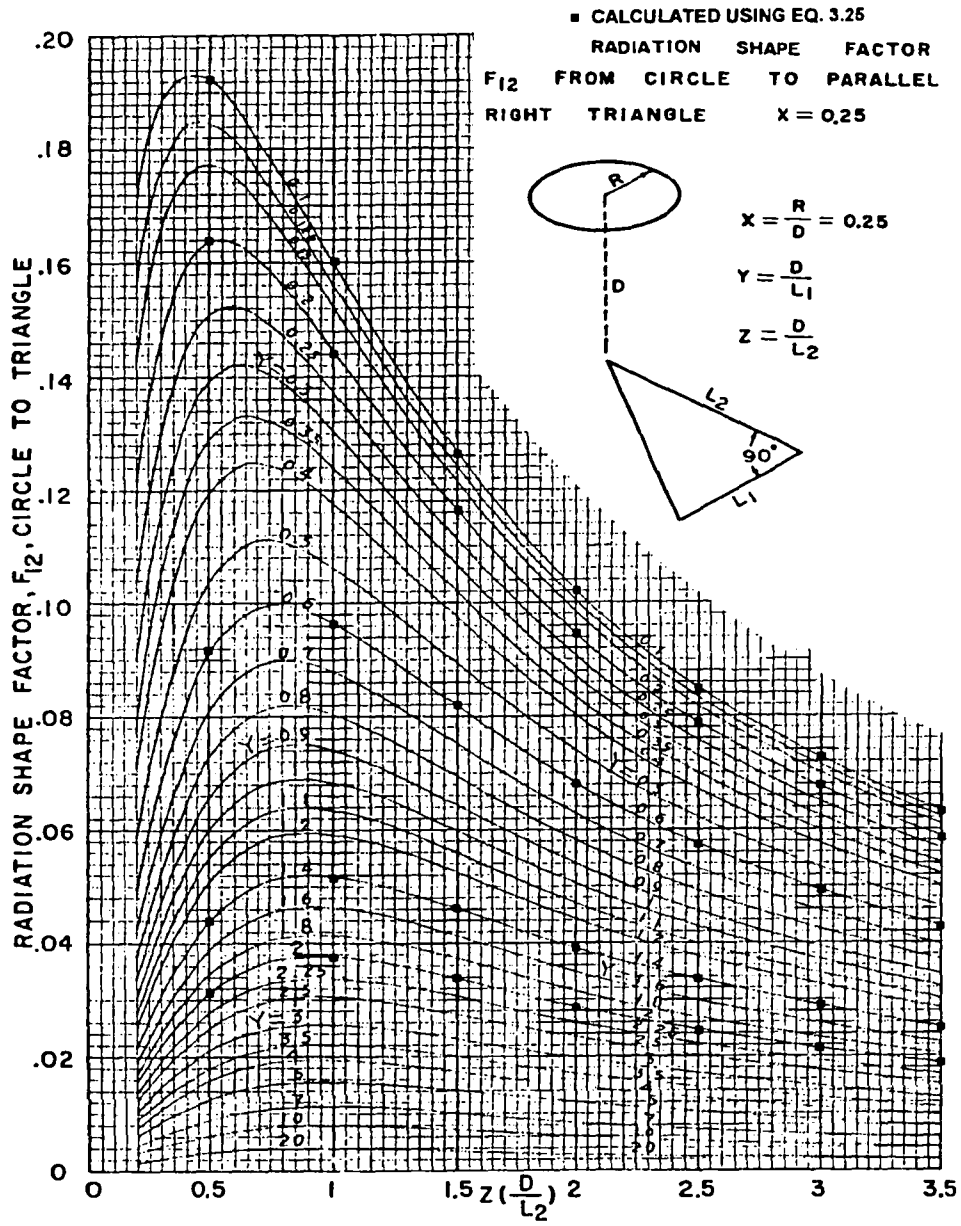


Figure 3.7. Comparison of tabulated and calculated values of the shape factor from a circle to a right triangle using Equation (3.25) with $X = 0.25$.

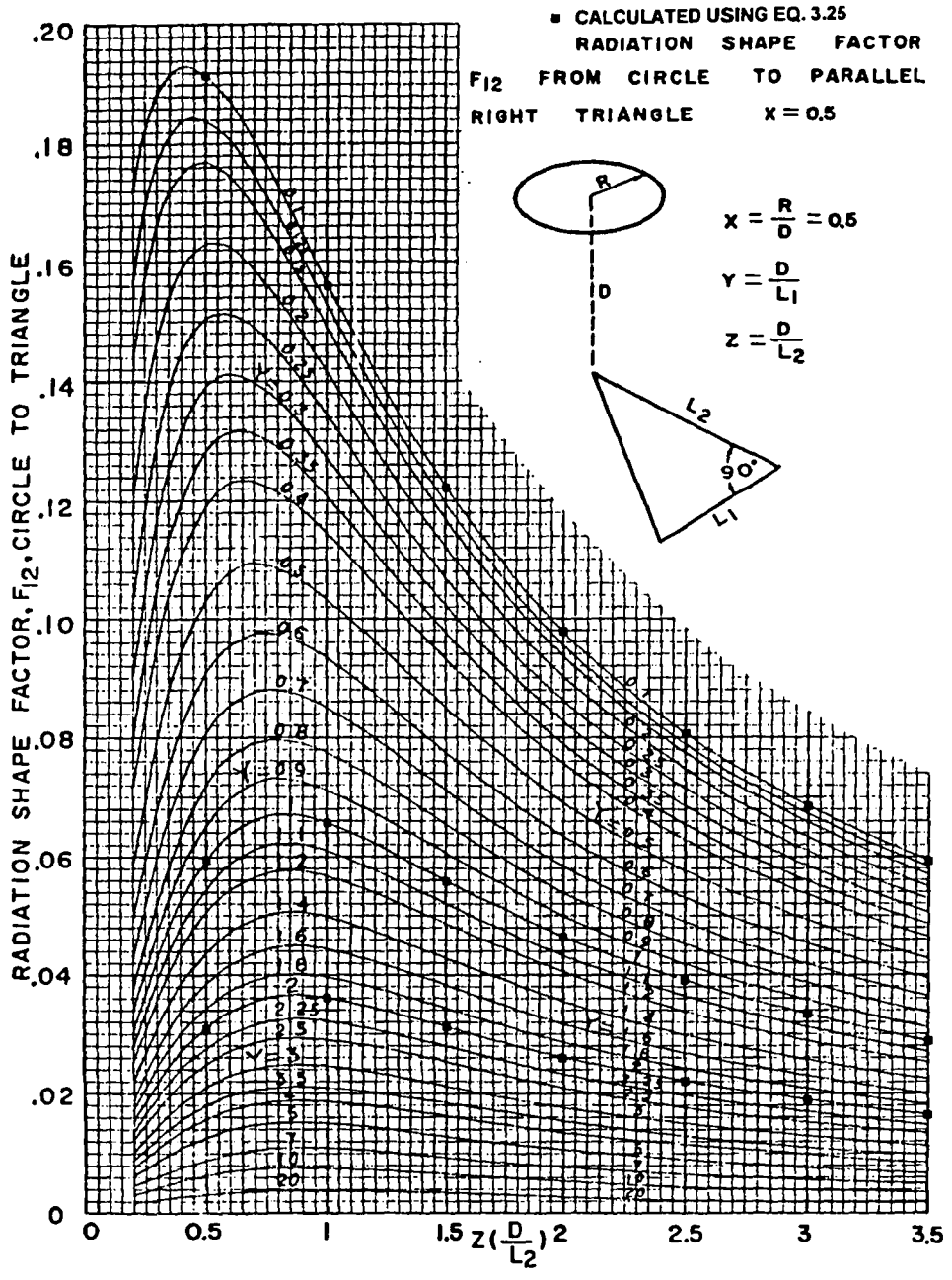


Figure 3.8. Comparison of tabulated and calculated values of the shape factor from a circle to a right triangle using Equation (3.25) with $X = 0.50$.

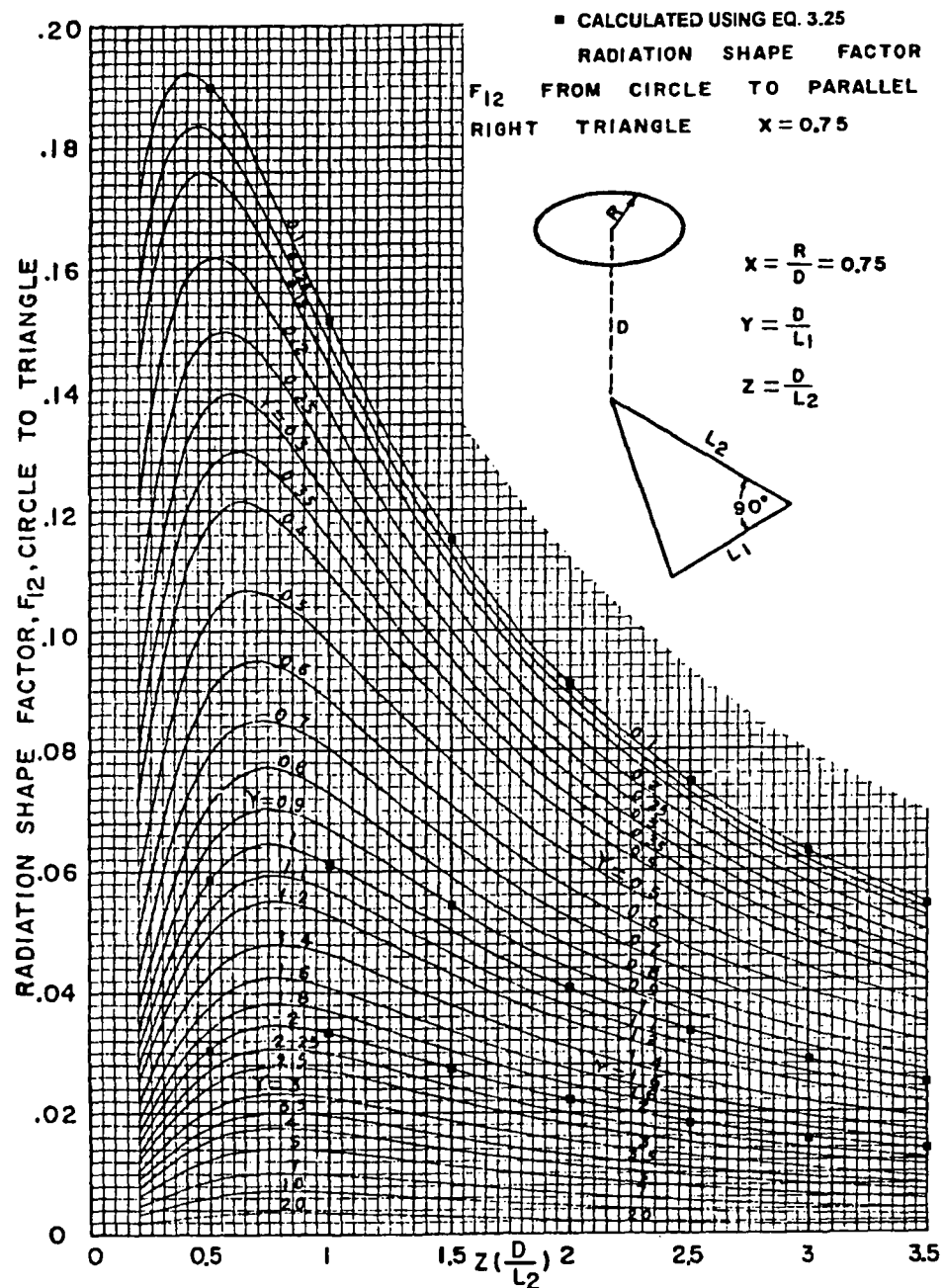


Figure 3.9. Comparison of tabulated and calculated values of the shape factor from a circle to a right triangle using Equation (3.25) with $X = 0.75$.

It was found that Equation (3.25) diverged for values of R less than 1.0×10^{-6} m. For this reason, to be able to calculate the shape factor from a rectangular plane to a circle for very small particles, it was necessary to simplify the problem, assuming that at the limit, the circle was an infinitesimal plane. In the same fashion with the previous shape factor, the view factor from an infinitesimal plane to a rectangular plane, could be calculated as twice the shape factor from the infinitesimal plane to any of the two triangles formed by drawing the rectangle's diagonal with origin in the vertex normal to the infinitesimal plane (Fig 3.10).

The shape factor from an infinitesimal area to a triangular plane (Figure 3.10) was found by Siegel and Howell (1981) as,

$$F_{d1-2} = \frac{X}{2\pi(1+X^2)^{\frac{1}{2}}} \tan^{-1} \left(\frac{X \tan \varphi}{(1+X^2)^{\frac{1}{2}}} \right) \quad (3.29)$$

where

$$X = \frac{Cx}{H} \quad (3.30)$$

$$\tan \varphi = \frac{Cy}{H} \quad (3.31)$$

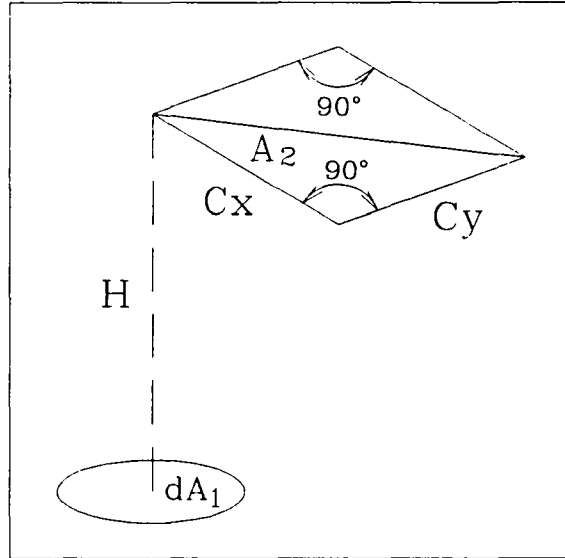


Figure 3.10. Geometry to calculate the shape factor from an infinitesimal plane to a right triangle.

Finally, the shape factor between two parallel planes (Figure 3.11) was found by Siegel and Howell (1981) as,

$$F_{12} = \frac{2}{\pi XY} \left\{ \ln \left[\frac{(1+X^2)(1+Y^2)}{1+X^2+Y^2} \right]^{\frac{1}{2}} + X\sqrt{1+Y^2} \tan^{-1} \left(\frac{X}{\sqrt{1+Y^2}} \right) \right. \\ \left. Y\sqrt{1+X^2} \tan^{-1} \left(\frac{Y}{\sqrt{1+X^2}} \right) - X \tan^{-1}(X) - Y \tan^{-1}(Y) \right\} \quad (3.32)$$

where:

$$X = \frac{C_x}{H} \quad (3.33)$$

$$Y = \frac{C_y}{H} \quad (3.34)$$

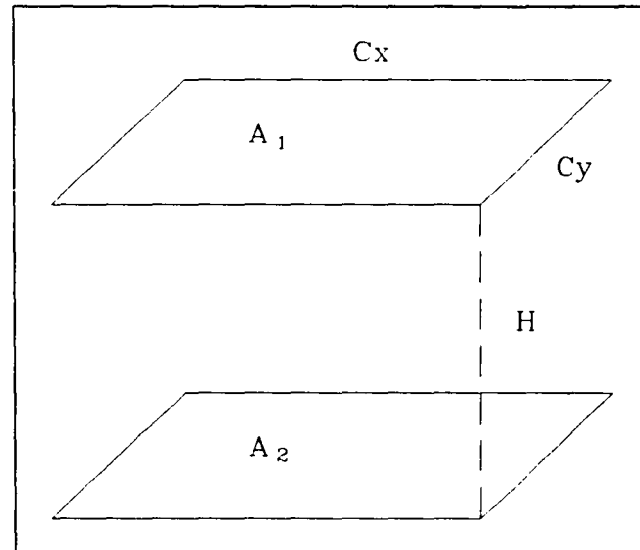


Figure 3.11. Geometry to calculate the shape factor between two parallel planes.

The subroutine *Analytic* calculated the shape factors from the roof to the spheres and circles using the relations described earlier. This subroutine called the function *Integra* to perform the numerical integration of Equation (3.25). The flow chart corresponding to this subroutine is shown in Figure 3.12.

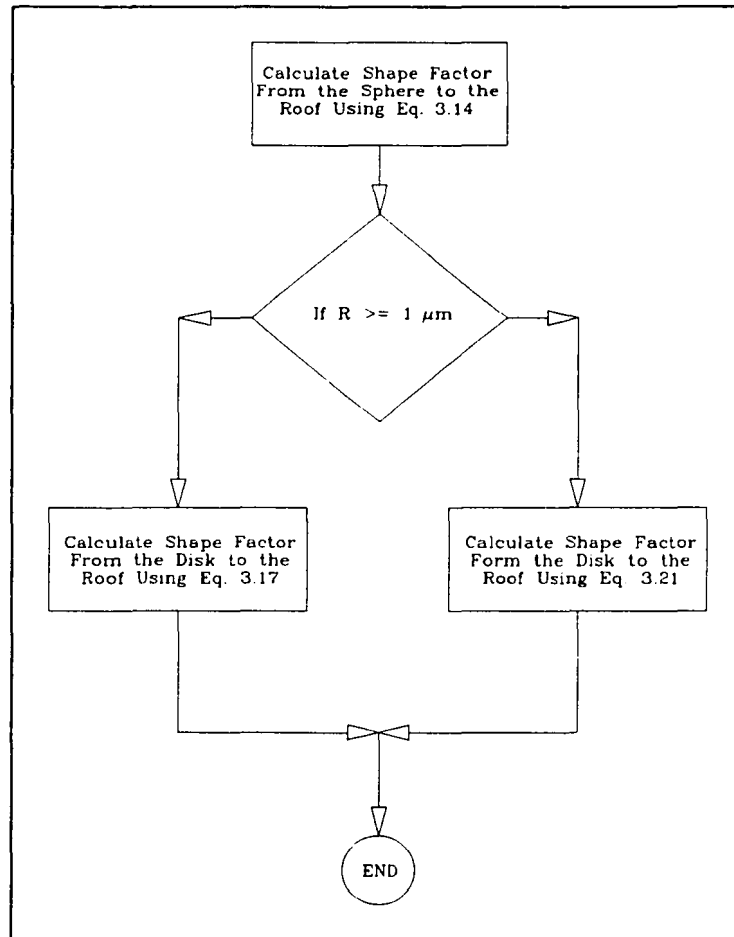


Figure 3.12. Flow chart of subroutine Analytic to calculate the shape factor from the roof to spheres and disks using Equations (3.22), (3.25), and (3.29).

The flow chart of the main program is shown in Figure 3.13. The main program set the geometrical dimensions of the attic, calculated the shape factor from the roof to the ceiling using Equation (3.32), set the diameters of the sphere and disk, and called the subroutines to calculate the shape factors using the Monte Carlo method and using the Equations (3.22) through (3.29). After the calculations were performed, the main program called the subroutine PrintRes to print out the results to a file. This procedure was repeated for several particle diameters.

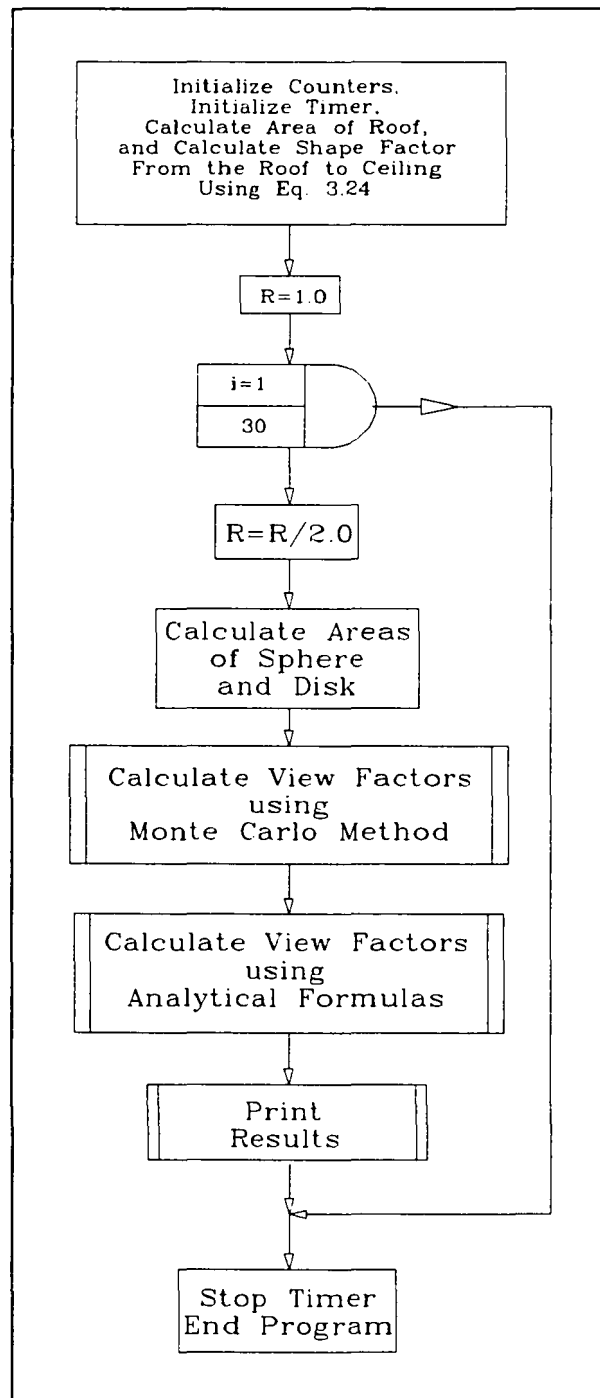


Figure 3.13. Flow chart of program MCar to calculate shape factors from the roof to the particles using the Monte Carlo method and analytical formulas.

A comparison of the shape factors calculated by the two methods described earlier are shown in Figures 3.14 and 3.15. The minimum radius shown was 1.2×10^{-4} m which was the minimum radius for which the Monte Carlo simulation produced useful results.

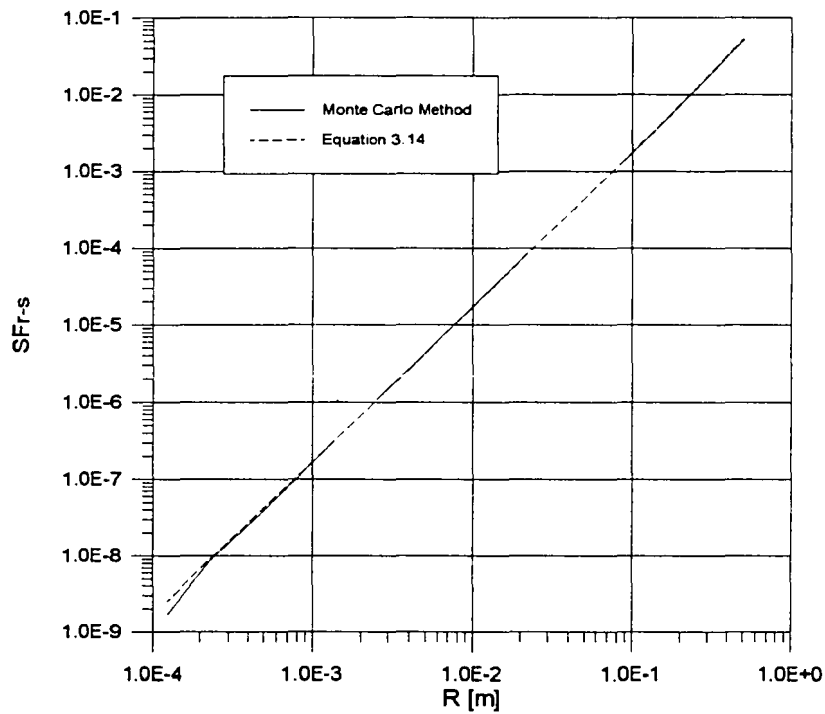


Figure 3.14. Comparison of the shape factors from the roof to the spheres calculated using the Monte Carlo method and Equation (3.22).

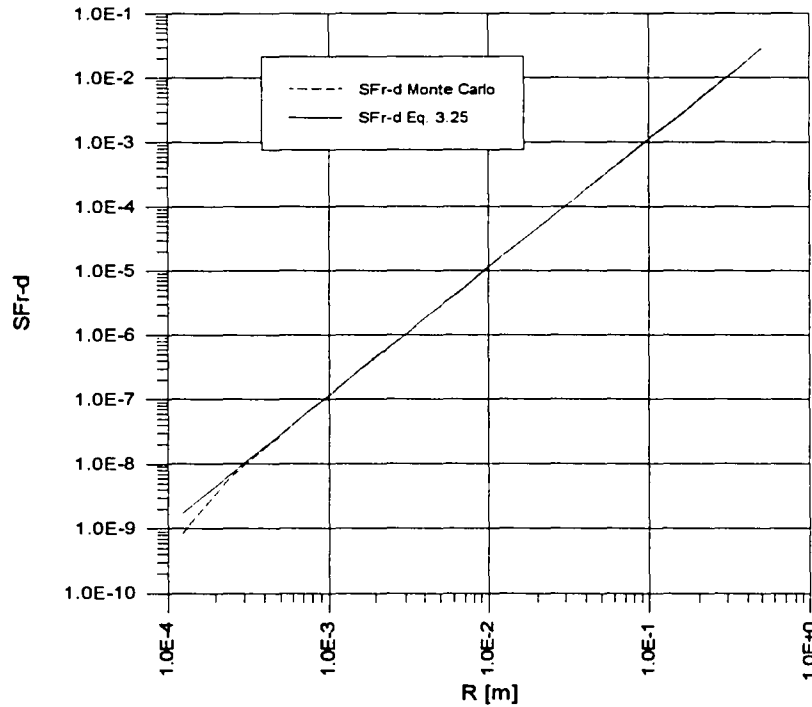


Figure 3.15. Comparison of the shape factors from the roof to the disks calculated using the Monte Carlo method and Equation (3.25).

3.2.3. Analysis of Results

The program calculated the shape factors of interest and the results obtained using the Monte Carlo Method agreed with the analytical formulae within 5 % for radii larger than 1.2×10^{-4} m when the number of hits to the intended target (disk or sphere) dropped to an insignificantly small (less than 10-15) number of hits.

Because of roundoff errors in the calculations of the shape factor from a disk to a rectangular plane using Equation (3.25), that equation could not be used for particle radius of less than about 1.2×10^{-4} m. For the case of the calculation of the shape factor from the roof to disks smaller than 1.2×10^{-4} m, a further simplification was needed and the particle was considered infinitesimal.

The Monte Carlo method consumed much more computing time than the analytical approach; nevertheless, this procedure proved to be easy to program, accurate, and fast for large diameters.

Figure 3.16 shows the shape factor from the roof to the sphere and from the roof to the disk calculated using Equations (3.22) and (3.25) as a function of the diameter of the disk and the sphere. For very small particle sizes, the shape factor from the roof to the circle was computed using Equation (3.29) (shape factor from an infinitesimal plane to a rectangle).

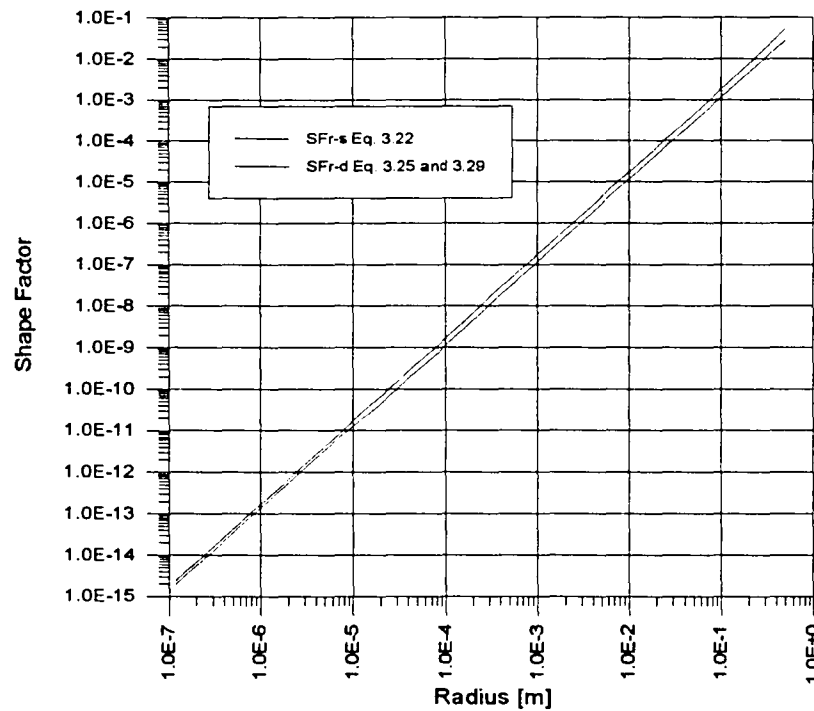


Figure 3.16. Comparison of the shape factor from the roof to a sphere with the shape factor from the roof to a disk a function of the sphere and disk diameters.

Figure 3.17 shows the ratio $SFr-s/SFr-d$ with $SFr-d$ calculated using Equation (3.25) and Equation (3.29) according to the radius size.

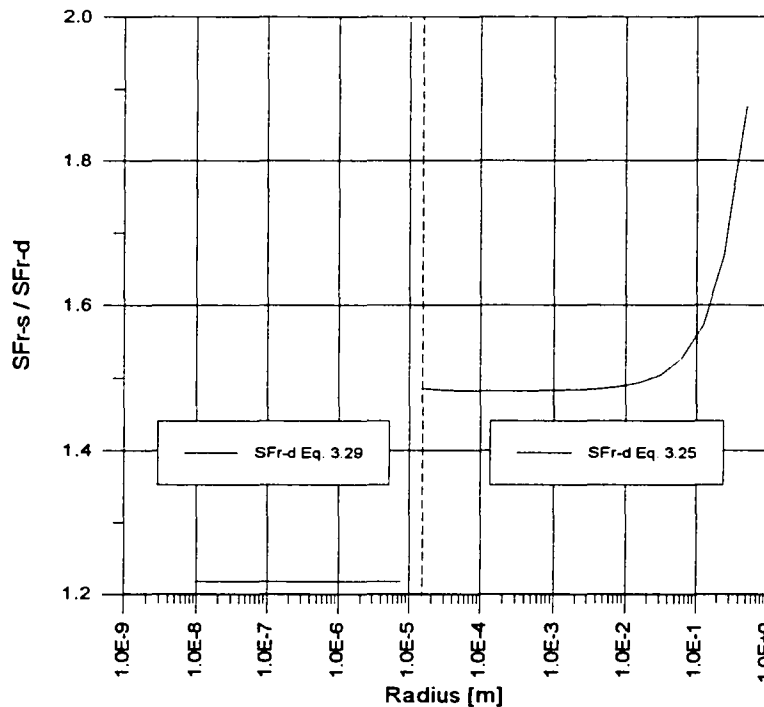


Figure 3.17. Ratio of the shape factor from a sphere to the roof to the shape factor from a disk to the roof as a function of the sphere and disk diameters.

Figure 3.17 shows that the ratio of the shape factors $SFr-s/SFr-d$ decreased as R decreased until about 2.0×10^{-3} , then became constant. It would be expected that the shape factor from the roof to the disk would approach asymptotically to the shape factor from the roof to an infinitesimal plane; but this was not the case, and there was a discontinuity in the results. For the range of diameters of particles considered in the present research, the relevant relationship is Equation (3.29) and the ratio $SFr-s/SFr-d$ was about 1.2. For the energy analysis, if the dust would be considered as spheres rather than disks, the dust would account for 20 % more effective area than for the flat case. To correct for the error in the assumption of the particles as plane disks, the model was fine tuned using a correction factor to the dust density so the particle's volume and cross sectional area was increased by increasing the density value used in the calculations by about 20 % of the measured density.

3.3. Assumption Analysis: Dust Particles Are at the Same Temperature as the Radiant Barrier

For validating this assumption, an experimental procedure was followed. The experimentation was designed to measure the temperature difference between the dust particles and the material of the radiant barrier.

The equipment used was:

1. One infrared camera with resolution of 2 °C, with adjustable target emissivity ranging from 0.1 to 1.0, attached to a VHS video recorder.
2. One piece of radiant barrier with emissivity $\epsilon_b=0.025$.
3. Black paint with known emissivity $\epsilon_p=0.88$.
4. Thermocouples type K attached to the underside of the barrier.
4. Dust with known emissivity $\epsilon_d=0.83$.
5. One data logger to record temperature signals from the thermocouples.
6. An infrared lamp for heating the barrier.

Three small thermocouples were placed in the underside side of a 7 cm by 7 cm piece of radiant barrier. A spot of black paint was placed on top of one of the thermocouples. Approximately two grams of dust with known emissivity were placed on top of the other thermocouple and the third thermocouple was beneath clean barrier. The piece of radiant barrier was then mounted on Styrofoam insulation.

The infrared measurement system had a movable pointer in the screen. This pointer provided a continuous reading of the surface's temperature at that point.

Because the infrared camera recorded the total incoming radiation through the lens, it actually recorded the radiation emitted by the sample plus the radiation emitted by the heat source that was reflected by the sample. To measure the actual temperatures in the point of interest of the sample, the temperatures were recorded when the heat source was off.

Because the infrared camera had no digital output, the infrared measurements were recorded in video cassette. To relate the temperatures from the data logger to the video recording, the clocks in both devices were synchronized. After the

experiment was concluded, it was possible to correlate the temperature in the surface to the temperatures in the underside of the barrier.

The procedure was conducted as follows: (1) The clocks in the data logger and the infrared video camera were synchronized. (2) The emissivity of the camera was set equal to the emissivity of the paint and the pointer was located on the paint spot. (3) The sample was heated until the temperature reached approximately 70 °C, at which point the heat source was turned off. (4) With the infrared camera viewing and recording the temperature changes of the paint, the data logger was started and kept on until the temperature in the paint was about 27 °C. At that time the experiment was concluded. (5) Afterwards, the video recording was played back and the temperature in the paint was obtained and matched with the readings of the data logger that measured the temperatures in the underside of the barrier (Figure 3.18).

The experiment was then repeated, but this time the emissivity of the camera was set to the emissivity of the dust, and the pointer of the camera was located on the dust spot.

The whole experiment was repeated ten times with the pointer (and the emissivity) on the dust and 10 times with the pointer (and the emissivity) on the black paint. The results from all the experiments could not be averaged because the initial state varied from experiment to experiment. Figure 3.19 shows a typical result for the temperature variation in the black paint spot and in the thermocouple under it. Figure 3.20 shows a typical temperature variation in the dust spot and in the thermocouple under the spot.

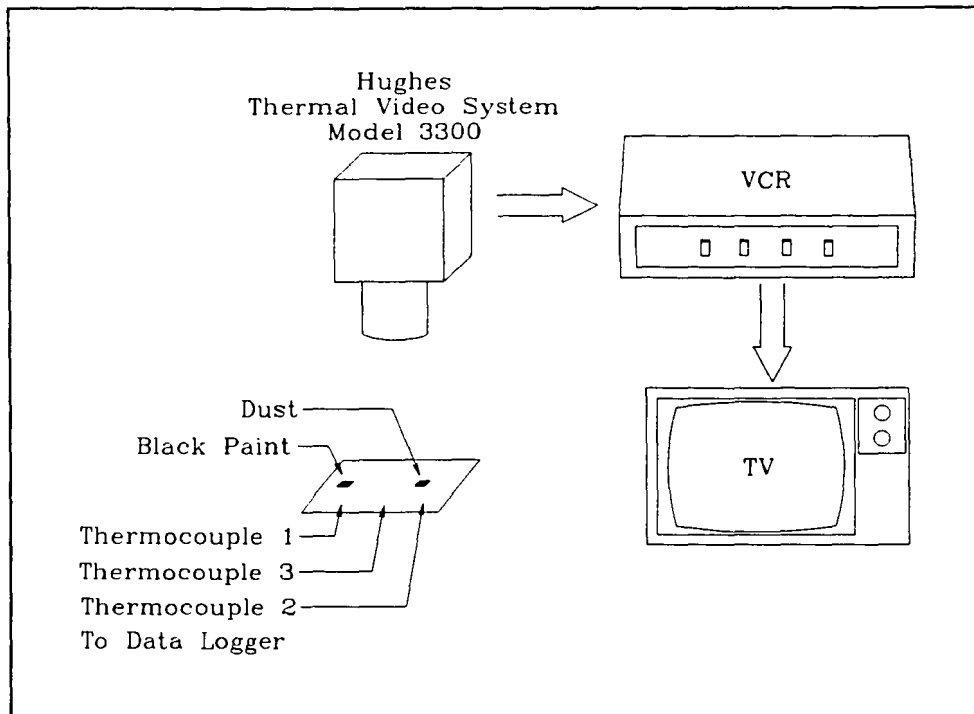


Figure 3.18. Experimental set-up to analyze the temperature difference between the dust particles and the barrier's material.

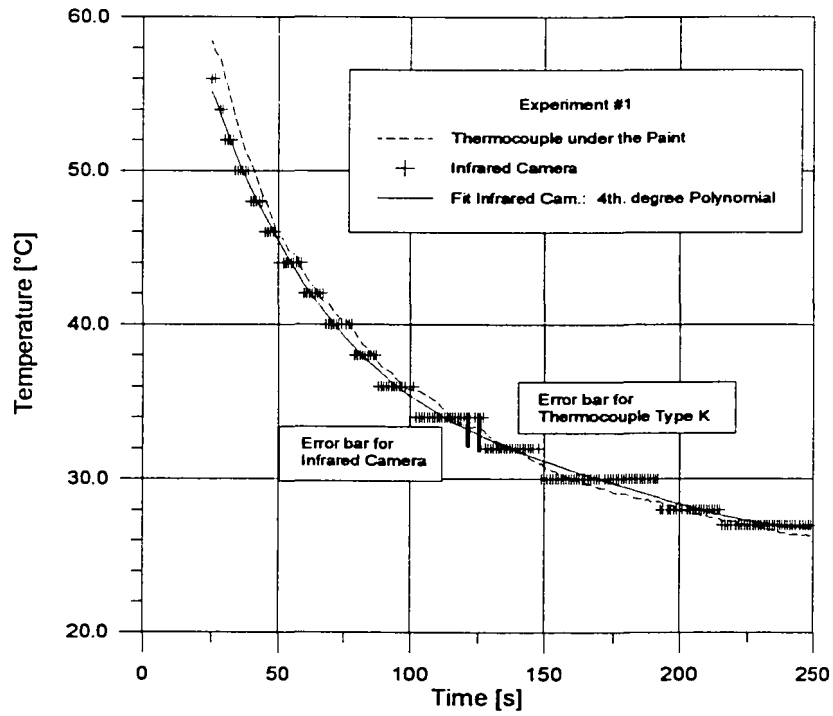


Figure 3.19. Typical temperature variation of the temperature recording of paint and a thermocouple under the barrier in the same spot.

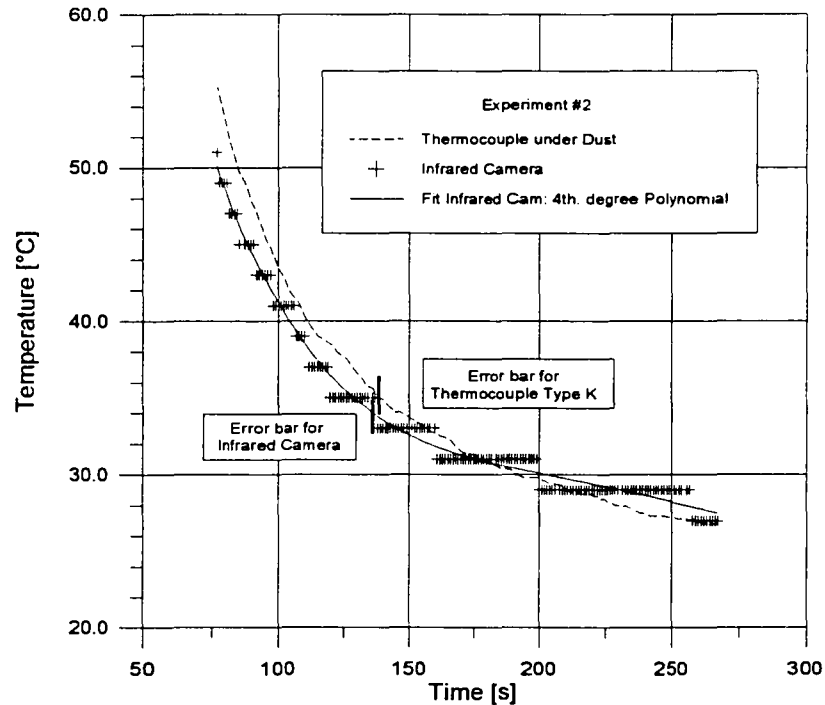


Figure 3.20. Typical temperature variation of the temperature recording of dust and a thermocouple under the barrier in the same spot.

Given that the resolution of the infrared camera was 2 °C (Hughes, 1991) and the accuracy of the thermocouples was 2.2 °C (Avallone and Baumeister, 1986), it was possible to detect temperature variations between the thermocouples due to the presence of the dust and the black paint. The temperature differences between the readings using the thermocouples and the video camera for the same spot were within the range of resolution of the equipment, (Figure 3.19 and 3.20). Furthermore, the temperatures approach to each other as the steady state is reached. In an attic the solar load changes slowly (variations in the range of hours), thus, it appeared reasonable to accept the assumption that the temperature of the radiant barrier material is equal to the temperature of the dust that settles on top of the barrier.

3.4. Model Methodology and Results

The early model developed by Noboa (1990) assumed that the dust particles laid in the nodes of an uniform array covering the entire attic floor. That model also

assumed that all the particles had the same radius, equal to the mean diameter of the Arizona Road Test Dust used in the experimental part of the research. In that model, dust superposition was modeled when the distance between the particles was smaller than the diameter of the particles, as shown in Figures 3.21 and 3.22. The thermal and heat transfer model treated each dust particle as an independent surface.

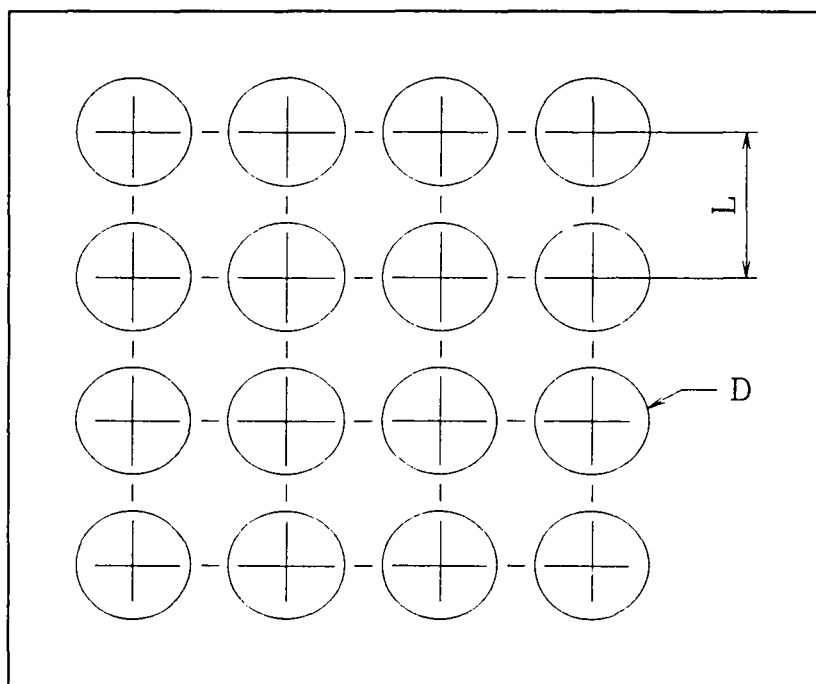


Figure 3.21. Early model of dust accumulation on top of HRB. No superposition present.

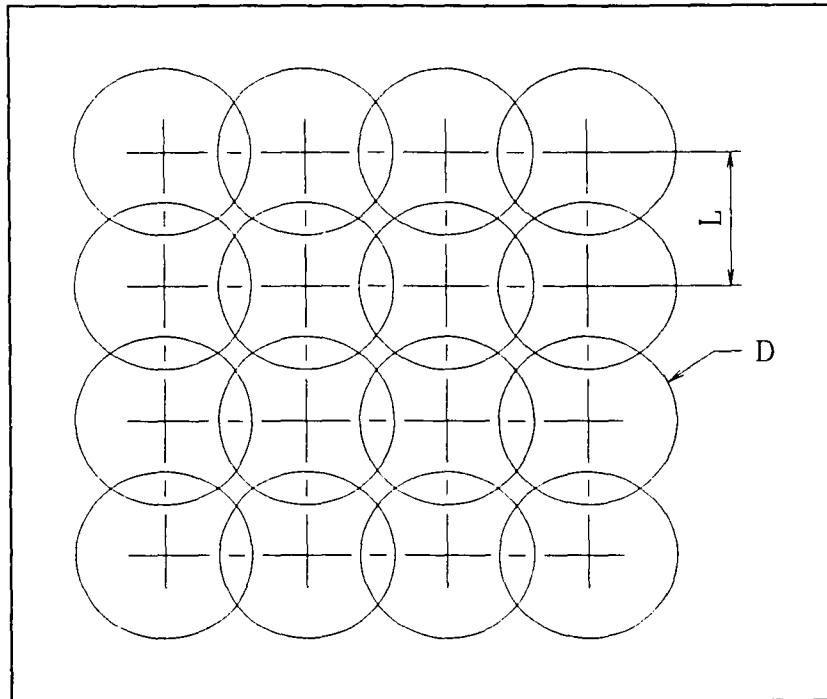


Figure 3.22. Early model of dust accumulation on top of HRB. Superposition present.

The early model applied the Net Radiation Method to the attic enclosure. A system of $N+4$ by $N+4$ system of equations was formed (where N is the number of dust particles considered), and the solution of that system of equations lead to the determination of the heat fluxes in the enclosure. Once the heat fluxes were known, an equivalent system of equations was formed, but in this case all the nodes representing the dust particles and the node corresponding to the clean barrier were replaced by a single node representing the radiosity of the dusty radiant barrier. In this new system of equations the only unknown was the radiosity of the dusty barrier. Once this system of equations was solved, the absorptivity of the dusty barrier could be calculated.

Further analysis of the results lead to an interesting finding: the absorptivity of the dusty barrier is a **linear** function of the ratio of area covered by dust. This results were corroborated by an experimental work by Cook et al. (1989). The relationship found was of the form,

$$\alpha_{db} = \alpha_b + (\alpha_d - \alpha_b) \cdot f_p \quad (3.35)$$

This relationship could be used to determine the overall absorptivity degradation of the radiant barrier and more important, the new model did not need to solve the radiation exchange in the attic, but required only to accurately find the ratio of barrier area covered by dust.

4. DUST CHARACTERIZATION

4.1. Introduction

Dust size distribution had to be accurately measured and characterized because the model developed in this research relied heavily on the physical properties, and particularly on the physical dimensions of the dust. To assess the validity of the model, a portion of the experimental part of this research used a commercially available dust to simulate natural dust accumulation on top of a HRB. The test dust manufacturer provided dust size distribution data based on mass. The model developed in this research used the particle size distribution based on the number of particles. In this section the manufacturer's mass distribution data were converted into the number of particles in each particular size range for further use in the research.

4.2. Dust Characterization

There were two commercially available test dust types: Coarse and Fine. The particle size distributions provided by the manufacturer on a mass basis (Weiss and Frock, 1975) are shown in Tables 4.1 and 4.2 for the fine and coarse dust, respectively. The columns labeled "Diameter Range" represented the minimum and maximum particle diameter expected to be found in that range. The column labeled "Mean Diameter" corresponded to the mean diameter of the range. The column labeled "Difference" corresponded to the statistical probability of finding dust with diameters within the specified range. The cumulative data represented the probability of finding dust with diameter between zero and the upper limit of the specified range. The same data are presented in graphical form in Figures 4.1 and 4.2.

Table 4.1. Particle size distribution of fine dust in mass basis.

Diameter Range [μm]		Mean Radius [μm]	Cumulative Probability	Probability Difference
0.00	2.8	0.700	0.141	0.141
2.8	3.9	1.675	0.245	0.104
3.9	5.5	2.350	0.350	0.105
5.5	7.8	3.325	0.420	0.070
7.8	11.0	4.700	0.511	0.091
11.0	16.0	6.750	0.599	0.088
16.0	22.0	9.500	0.690	0.091
22.0	31.0	13.25	0.780	0.090
31.0	44.0	18.75	0.862	0.082
44.0	62.0	26.50	0.936	0.074
62.0	88.0	37.50	0.990	0.054
88.0	125.0	53.25	1.000	0.010
125.0	176.0	75.25	1.000	0.000

Table 4.2. Particle size distribution of coarse dust in mass basis.

Diameter Range [μm]		Mean Radius [μm]	Cumulative Probability	Probability Difference
0.00	2.8	0.700	0.052	0.052
2.8	3.9	1.675	0.086	0.034
3.9	5.5	2.350	0.130	0.044
5.5	7.8	3.325	0.175	0.045
7.8	11.0	4.700	0.217	0.042
11.0	16.0	6.750	0.276	0.059
16.0	22.0	9.500	0.356	0.080
22.0	31.0	13.25	0.449	0.093
31.0	44.0	18.75	0.574	0.125
44.0	62.0	26.50	0.704	0.130
62.0	88.0	37.50	0.855	0.151
88.0	125.0	53.25	0.964	0.109
125.0	176.0	75.25	1.000	0.036

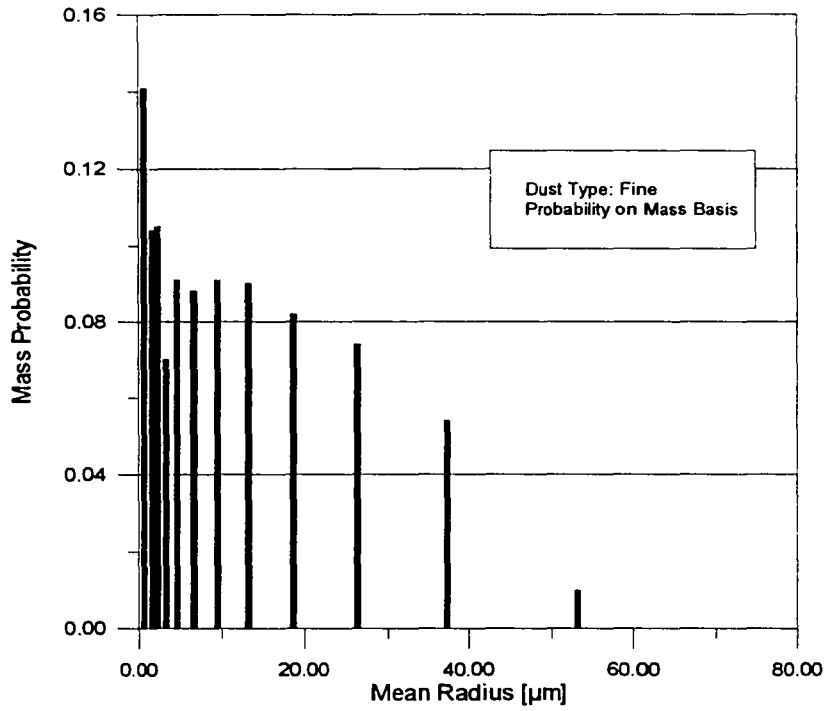


Figure 4.1. Particle size distribution of fine dust on a mass basis.

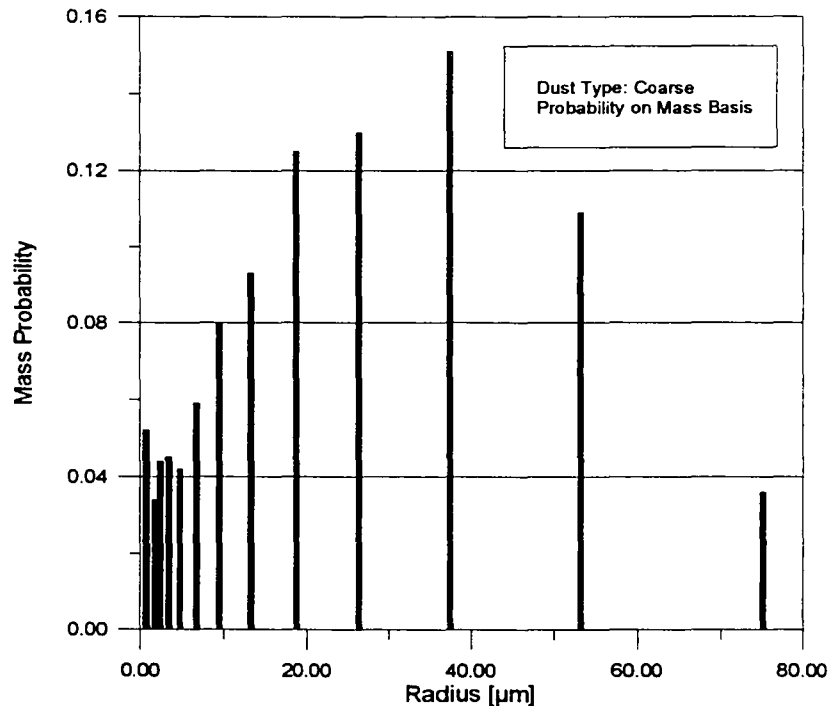


Figure 4.2. Particle size distribution of coarse dust on a mass basis.

From an analysis of the data, it was possible to note that the fine dust had more mass made up of small particles than the coarse dust. This fact was specially evident when the mean diameter of the samples was calculated. The mean diameter of the fine dust was equal to 19.8 μm and the mean diameter of the coarse dust was equal to 45.8 μm , more than double the mean diameter of the fine dust. Because of the smaller diameter of the fine dust, it degraded the absorptivity of the radiant barrier faster than the coarse dust. The analysis of photomicrographs suggested that the small particles could fill the gaps between the particles easier than the larger particles. Thus, for the same dust loading [mg / cm^2], the fine dust produced larger absorptivities.

Given that the program to simulate dust accumulation on top of the radiant barrier used the dust size distribution as the number of particles in each diameter range, the mass probability had to be converted to number of particles. For a sample of one unit of volume (1 m^3), the number of particles, $np(j)$, present in each diameter range Diameter(j), was:

$$np(j) = \frac{\text{Mass Probability (j)}}{\text{Volume of Sphere (j)}} \quad (4.1)$$

The Volume of Sphere (j) was calculated using the radius of the average particle for the range (j). Thus, the fraction of particles, $f(j)$, in any given diameter range j was given as:

$$f(j) = \frac{np(j)}{\text{Total Number of Particles}} \quad (4.2)$$

where the total number of particles was calculated as the sum of the number of particles in each particle range. The fraction of particles in each size range for the two types of dust is shown in Tables 4.3 and 4.4, and the same data are presented in graphical form in Figure 4.3 and 4.4.

Table 4.3. Particle size distribution of fine dust in number of particles basis.

Diameter Range [μm]		Mean Radius [μm]	Cumulative Probability	Probability Difference
0.00	2.8	0.700	0.92475118	0.92475118
2.8	3.9	1.675	0.97453507	0.04978389
3.9	5.5	2.350	0.99273567	0.01820060
5.5	7.8	3.325	0.99701941	0.00428374
7.8	11.0	4.700	0.99899114	0.00197173
11.0	16.0	6.750	0.99963482	0.00064368
16.0	22.0	9.500	0.99987358	0.00023876
22.0	31.0	13.25	0.99996062	0.00008704
31.0	44.0	18.75	0.99998860	0.00002798
44.0	62.0	26.50	0.99999755	0.00000895
62.0	88.0	37.50	0.99999985	0.00000230
88.0	125.0	53.25	1.00000000	0.00000150
125.0	176.0	75.25	1.00000000	0.00000000

Table 4.4. Particle size distribution of coarse dust in number of particles basis.

Diameter Range [μm]		Mean Radius [μm]	Cumulative Probability	Probability Difference
0.00	2.8	0.700	0.90521294	0.90521294
2.8	3.9	1.675	0.96620009	0.06098715
3.9	5.5	2.350	0.98874424	0.02254415
5.5	7.8	3.325	0.99475416	0.00600992
7.8	11.0	4.700	0.99797475	0.00322059
11.0	16.0	6.750	0.99915905	0.00118430
16.0	22.0	9.500	0.99961172	0.00045267
22.0	31.0	13.25	0.99984273	0.00023101
31.0	44.0	18.75	0.99994056	0.00009783
44.0	62.0	26.50	0.99997778	0.00003722
62.0	88.0	37.50	0.99999386	0.00001608
88.0	125.0	53.25	0.99999955	0.00000569
125.0	176.0	75.25	1.00000000	0.00000045

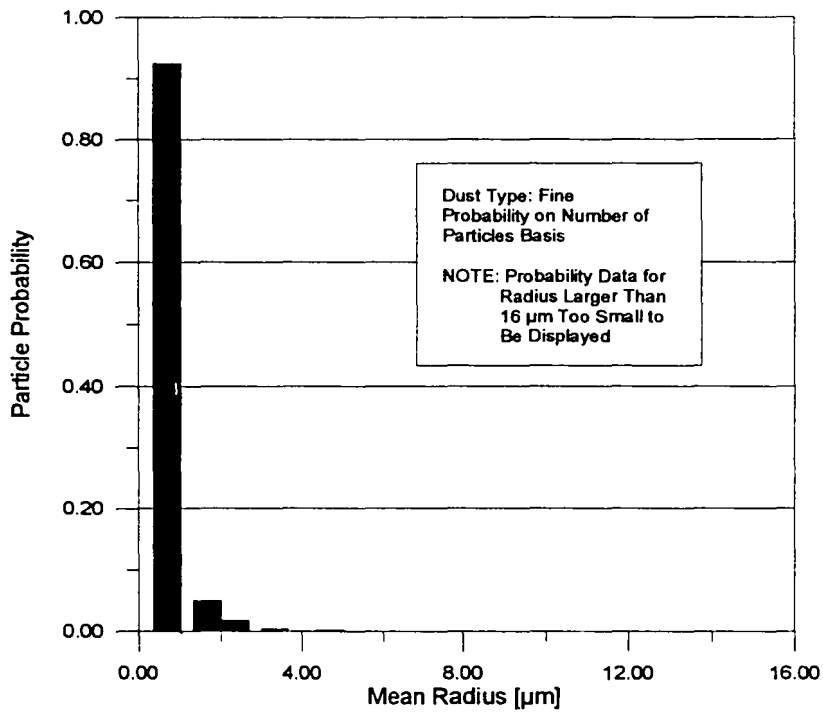


Figure 4.3. Particle size distribution of fine dust on a number of particles basis.

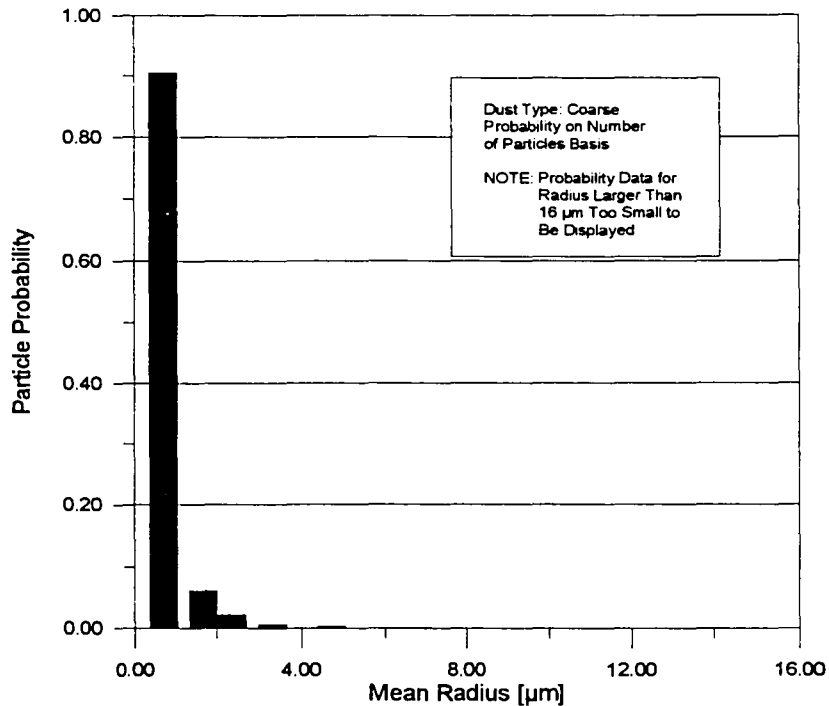


Figure 4.4. Particle size distribution of coarse dust on a number of particles basis.

Given that a large number of small particles would contribute a small portion of mass of dust, it was expected that most of the particles were of the small diameter and a very small percent of particles were of the larger sizes. To be able to get useful information in the larger particle ranges, the calculations were performed using 15 digits of accuracy. It should also be noted that in the use of these data in the computer model to predict the dust influence in the absorptivity of the radiant barrier, the random numbers generated in the computer differed in all the 15 digits.

4.3. Summary

Photomicrographic analysis had shown that natural dust differs from the Arizona Test Dust mainly in the natural occurrence of fibers and other long particles that are virtually absent in the Arizona Test Dust. In general, fibers account for a small percent of the particles, maybe 5 % or less, depending on the location.

Comparison of Figures 4.1 and 4.2 showed the difference between the two dust types. Fine dust contained more smaller size particles, and the bulk of the mass was made of particles with diameters less than 8 μm , while most of the particles of the coarse dust were made of particles ranging from 18 to 53 μm . As noted earlier, this characteristic caused fine dust to increase the radiant barrier absorptivity (and correspondingly the absorptivity) faster than the coarse dust, e. g. a given dust loading [mg / cm^2] of fine dust produced larger absorptivities than the same loading of coarse dust. Photomicrograph analysis showed that the possible reason for this phenomena was that small particles could fill the spaces between particles better than larger ones that tended to overlap.

Comparison of Figures 4.3 and 4.4 showed a very different picture. It can be seen that in both dust types, more than 90 % of the particles were of the smallest diameter, and there were not much difference in the percent of particles in each diameter range. It is worth noting that one 75 μm diameter particle covered an equivalent area of 11,480-0.7 μm particles. Thus, even though the percent difference on a particle basis between the two dust types was small, that small difference produced noticeable changes in the area covered by dust and in the resulting absorptivity.

5. MODEL TO PREDICT THE ABSORPTIVITY OF DUSTY RADIANT BARRIERS

5.1. Introduction

As explained in section 3, the early model assumed that the dust particles laid on the surface of the radiant barrier in the nodes of a rectangular and uniform array. The model assumed that all the particles were of the same radius which was equal to the mean radius of the dust to be analyzed. To simulate heavy dust loading, the array was modified to include more rows and columns but the particles would always lay in the nodes of the rectangular array. Given that geometrical assumption, superposition of the particles occurred when the distance between the rows and columns was smaller than the diameter of the particles to be analyzed. The ratio of area covered by dust to the area of the barrier was found using the appropriate geometrical relationships.

The modeling of dust accumulation by using a random particle size distribution and random location of the particles on the barrier is described in this section.

5.2. Analytical Approach

An analytical solution to the problem of finding the area of dust superposition between overlapping particles was sought using elementary geometry. A solution was easily obtained for the case when two to three particles overlap, but keeping track of successive overlapping of particles was nontrivial. It was necessary to make the model discern between partial, complete and null superposition and be able to calculate the area of barrier that was covered by dust, regardless of the amount of dust. An example of the complexity of this problem is shown in Figure 5.1 where it is possible to note that superposition occurred.

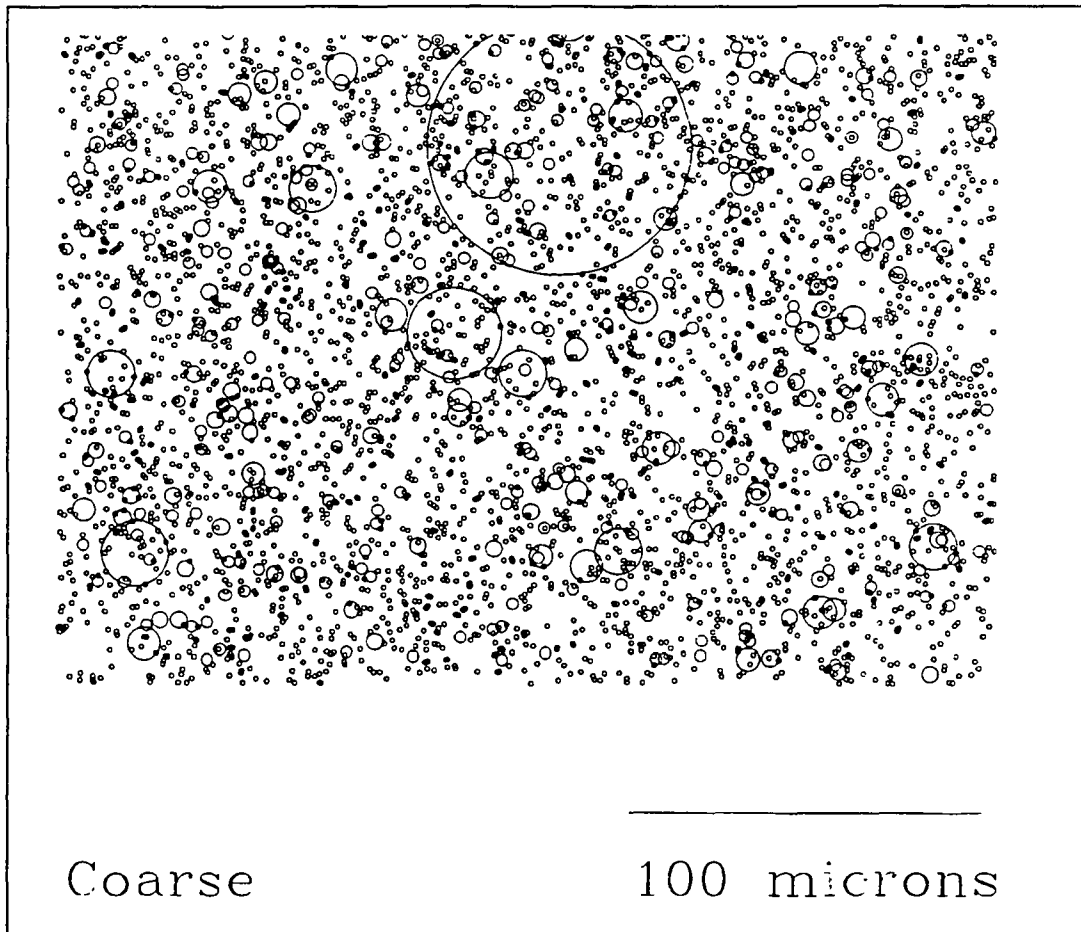


Figure 5.1. Typical dust particle superposition. NOTE:
Partilces are pictured as transparent circles to illustrate
overlapping.

5.3. Graphical Method

The next step was to try to solve the problem graphically. Given that the graphical method is an approximation of reality, the first decision to be made was to set a resolution criteria for the method. This criteria included two requirements: (1) the sample area should be at least 25 mm² to have a good representation of the random nature of the phenomena to be modeled, and (2) in that frame, it was required to represent the area of one circle with radius 0.7 μm (the minimum radius considered

by the particle size analysis of the Arizona Road Test Dust) with an accuracy of 5 %. The resolution criteria meant that the calculated area of this particle should be within the range $1.539 \pm 0.077 \mu\text{m}^2$ or within the range 1.462 to $1.616 \mu\text{m}^2$.

The first attempt to develop this method was done by using a Pascal program in which the dust particles were drawn on a graphical screen in random locations and radii according to the particle size distribution of the dust that was to be analyzed. After all the particles were located on the screen, the program counted the number of pixels that have been placed on the screen. The ratio of area covered by the dust was then equal to the number of pixels drawn, divided by the total number of pixels of the screen.

This graphical method had two serious limitations. First, using the VGA screen of the PC, the resolution was very low; thus, the screen could not comply with the resolution criteria previously set. In a 25 mm^2 sample, the smallest particle that could be drawn with the 5 % accuracy required was a particle of radius 1.2 mm. That was about 1700 times the size of the smallest particle ($0.7 \mu\text{m}$, see tables 4.1 and 4.2) required to be represented. To improve the accuracy, the particles had to be drawn in a larger scale, but this, in turn, made the sample of analysis too small for practical purposes. Secondly, because the screen had 640 pixels in the x direction and 480 pixels in the y direction, to be able to represent circles, they had to be drawn as ellipses having an eccentricity factor of $480 / 640$. The use of a work station screen could improve the accuracy but not enough to comply with the resolution criteria assumed. Because of these limitations, this method was abandoned.

5.4. AutoCAD Solution

An AutoCAD procedure was developed to address the limitations of the graphical method. AutoCAD had the Advanced Modeling Extension (AME) module which provided capabilities to model solids. Using this module, it was possible to find the volume of a solid drawn in three dimensions.

The SOLMASSP command calculated and displayed the mass properties of a set of selected solids and regions. AME listed the solids and regions of the selection set separately.

The mass properties displayed for solids were mass, volume, bounding box, centroid, moments of inertia, products of inertia, radii of gyration, and principal moments with corresponding principal directions. Calculations were based on the current User Coordinate System (UCS).

AME displayed the centroid (center of mass or area) on the drawing as a point in the current layer. It was possible to change the style of this point by setting the PDMODE variable to the point type required. The point was sized according to the PDSIZE variable.

5.4.1. Accuracy of Solid Volume Calculations

Given that the calculation was based on a ray classification technique described next, the volume calculation of solids was an approximation.

To calculate the volume of solids, the program fired rays at the solid modeled and classified them according to whether they intersected the solid or not. Two settings affected the accuracy of the ray classification: the density of the rays and the direction that they are fired at the solid. The first setting was the density of the rays, called the "subdivision level," and was set by the SOLSUBDIV variable. The direction of the ray projection was called the "decomposition direction" and was set by the SOLDECOMP variable.

The subdivision level determined the number of partitions to be made to the box enclosing the solid. The enclosing box was the smallest possible box that fully enclosed the volume of the solid being analyzed. The number of divisions N_d was defined according to the following formula, where l was the subdivision level.

$$Nd = (2^1)^2 \quad (5.1)$$

As the details of the solid modeled became smaller with respect to the enclosing box (or when the evaluated solid was small compared to the size of the primitives in the Constructive Solid Geometry (CSG) tree), SOLMASSP would not give accurate results at low subdivision levels. It was necessary to use the highest value of SOLSUBDIV (equal to 8) to simulate the dust accumulation.

One ray was fired randomly for each subdivision and was then classified according to where it lay with respect to the solid. If a ray did not lie on or within the solid, the subdivision was disregarded.

Because rays were fired randomly, there was some error intrinsic to the random nature of the method, which was not reflected in the error estimation. This random error occurred when, by chance, rays hit small portions of the solid and by chance, as well, the rays missed bulky portions of the solid. This was particularly true when the calculations involved curved solids. To minimize this problem, the model made all the solids with the Z direction being a straight line. The error estimations are shown (enclosed in parentheses) in the report generated by the SOLMASSP command (Table 5.1).

Table 5.1. Typical output of AutoCAD SOLMASSP command.

Ray projection along Z axis, level of subdivision: 8.	
Mass:	171.8 gm
Volume:	21.86 cu cm (Err: 0.00116)
Bounding box:	X: 1 -- 6 cm Y: 1 -- 6 cm Z: 0 -- 1 cm
Centroid:	X: 3.5 cm (Err: 0.0064) Y: 3.5 cm (Err: 0.0064) Z: 0.5 cm (Err: 2.654e-05)
Moments of inertia:	X: 2565 gm sq. cm (Err: 7.808) Y: 2565 gm sq. cm (Err: 7.807) Z: 5015 gm sq. cm (Err: 11.02)
Products of inertia:	XY: 2104 gm sq. cm (Err: 5.67) YZ: 300.6 gm sq. cm (Err: 0.5498) ZX: 300.6 gm sq. cm (Err: 0.5497)
Radii of gyration:	X: 3.864 cm Y: 3.864 cm Z: 5.403 cm
Principal moments (gm sq. cm) and X-Y-Z directions about centroid:	
	I: 417.3 along [0 1 0]
	J: 806.1 along [0 0 1]
	K: 806.1 along [1 0 0]

The second setting that affected the accuracy of mass properties was the decomposition direction. This setting determined the direction in which the rays were fired. Rays were fired parallel to the decomposition direction (Subdivision of the enclosing box was perpendicular to the decomposition direction).

The subdivision was optimized by choosing the decomposition direction parallel to the longest dimension of the solid and choosing the direction along the axis perpendicular to dust plane. This ensured that the subdividing boxes were small, thereby reducing the likelihood of erroneous ray classification.

5.4.2. Model Description

The model in AutoCAD was programmed in Lisp, which was the programming interface for AutoCAD. The program read a data file containing the x and y coordinates of the location of the centers of the particles and the corresponding radius. The program then located the particles in the drawing, and finally calculated the total volume (area) of the solids generated.

Figures 5.2 and 5.3 show the representation of four particles. These figures were created using the command SOLBOX to create the rectangular parallelepiped or box. The box was made, according to the resolution criteria, with the X-Y face formed by a square with sides equal to 5 mm. The Z height was set equal to 1 mm. The cylinder was drawn with the chosen radius and a height of 1 mm. Finally, the command SOLSUBS subtracted the cylinder from the box. Prior to performing the SOLMASSP calculation, the variable SOLDECOMP was set to the Z axes and the variable SOLSUBDIV was set to the maximum value, equal to eight.

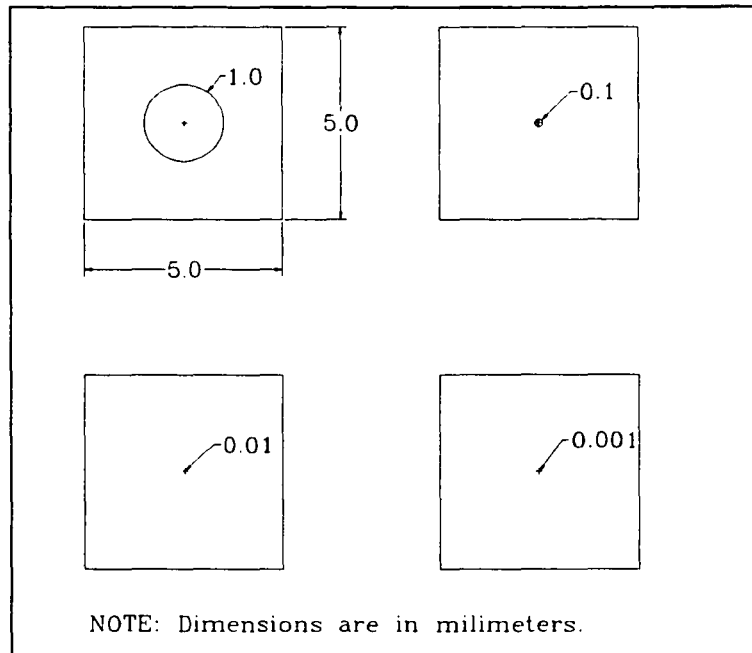


Figure 5.2. Representation of dust particles of different radius in a sample area of 25 mm².

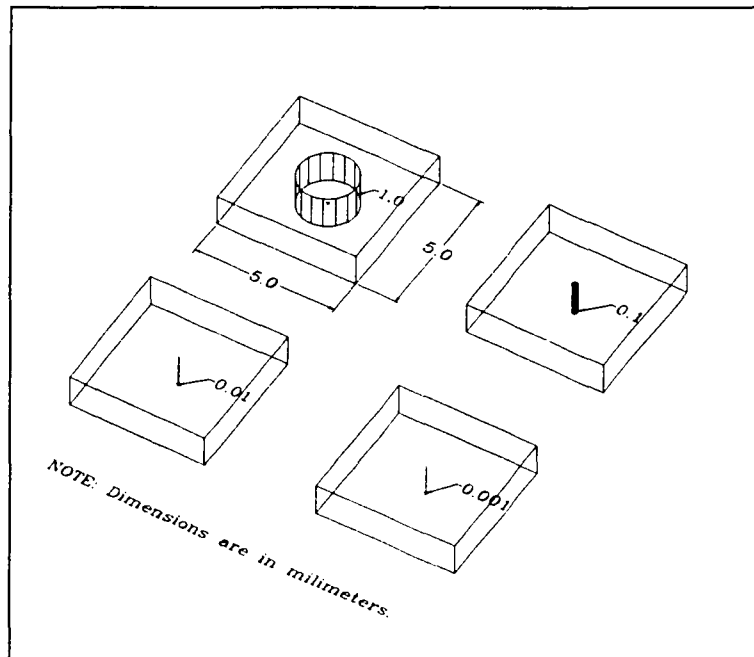


Figure 5.3. 3-D Representation of dust particles to be used in AutoCAD.

5.4.3. Model Results

Table 5.1 shows a typical output of the AutoCAD SOLMASSP command, it can be seen that the volume is reported with a precision of 2 digits. Table 5.2 compares the actual and the calculated area of circles using this technique. For the 5 by 5 mm sample, the smallest particle that could be accurately represented was one with a radius of 1.0 mm.

Table 5.2. Evaluation of the procedure to calculate the area of a circle using AutoCAD.

Particle Radius [mm]	Sample-Circle Area, Calculated [mm ²]	Circle Area, Calculated [mm ²]	Circle Area, Exact [mm ²]	Error %
1.0	21.86	3.14	3.1416	0.05093
0.1	24.96	4.0x10 ⁻²	3.1416x10 ⁻²	27.3236
0.01	24.99	1.0x10 ⁻²	3.1416x10 ⁻⁴	-3083.09
0.001	24.99	1.0x10 ⁻²	3.1416x10 ⁻⁶	-3.182x10 ⁵

This new technique provided better resolution than the Pascal program, and the procedure modeled a sample area of 25 mm² with particles with radius larger than 1.0 mm. This resolution was not sufficient, and the method had two additional disadvantages: AutoCAD does not allow the control of the number of digits printed in the results, and a 486-33 MHz machine would take about 50 minutes to generate one sample of radiant barrier covered by 200,000 particles and to find the area of dust in the dusty sample. Thus even though this procedure looked promising, it was abandoned.

5.5. Fortran Solution

The original idea of projecting the particles onto a screen and counting the pixels to find the ratio of area covered by dust was revisited but instead of the graphical screen, it was decided to attempt to develop a model that would use computer memory to simulate the clean barrier as an integer array originally set to zero. The dust particles were simulated as sets of ones in the array located according to the geometric position of the dust on the radiant barrier.

A computer program in Turbo Pascal was developed, but the resolution was worse than that obtained by the graphical solution. The program was then translated to Microsoft Fortran which had a larger capacity for storing arrays than Turbo Pascal, but the capacity of 64 KBytes per array did not provide a resolution much better than the original graphical solution.

The next logical step was to migrate from the PC to the VAX mainframe. The use of all the available memory into one huge array provided a resolution in which a sample of about 0.25 mm² could be represented with particles for the full range of interest. This resolution was the best obtained so far but still was not considered acceptable.

Realizing that the proposed algorithm wasted memory because each number occupied 32 bits (4Bytes × 8Bits / Byte) and only one bit was used to represent dust, the program was modified to use each bit in each number as the representation of the barrier. The new procedure was somewhat more complicated but finally provided the resolution required to model the dust accumulation on top of the horizontal radiant

barrier. The model could represent a sample area of 9.0 mm^2 for the full range of dust particles of interest. The problem now was that the program took more than 3000 seconds of CPU time to run one simulation. To solve the computing time limitation, the code was transferred to the Cray Y-MP Super Computer. After optimizing the code, the calculation time was reduced to about 34 seconds.

5.5.1. Program Description

Figure 5.4 shows a general flow chart of the program. The code had four main parts: the first part was the initializing procedure; the second part drew the circles in the array; the third part counted the ones to calculate the ratio of area covered by dust and then calculated the resulting absorptivity of the dusty radiant barrier; the last portion of the program printed the results.

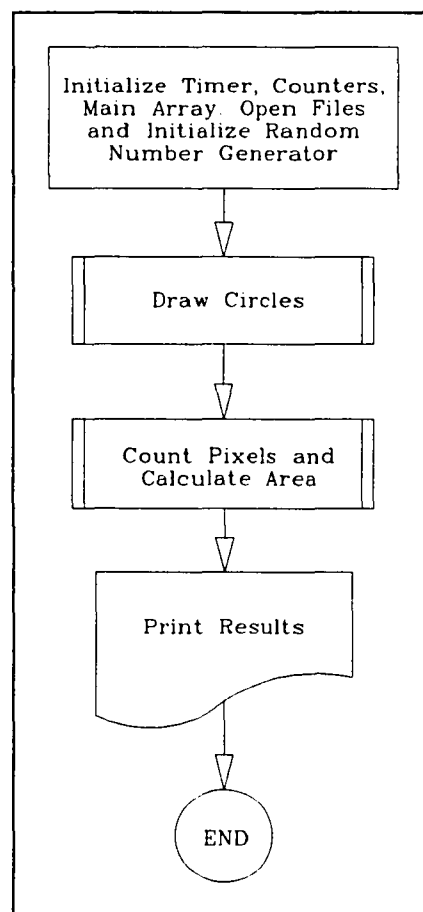


Figure 5.4. General flow chart of the program Dust.

5.5.2. Initialization Procedure

In the initial part of the code the timer, the counters, and the array to simulate the barrier were set to zero. In this portion of the program the data and output files were also opened and the random number generator was set with an integer constant so that the program generated the same series of random numbers every time. This feature was especially important while debugging the code.

5.5.3. Drawing of the Dust Particles in the Memory Array

The program had some restrictions. First, it assumed that the sample was a square of length L and it had the same number of pixels in the x and y directions. It could be made more general, but this feature did not influence the outcome of the results and made the program easier to handle and understand.

The integers in the Cray Y-MP Super computer were 64 bits long which is equal to 1 word of memory. The machine at Texas A&M had 10 mega words (10,240,000 words) of memory available. Discounting the memory required for the program and all the other variables on it, the largest array that was possible could contain only 9,241,600 words. Given this limitation, the memory was structured in an array with MaxY number of rows and MaxX number of columns, according with the following relationships.

$$\text{MaxX} = \frac{\text{MaxY}}{64} \quad (5.2)$$

and

$$\text{MaxX} \cdot \text{MaxY} = 9,241,600 \quad (5.3)$$

Then,

$$\text{MaxY} = 24,320 \quad (5.4)$$

$$\text{MaxX} = \frac{24,320}{64} = 380 \quad (5.5)$$

Note that the array then contained $24,320 \times 24,320 = 591,462,400$ pixels, about 1,900 times the resolution of the VGA screen.

Figure 5.5 shows a more detailed flow chart for this portion of the code. The program started with a "do loop" to control the total number of particles in a certain simulation. Because the most intensive portion of the code was the placement of the particles, all the required dust loadings were simulated in one run of the program. The amount of dust (in number of particles) to be simulated was controlled by the variable H(NBlks) which was read from the data file. This methodology allowed great flexibility in the calculation while maintaining an excellent efficiency of the code.

Inside the loop that controlled the number of particles, the program defined the location and radius of the particle by generating two random numbers. Given that the numbers generated were real between zero and one, the x and y locations of the center of the particle in pixels were found according to the following relations.

$$Cx = R_{cx} \cdot \text{MaxY} \quad (5.6)$$

$$Cy = R_{cy} \cdot \text{MaxY} \quad (5.7)$$

Where R_{cx} and R_{cy} were random numbers generated to define the position of the center of the particle in the x and y direction respectively.

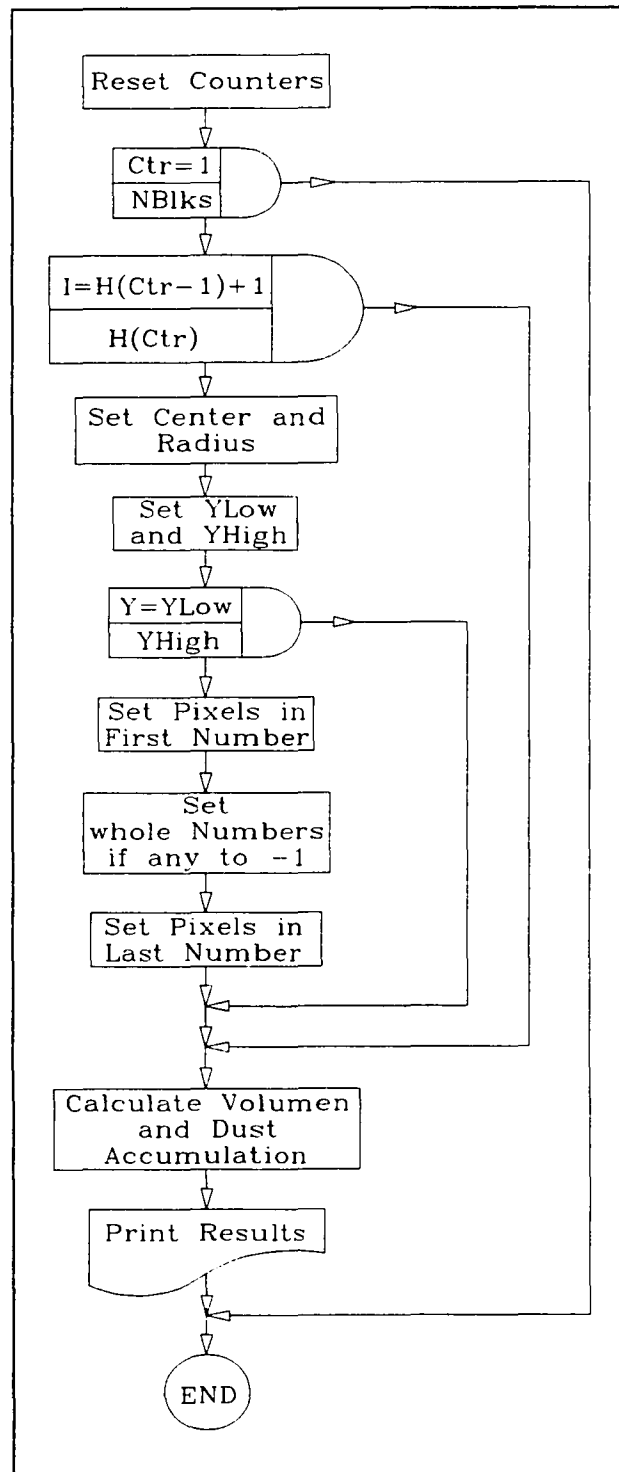


Figure 5.5. Flowchart of subroutine DrawCircle.

The determination of the radius was somewhat more complicated given that the program had to assign the radius according to a particle size distribution. The radius was defined in a "do loop" that compared successively the value of a third random number with the cumulative probability that a particle had to belong to a certain particle size range. If the random number was greater than the cumulative probability of the range $j-1$ and less than the cumulative probability of the range j , then the radius was chosen as the mean radius for that range. For example, for the dust particle analysis shown in Table 4.3, if the random number just generated was equal to 0.9990000, the particle radius was set to 6.75 μm . Once the radius was found, the radius in pixels was found by:

$$\text{RadPix} = \frac{\text{Rad} \cdot \text{MaxY}}{L} \quad (5.8)$$

Where Rad was the radius of the particle, MaxY was the number of pixels in the Y direction and L was the length of the sample in the y direction. Next, the program calculated the starting row where pixels were to be set to one:

$$\text{YLow} = \text{Cy} - \text{RadPix} + 1 \quad (5.9)$$

$$\text{YHigh} = \text{Cy} + \text{RadPix} \quad (5.10)$$

If the starting or ending addresses were out of the array, then the border of the array was set as the boundary of the particle. Then a do loop started to place ones in the array for the rows just defined. In this loop the starting and ending location in the x direction were found solving the quadratic equation that defines the circle:

$$x_{\text{start, end}} = \frac{-b \pm \sqrt{b^2 - 4c}}{2} \quad (5.11)$$

where,

$$b = -2 \cdot \text{Cx} \quad (5.12)$$

$$c = (y - \text{Cy})^2 + \text{Cx}^2 - \text{RadPix}^2 \quad (5.13)$$

Because the program approximated the circle with a set of squares, the last operation had to determine if the square on the border of the circle was covered more than half by the circle. To accomplish this, the program calculated the y coordinate of the circle at the middle of the square (y in Figure 5.6) and compared it with the coordinate of the center of the pixel (y_c in Figure 5.6), setting the starting and ending locations accordingly.

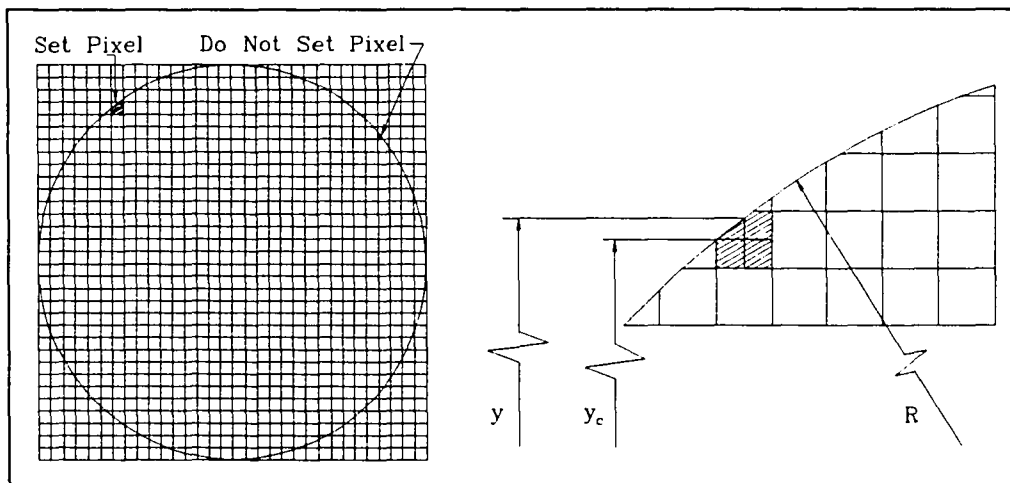


Figure 5.6. Setting of pixels on the border of the circle.

Once the starting and ending locations in the x direction were set, the program proceeded to set the pixels to one, but this operation was performed bit by bit. A pointer to locate the first integer to be modified was found by:

$$\text{ptr} = \frac{\text{XLow} - 1}{64} + 1 \quad (5.14)$$

and a pointer to track the location of the pixel that was being set was also defined as:

$$\text{ptrBit} = (\text{ptr} - 1) \cdot 64 \quad (5.15)$$

Then, the starting bit in the first number was found as:

$$\text{MinBit} = 64 - (\text{XHigh} - \text{PtrBit}) \quad (5.16)$$

Noting that this number can be negative, it was added to the absolute value of itself and the result was divided by two which resulted in zero if the original number

was negative. MinBit also could not be 64, if this was the case, all the bits were to be set to one. For this purpose MinBit was again modified by:

$$\text{MinBit} = \left(1 - \frac{\text{MinBit}}{64}\right) \cdot \text{MinBit} \quad (5.17)$$

Which resulted in the same MinBit, if it was different than 64, otherwise it resulted in zero. MaxBit was found in a similar fashion:

$$\text{MaxBit} = 64 - (\text{Xlow} - \text{PtrBit}) \quad (5.18)$$

and it was controlled so that it did not take the value 64 as well. With MinBit and MaxBit defined, a do loop was performed to set the bits to zero inside the first number, the intrinsic function IBSET was used. The next step was to set to -1 (binary 111..111) the numbers that contained all ones. This was accomplished by a do loop between Ptr+1 and XHigh / 64 that set the array to -1. Finally, the last number that contained ones was found, and the procedure described to set the first number that contains ones was repeated.

At this point the "do loop" that accounted for the number of particles was closed. When this loop was done, the program called the subroutine that counted the ones in the array and calculated the ratio of area covered by dust to the area of the sample. To relate the ratio of areas to the absorptivity of the dusty radiant barrier, as explained in section 3, the following relationship was used:

$$\alpha_{db} = \alpha_b + (\alpha_d - \alpha_b) \cdot f_p \quad (5.19)$$

Where f_p was the fraction of the foil area covered by dust particles to the total area of the sample, α referred to absorptivity and the subscripts d, b and db referred to dust, barrier and dusty barrier respectively.

The volume of dust was found by multiplying the number of particles of each size times the volume of each sphere. The loading was found by multiplying the dust volume times the dust density and dividing the mass of dust by the area of the sample.

The program repeated the calculations for several dust loadings and printed the results onto the screen and into a file. At the end, it stopped the timer and printed the CPU and wall clock times used by the computer.

5.5.4. Finding the Area Covered by Dust

This subroutine was smaller and simpler. It only set up a triple loop to sweep the array in the x and y direction and inside each number. It is interesting to note that the largest loop corresponding to the y direction had to be the inner loop for the Super Computer to perform optimally regardless of what made more sense to the human mind.

The ratio of area covered by dust to the total sample area was found by,

$$\text{Area} = \frac{\text{CountPix}}{\text{MaxY} \cdot \text{MaxY}} \quad (5.20)$$

In this equation, L^2 has been dropped from both the numerator and denominator of the expression.

5.6. Summary

After several failed attempts to model dust accumulation on top of horizontal radiant barriers, a model was developed in which the computer memory was used to simulate the clean barrier, and the dust particles were simulated as an orderly array of bits set to one in the original set of zeroes. The program changed the zeroes to ones but not backwards. Once a one was set, it remained as such until the end of the simulation. This methodology provided the means to account for dust superposition and overlapping in a natural way.

Once all the particles were represented, the program counted the number of ones in the array. The area of barrier covered by dust was then calculated as the ratio of the total number of ones to the total number of pixels in the array.

Finally, the resulting absorptivity of the dusty barrier was calculated as the linear relationship between the area ratio of dust coverage, the absorptivity of the clean barrier and the absorptivity of the dust, as explained in section 3.

6. EXPERIMENTAL ANALYSIS

6.1. Introduction

In addition to the experimentation described in section 3, an extensive experimental analysis was carried out to assess the model validity. Radiant barrier samples were placed in attics in the Bryan-College Station, TX area for collecting natural dust. Samples made with Arizona Road Test Dust were used for controlled tests of dust accumulation on top of the HRB's.

When one refers to a HRB, the appropriate name of the property that makes the barrier absorb the incoming radiation is its absorptivity. If the incoming radiation is diffuse and the surface is gray, then according to Kirchhoff's law, the emissivity of the surface should be equal to its absorptivity. In this section, the absorptivity is labeled as the emissivity, because the instrument used to perform the measurements of this property was an emissometer. Thus, this instrument measured the emissivity of the sample. The reader should be aware that the numerical value of the measured property emissivity was assumed to be equal to the numerical value of the property absorptivity.

Once the samples were prepared, the emissivity of the dusty barriers was measured using an infrared reflection emissometer, the samples were also weighed with and without the dust on the sample to measure the dust loading. A small piece of the dusty sample was examined using an electron microscope. The photomicrographs obtained in the microscope were analyzed using digital techniques to find the dust particle size distribution and the area of dust coverage.

Thirty six samples of natural dust were collected, and thirty samples using Arizona Test Dust were prepared. The microscope analysis produced 285 photomicrographs.

6.2. Instrumentation

To carry out the experimentation, the following equipment was used:

1. Analytical scale Scientech Model ESA-80 with the following specifications:
 - Single weighing mode.
 - Capacity: 80 g.
 - Readability: 1.0×10^{-4} g.
 - Tare range: 0-80 g.
 - Repeatability (Standard Deviation): 1.0×10^{-4} g.
 - Linearity: $\pm 2.0 \times 10^{-4}$ g.
 - Stabilization time: ~ 3 s.
 - Data interface: RS232C bi-directional. Baud Rates: 300, 600, 1200, 2400, 4800, 9600 and 19200.
 - Power supply: 115 V / 60 Hz.

2. Emissometer: Devices and Services Model AE with the following specifications:
 - Spectral Response: The radiation detector was a differential thermopile with low and high emissivity areas. The combination insured a near constant response to thermal wavelengths from 3 to 30 microns.
 - Linearity: ± 0.01 emissivity units.
 - Output: Nominally 2.4 millivolts measuring a sample with $\epsilon = 0.93$ at room temperature.
 - Heat Sink: Used to keep both the calibration standard and the unknown sample at the same temperature.
 - Drift: The output changed with time due to changes in ambient conditions. This effect was negligible over the time required to make one measurement. Frequent re-calibrations were required for multiple measurements.
 - Calibration Standards: Two, each of $\epsilon = 0.87$ and $\epsilon = 0.08$ were provided by the manufacturer.
 - Power: 80 to 160 AC V, 4 w.

3. Multimeter: Fluke Model 45 Dual Display with the following specifications for the DC voltage in the working operating range:
 - Range: 0-300 mV.

- Resolution: 100 μv .
 - Accuracy: $\pm 0.025\% + 2$.
 - Input Impedance: 10 M Ω in parallel with < 100 pF.
4. Laptop computer. To act as data logger of the multimeter for the emissivity measurements. Using the RS-232C serial port data was transmitted to the computer. A Basic program was written to perform the communication between the two devices.
 5. Coating device: Technics model Hummer I. This device provided a gold coating of approximately 200 nm to the samples to be analyzed in the electron microscope.
 - Operating pressure: 120 mTorr.
 - Operating Voltage: 11 DC V.
 - Operating current: 10 mA.
 6. Electron Microscope. Jeol Model JSM-T330A. With the following operating parameters:
 - Gun accelerating voltages selectable from 1.6 to 30 kV. The instrument was operated at 15 kV for all the experimentation.
 - Gun Bias: 0-1 mA. The instrument was used with 0.35 mA of Bias current for all the experiments.
 - Magnification selectable from 35 X to 200,000 X.
 - Nominal operating pressure: 8.0×10^{-6} Torr.
 - Secondary Electron Detector: Scintillator-photomultiplier system.
 7. Film processor equipment. Mohor Enterprises model Mohorpro 8. Automatic film processor to produce the negatives from the photomicrographs taken in the electron microscope.
 8. Scanner. Epson attached to a Macintosh II machine, running the program Scan Do/DA Ver. 1.7 to produce TIFF files from the negatives.

9. Video Camera Dage-MTI, Inc. Series 68. Connected to a Macintosh II fx computer running the program Truevision-Capture, Ver. 2.2 to produce TIFF files.
10. Macintosh II fx computer. Running Image Ver. 1.39b6 to make the particle size analysis of the TIFF files.
11. Radiant barrier without perforations. The radiant barrier was aluminum foil with a measured emissivity $\epsilon_p = 0.03$.
12. Arizona Test Dust: from AC General Motors Air Cleaner Test Dust Fine and Coarse, with measured emissivity $\epsilon_d = 0.82$ and the particle size analysis shown and studied in section 4. The measured density was 2.7 g / cm^3 .

6.3. Natural Dust Collection

To collect natural dust, radiant barrier samples 7.6 cm by 7.6 cm (Figure 1) were placed inside plastic containers. Fifteen of those containers were placed inside each attic of four selected buildings in the Bryan-College Station area which was located in Central Texas. The samples were left undisturbed for a period of time and then collections were scheduled and made (Table 6.1). Every sample was labeled and numbered to record the time of dust accumulation and location of the sample inside the attic. At the time of collection, the lid of the container was replaced and the container was treated with care, trying not to disturb the dust accumulated on the barrier sample.

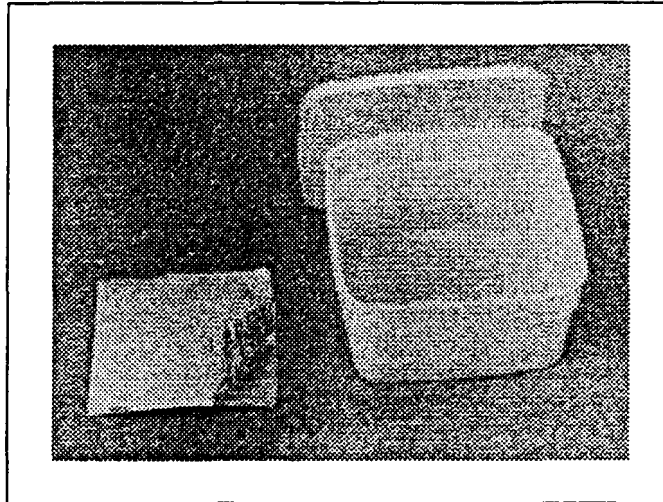


Figure 6.1. Photograph of a radiant barrier sample.

Table 6.1. Schedule of radiant barrier samples installation and collection.

Installation (Date)	Collection (Date)	Elapsed Time (Days)
08/01/86	10/20/92	2272
08/01/86	01/14/92	1992
08/01/86	03/07/91	1699
05/22/91	02/04/93	624
03/27/91	10/20/92	573
03/20/91	08/31/92	530
04/20/91	03/14/92	329
03/27/91	01/14/92	293
03/20/91	07/23/91	125
04/20/91	08/22/91	124
03/27/91	07/28/91	123

6.4. Experimentation Using Arizona Test Dust

To be able to simulate any dust loading, Arizona Test Dust was sprinkled using a dust nebulizer developed in the Aerosol Technologies Laboratory at Texas A&M University. This nebulizer used a current of air driving the dust particles through a nozzle to achieve the particles separation and to obtain a very smooth and

uniform distribution of dust on the samples. As Levins et al. (1990) noticed, artificially applied dust did not adhere to the radiant barrier as well as natural dust. Natural pollutants, such as pollen and hydrocarbons could be responsible for the better adherence of the natural dust.

6.5. Weight Measurements

Once the sample was obtained (from an attic collecting natural dust or made using the Arizona Road Test Dust), a small piece (about 1 cm²) was cut for later use in the electron microscope analysis. The remainder of the sample was weighed using the electronic scale described earlier. To avoid excessive manipulation of the samples, only one measurement was made with the dusty barrier. After the emissivity measurement was performed, the sample was carefully cleaned and weighed again. Three readings were performed to provide statistical data from the measurements.

6.6. Emissivity Measurements

After the dusty sample was weighed for the first time, the emissivity of the dusty radiant barrier was measured using the reflection emissometer described earlier. The procedure was rather tedious because it was necessary to calibrate the instrument before performing the measurements and it was necessary to re-calibrate the device frequently during the procedure. The calibration procedure was done using two calibration standards supplied by the instrument manufacturer. The power was turned on for at least 30 minutes to allow it to warm up. The emissometer was then placed over the high emissivity sample (emissivity $\epsilon_h = 0.87$). After 150 seconds, the computer recorded the voltage V_h generated by the emissometer. The emissometer was then placed over the low emissivity sample (emissivity $\epsilon_l = 0.08$). The expected voltage corresponding to the low emissivity sample was calculated according to the following formula: (Devices & Services, 1981).

$$V_{l,ex} = \frac{V_h \cdot 0.08}{0.87} \quad (6.1)$$

Equation (6.1) shows the linearity relation exhibited by the device in measuring the emissivities.

After another 150 seconds, the computer recorded the voltage V_l corresponding to the low emissivity sample. This voltage was compared with the expected low voltage $V_{l,ex}$, and the instrument was calibrated appropriately. This procedure was repeated until the expected low voltage was equal to the measured low voltage. When the calibration was completed, it was possible to perform the emissivity measurements. The emissometer was placed on top of the low emissivity calibration sample and after 150 seconds, the voltage V_l was recorded. The emissometer was then placed on top of the sample to be studied and after the same time period of 150 seconds, the voltage V_s was measured. The emissivity of the sample ϵ_s was calculated using the following relation (Devices & Services, 1981):

$$\epsilon_s = \frac{V_s \cdot 0.08}{V_l} \quad (6.2)$$

Figure 6.2 shows the equipment used for the emissivity measurements.

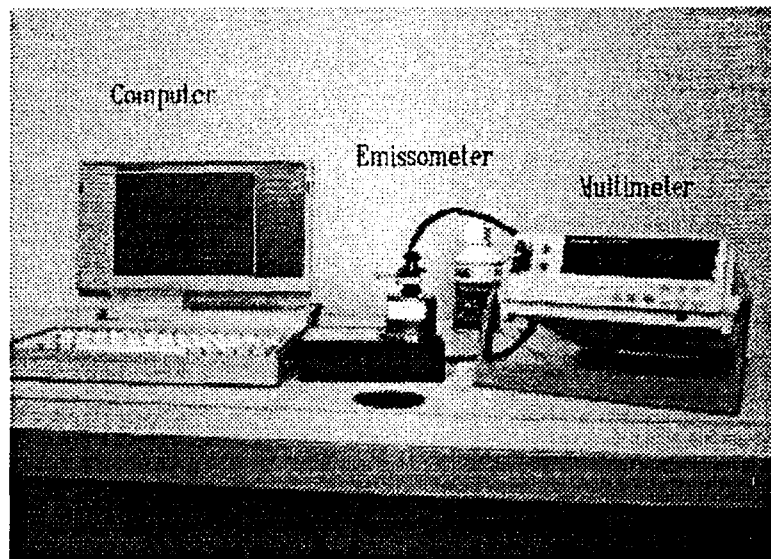


Figure 6.2. Equipment used to measure the emissivity of the radiant barriers. From left to right: computer, emissometer, and multimeter.

6.7. Electron Microscope Analysis

To better understand how the experimentation was carried out, a brief explanation of the principle of operation of the electron microscope follows.

6.7.1. Electron Microscope Basic Operating Principle

The scanning electron microscope is a powerful instrument which permits the observation and characterization of heterogeneous organic and inorganic materials and surfaces on a local scale. In the instrument, the area to be examined, or the micro volume to be analyzed, is irradiated with a finely focused electron beam, which, in the case of the instrument used for this research, swept in a raster pattern across the surface of the specimen. The signals produced when the electron beam impinges on a specimen surface include secondary electrons, backscattered electrons, Auger electrons, characteristic x-rays, and photons of various energies (Goldstein, et al., 1981). These signals were obtained from specific emission volumes within the sample and could be used to examine many characteristics of the sample (composition, surface topography, crystallography, etc.).

In the scanning electron microscope, the signals of greatest interest were secondary and backscattered electrons, because these signals varied as a result of differences in surface topography as the electron beam was swept across the specimen. The secondary electron emission was confined to a volume near the beam impact area, permitting images to be obtained at relatively high resolution (usually 5 nm in commercially available instruments). The three dimensional appearance of the images was due to the large depth of field of the scanning electron microscope as well as to the shadow effect of the secondary electron contrast (Goldstein, et al., 1981).

The basic components of the SEM were the electron gun, lens system, electron collector, visual and recording cathode ray tubes (CRTs), and the electronics associated with them. Figure 6.3 shows a schematic diagram of a combined scanning electron microscope.

The electron gun provided a stable source of electrons which was used to form the electron beam. These electrons were obtained from the source by a process called thermionic emission. In this process, at sufficiently high temperatures, a certain percentage of electrons became sufficiently energetic to overcome the work function energy that held them in place and escaped the source. The filament was heated and maintained at a high negative voltage (1-50 kV) during operation.

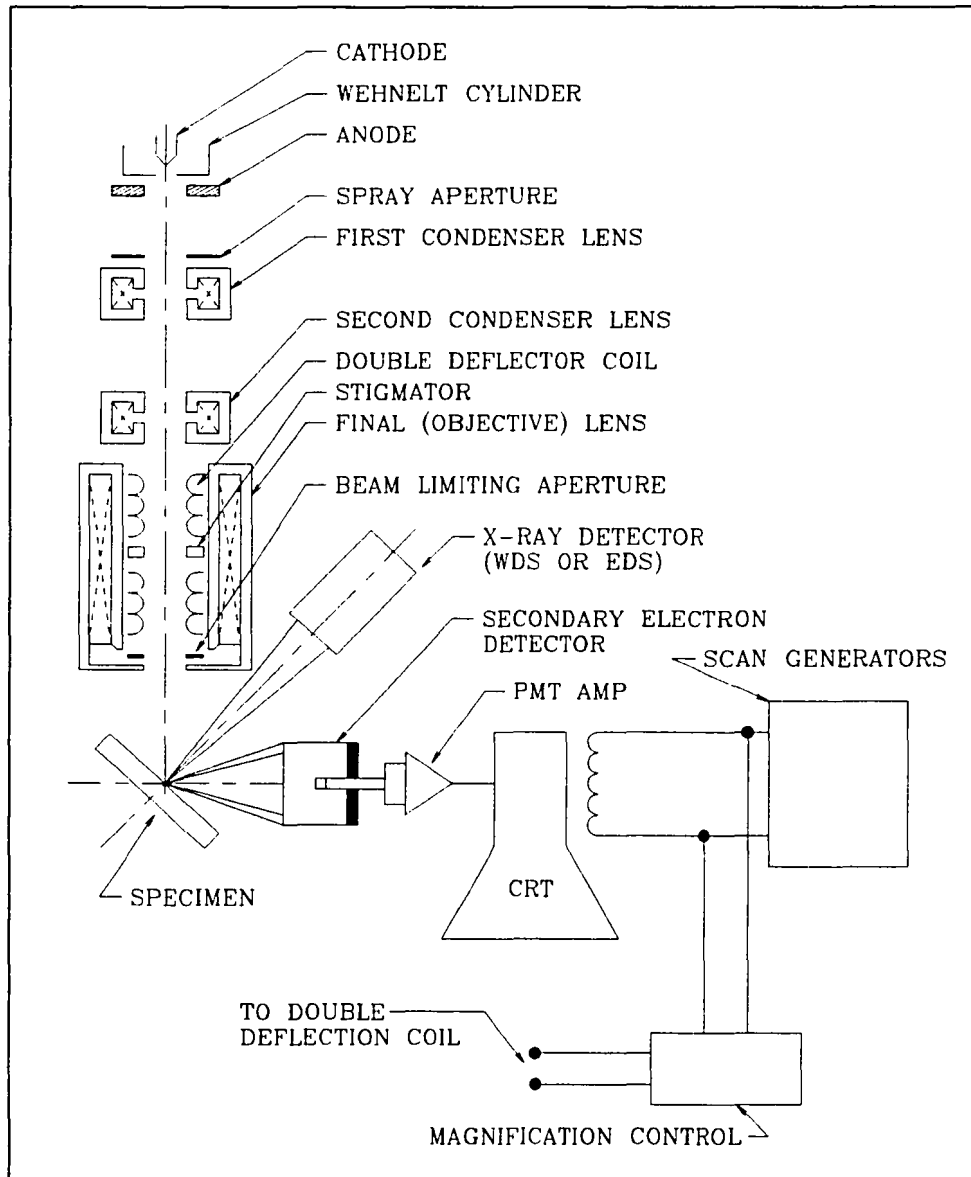


Figure 6.3. Schematic drawing of the electron and x-ray optics of a SEM.

Surrounding the filament was a grid cap or Wehnelt cylinder with a circular aperture centered with the filament tip. The grid cap was biased negatively between 0 and 2.5 kV with respect to the cathode. The effect of the electric field formed in such a gun configuration caused the emitted electrons from the filament to converge to a crossover. Two electron lenses were used to de-magnify the electron image to the

final spot size on the sample (5-200 nm). The condenser lenses system, which was composed of two lenses, determined the beam current which impinged on the sample. The final probe-forming lens, often called objective lens, determined the final spot size of the electron beam.

Once the electron beam impinged the specimen, two classes of interactions occurred: (1) elastic events, which affected the trajectories of the beam of electrons within the specimen without significantly altering the energy, and (2) inelastic events, which resulted in a transfer of energy to the solid, leading to the generation of secondary electrons, Auger electrons, characteristic and continuum x-rays, long-wavelength electromagnetic radiation in the visible, ultraviolet and infrared regions, electron-hole pairs, lattice vibrations (photons), and electron oscillations (plasmons). In theory, all these interactions could be used to obtain information about the nature of the specimen: shape, composition, crystal structure, electronic structure, internal electric or magnetic fields, etc. In practice, the most used interactions were the secondary electrons, the backscattered electrons, and the characteristic and continuum x-rays.

Secondary electrons were defined as those electrons emitted from the sample with an energy less than 50 eV (an arbitrary cutoff). The electron sensor was called scintillator-photomultiplier system. The sensor contained a doped plastic or glass target, or a compound such as CaF_2 doped with europium. The electrons striking the sensor produced photons which were conducted by a light pipe to a photomultiplier which was permanently isolated from the vacuum of the SEM. The photons struck the first electrode of the photomultiplier causing it to emit electrons, which then cascaded through the remaining electrode stages eventually producing an output pulse of electrons with a gain of 10^5 - 10^6 . This gain was obtained with very little noise degradation and a wide frequency bandwidth. To make use of the low-energy secondary electron signal, the scintillator was covered with a thin (10-50 nm) layer of aluminum and biased to approximately +10 kV, which served to accelerate the low-energy electrons. To prevent the 10 kV bias from displacing the incident beam or introducing astigmatism, the biased scintillator was surrounded by a Faraday cage near ground potential. The Faraday cage had a mesh opening to permit the entrance of electrons. To improve the collection of secondary electrons, a positive potential of

as much as +300 V could be placed on the cage. This voltage did not cause significant degradation of the incident beam (Goldstein, et al. 1981).

In forming the area scanning image, the beam was scanned on the specimen in an X-Y grid pattern while the CRT was scanned in the same X-Y pattern. A one to one correspondence was established between the set of beam locations on the specimen and the points on the CRT. To display the electron interaction information, the signal intensity derived from the detector was used to adjust the brightness of the spot on the CRT, called intensity or Z modulation. Thus, the creation of an SEM image consisted of constructing a map of the CRT. Unlike an optical or transmission electron microscope, no true image actually existed in the SEM but rather a mapping operation which transformed information from specimen space to CRT space.

6.7.2. Experimental Procedure Using the SEM

The small pieces of dusty radiant barrier were attached on mountings made for the holdings on the electron microscope. The mountings containing the radiant barrier were then placed on the coater, a device that used a vacuum and high voltage to produce plasma and flow of gold atoms from the anode to the cathode of the device. Because the analysis samples were mounted on the cathode, gold was deposited in atomic layers over the surface of the sample. This treatment was necessary to assure that the electron flow in the electron microscope could be dissipated and no static charge could develop on the sample. If this treatment was not performed or if it was performed incorrectly, the static charge built up in the dust particles would blow them off the barrier and destroy the experiment.

Once the sample was properly prepared, the electron microscope analysis was done according to the following procedure: (1) the sample was located inside the vacuum chamber of the electron microscope, and the vacuum pump was turned on; (2) once the pressure was reduced to 8×10^{-6} Torr, the electron gun was energized with an accelerating voltage of 15 kV, and the bias current was set to 0.35 mA; (3) once the image was formed, the magnification was set to 35 X, and a preliminary focus was performed; (4) after an appropriate zone of the sample was chosen, the microscope was set to a magnification equal to 10,000 X and the microscope was focused correctly; and (5) the photographs were taken. To ensure the strongest

contrast in the view, a large spot size (≥ 10 nm) was chosen, and the instrument was set with the desired magnification (200 X, 500 X, 1,000 X or 3,500 X). In the electron microscope, once focus was obtained at a large magnification, the view remained in focus at any lower magnification. Thus, no further tuning was required.

6.7.3. Electron Microscope Image Processing

After all the pictures of one session of the electron microscopy analysis were taken, the negatives were developed and later digitized. Either a video camera and the corresponding Truevision-Capture software, or a scanner and the corresponding program Scan Do/DA were used on a Macintosh computer. The digitized images were then imported to the Image software and the following procedure was followed to obtain the fraction of area covered by particles: (1) a threshold brightness was set to convert the gray image into an all white and black image; (2) the image was then converted to binary format; (3) using the scale printed in the picture, a scale for the computer was constructed, converting the pixels read in the image to μm ; (4) the image was then cleaned, erasing all the text and the scale line, creating a clean frame in the image; and (5) the area of analysis was set and the particle analysis was performed. The program generated a file containing the numeric values of the area of each particle in the image and the area of the frame just scanned. The Macintosh files were converted to IBM format to make the statistical analysis in the computer system available for this research. Figure 6.4 shows a typical image obtained using the procedure described.

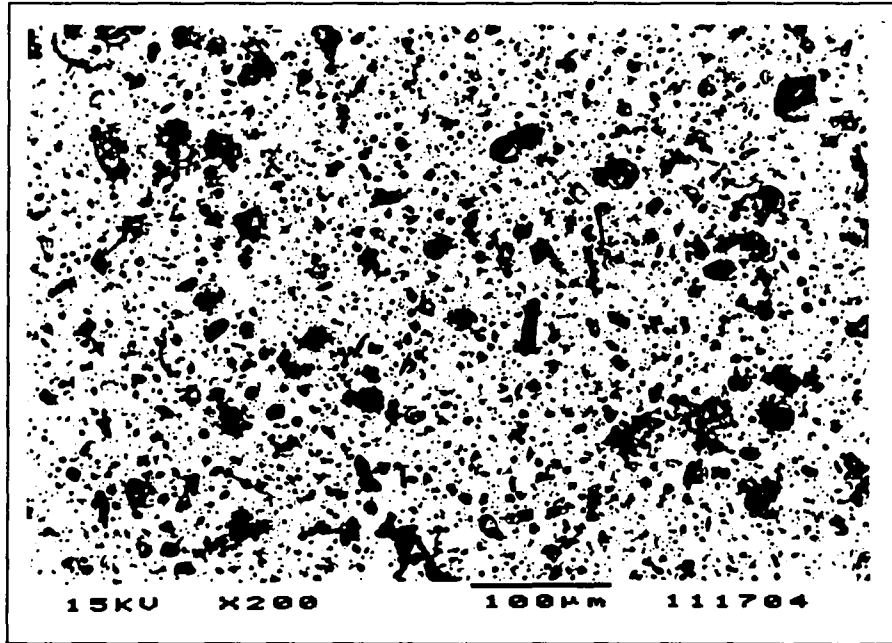


Figure 6.4. Typical image obtained after digitizing the SEM pictures.

Using the areas of the dust particles and the area of the frame where the particles were digitized, the fraction of the foil area covered by particles was found from:

$$f_p = \frac{\sum \text{Areas of Particles}}{\text{Frame Area}} \quad (6.3)$$

The statistical analysis included the determination of the total area of dust coverage, the determination of the mean and standard deviation of the population of particles, and the particle size distribution of the sample.

6.8. Determination of the Radiant Barrier Sample Area

To calculate the dust loading on the (approximately) 7.5 cm x 7.5 cm samples, the following formula was applied:

$$w_d = \frac{(W_{ds} - W_{cs})}{A_s} \quad (6.4)$$

where

- w_d = Dust loading [mg / cm²]
- W_{ds} = Weight dusty sample
- W_{cs} = Weight clean sample
- A_s = Area of the sample

The weight measurements were obtained as explained in section 6.5. To determine the area of the radiant barrier sample, after the emissivity and weight measurements were performed, the sample was cleaned and painted black. The black sample was then scanned to form a digital image of it. The digital image (together with a scale) followed the same procedure used to produce the electron microscope images. The image was converted to gray tones, a threshold brightness was set to transform the gray image into an all black and white image and then transformed to binary format. Finally, the same program used to make the particle analysis was used to find the area of the barrier sample, but in this case, the only particle to be analyzed was the sample area itself.

6.9. Statistical Analysis of the Measurements

A statistical analysis was performed on the experimental results. The measurements of weight and emissivity were the average of three consecutive readings, whereas the fractional covered by dust particles was determined by a single measurement.

The statistical analysis of the multiple measurements included the calculation of the mean and the standard deviation according to the relations:

$$\bar{x} = \frac{\sum_{i=1}^n x_i}{n} \quad (6.5)$$

$$s = \left[\sum_{i=1}^n \frac{(x_i - \bar{x})^2}{(n-1)} \right]^{1/2} \quad (6.6)$$

6.9.1. Weighing Measurements

Every reported measurement was the average of three consecutive readings. The mean and standard deviation of these three readings were calculated. To better understand the variation of the measurements, the mean of the standard deviations was computed using the same Equation (6.5). With the scale having a resolution of 1.0×10^{-4} g, the mean standard deviation was 5.3×10^{-5} g. The measurements had an accuracy of 1.0×10^{-4} g corresponding to the resolution of the instrument and no further restrictions apply to the measurements.

6.9.2. Emissivity Measurements

Given that the calibration standards had two digits of accuracy, the emissivity results cannot have any better resolution than the calibration standards. The emissometer provided an analog signal that was measured by the digital multimeter. Even though the multimeter provided 5 digits of accuracy, the result of the calculation given by Equation (6.2) was rounded to two digits.

The emissivity measurements were repeated three times in the samples containing natural dust, but the measurements were done only once in the samples containing Arizona Test Dust. The reason for this difference was that because the natural dust adhered better to the radiant barrier, and the sample remained undisturbed after the measurement. Because of the very low adhesiveness of the Arizona Road Test Dust, the sample was always disturbed after the measurement. Dust was displaced, and the barrier showed patches of clean surface. Any attempt to repeat the measurement would have resulted in a lower value of the emissivity than the initial measurement.

For these measurements, the mean of the standard deviations was also computed using Equation (6.5) and was equal to 0.0071 emissivity units. These results showed that the emissometer performed within the manufacturer's

specifications. Thus, the results were within the resolution of the calibration standards (0.01 units of emissivity).

6.9.3. Fraction of Area Covered by Dust Measurements

Given the complexity and the cost of the measurements, only one reading of the fraction of area covered by dust particles was performed for each sample. The experimental approach followed was to cut a 1 cm x 1 cm area from the approximately 7.5 cm x 7.5 cm sample. Typically a corner piece was cut out to minimize disturbance of the dust particles on the sample. Therefore a small, but representative area, was selected for the SEM study. Once the sample was placed on the mounting probe and prepared for SEM analysis, a representative area was chosen for the single point analysis at 500X magnification. To find the error associated with this experimental approach, a statistical analysis of the procedure was performed.

One 7.5 cm x 7.5 cm sample with natural dust was cut in small pieces to make ten electron microscope probes. Each probe was placed in the SEM, and the fractional area was determined, as explained in sections 6.7.2 and 6.7.3, using a single, representative area on each probe.

Table 6.2 presents the data obtained by the measurements of the fraction of area covered by dust in ten different probes. Table 6.3 presents the statistics corresponding to this experiment.

Table 6.2. Fraction of area covered by particles for ten different probes at 500X magnification.

Photo	Sample	Area
080302	58	0.072569
080305	59	0.106123
080307	60	0.087633
080309	61	0.077388
080311	62	0.093968
080313	63	0.079503
080315	64	0.074497
080317	65	0.083318
080319	66	0.07278
080325	67	0.090072

Table 6.3. Statistics of the fraction of area covered by particles for ten different probes at 500X magnification.

10	Number Measurements
0.8503780	Sum
0.0850378	Average
0.0100840	Standard Deviation
0.0725690	Minimum
0.1061230	Maximum
0.07495 ↔ 0.09512	$\bar{x} \pm s$

The measurements of the fraction of area covered by dust had a mean of 0.085 and a standard deviation of 0.010 corresponding to 11.9 % of the reading, showing that one probe obtained from the sample was a good representation of the sample.

Given that at the chosen magnification (500X) in the 1 cm² probe there were many locations that could be chosen for making the photomicrograph, the statistics with respect to the location of the photomicrograph within the probe were calculated using thirteen photographs at different locations on one probe. The photographs were taken in locations equally spaced across the probe. Table 6.4 shows the data and Table 6.5 shows the statistics obtained in this experiment.

Table 6.4. Fraction of area covered by particles for thirteen different locations on one probe at 500X magnification.

Photo	Sample	Area
081001	66	0.060859
081002	66	0.091592
081003	66	0.103297
081004	66	0.109263
081005	66	0.078453
081006	66	0.101694
081007	66	0.097265
081008	66	0.105366
081009	66	0.081766
081010	66	0.088293
080319	66	0.072780
080321	66	0.073153
080323	66	0.085307

Table 6.5. Statistics of the fraction of area covered by particles for thirteen different locations on one probe at 500X magnification.

13	Number of Measurements
1.1490880	Sum
0.0883914	Average
0.0147140	Standard Deviation
0.0608590	Minimum
0.1092630	Maximum
0.07368 ↔ 0.10311	$\bar{x} \pm s$

The measurements of the fraction of area covered by dust had a mean of 0.088 and a standard deviation of 0.015 corresponding to 16.6 % of the reading.

The average of the measurements of the ten probes (Table 6.3) differed from the average of the thirteen measurements made on one probe (Table 6.5) by less than one standard deviation and also both means were within the $[\bar{x} \pm s]$ range. These

statistics showed that the measurements of the fraction of area covered by dust had an error less than 0.015 (fraction of area covered by particles). The fractional area determined by the single measurement expected to be accurate within $\pm 16\%$. The methodology thus chosen to determine the fractional area covered by dust was a valid approach.

6.10. Analysis of the Experimental Results

To be able to correlate the microscopic information with the emissivity and dust loading information, a data base was created in which the following data was recorded for every sample (in parenthesis is the section where the procedure was explained):

1. Identification numbers of the photomicrographs obtained from the sample.
2. Measured fraction of foil area covered by dust particles (6.7).
3. Statistical data of the particles of the sample (6.7).
4. Weight of the dusty sample (6.5).
5. Weight of the clean sample (6.5).
6. Area of the sample (6.8).
7. Measured dust loading (6.8).
8. Measured emissivity (6.6).
9. Calculated emissivity (Equation (3.35)).

Figures 6.5 and 6.6 show the measured emissivity as a function of the dust loading in mg/cm^2 for the two types of Arizona Road Test Dust used in the research. The smooth curves were exponential curve fits of the experimental data. As noted in Noboa (1991), the resulting emissivity was sensitive to the particle size of the dust. The microscopic analysis showed that fine dust tended to settle in between the particles and larger particles tended to overlap. This is the reason why fine dust produced larger emissivities for any given dust loading.

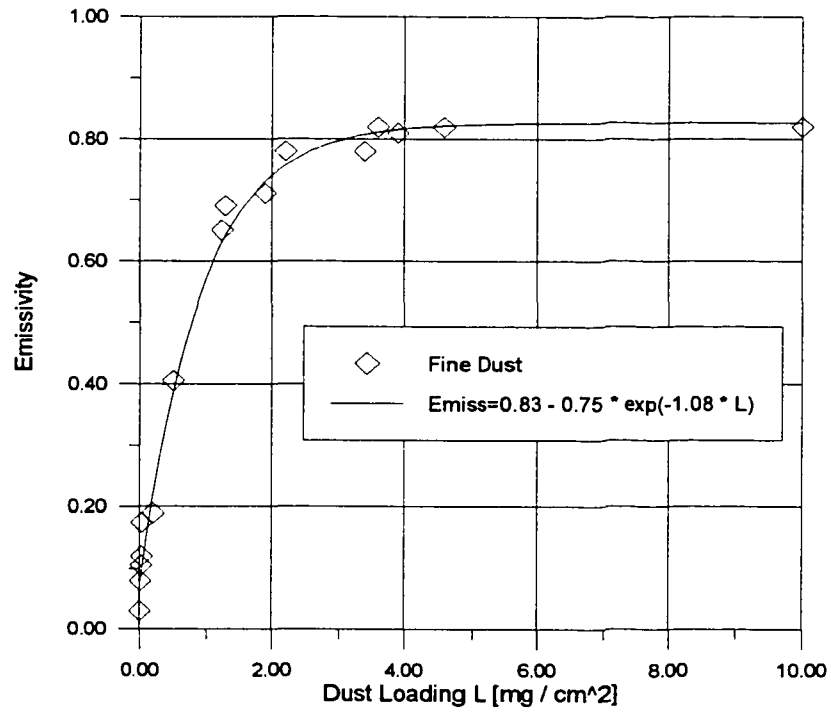


Figure 6.5. Experimental emissivity vs. dust accumulation for fine dust.

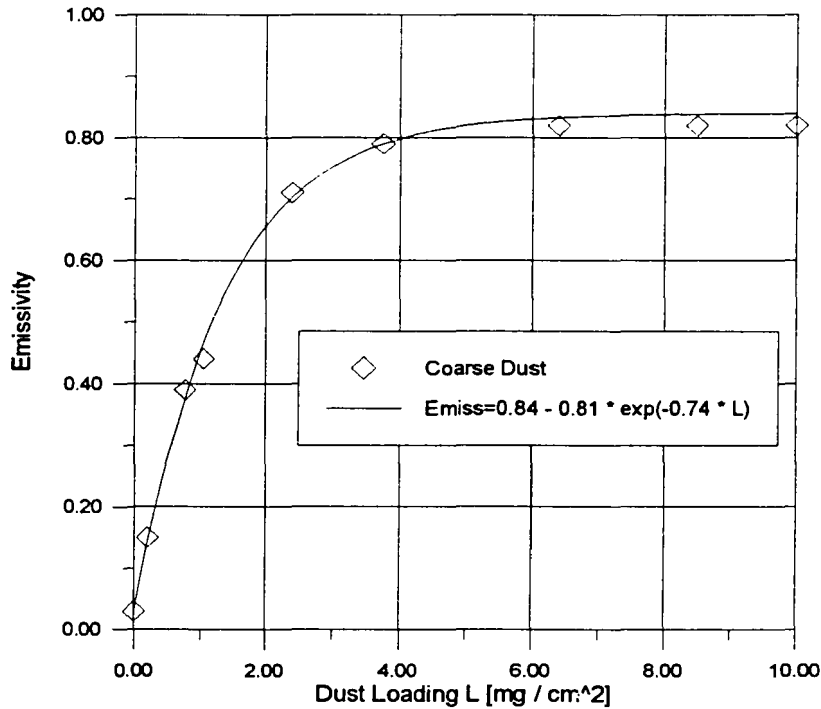


Figure 6.6. Experimental emissivity vs. dust accumulation for coarse dust.

Figure 6.7 shows the measured emissivity as a function of the dust loading in mg / cm^2 for the natural dust collected on the radiant barrier samples placed inside the attics of the houses. A much coarser distribution was found and the dispersion of the results was a result of the differences on the dust physical properties such as emissivity, density, composition, etc. Also, it should be noted that in the five year period in which dust was collected, the maximum dust loading was about $0.75 \text{ mg} / \text{cm}^2$ which corresponded to a light loading of the Arizona Road Test Dust.

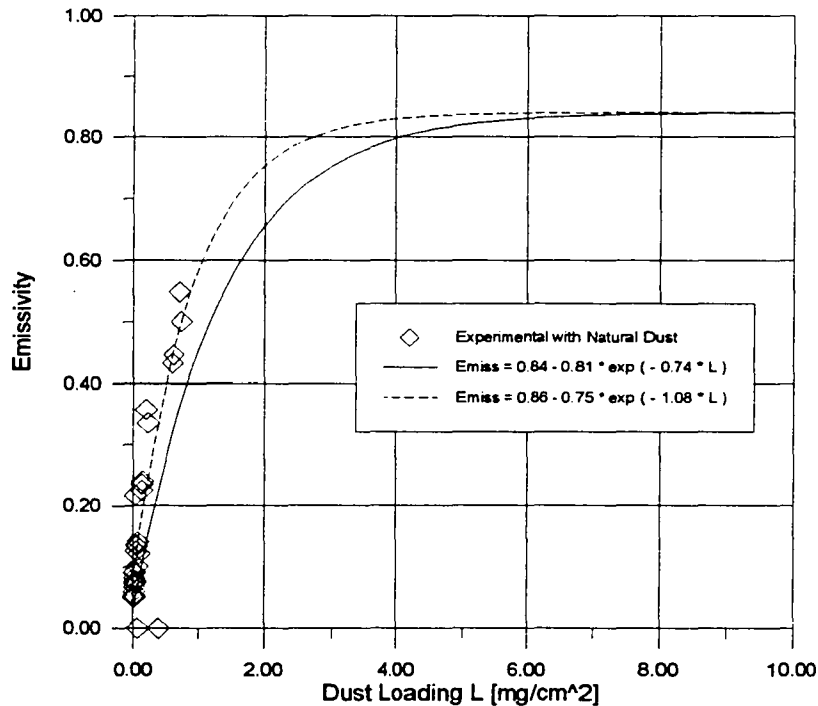


Figure 6.7. Experimental emissivity vs. dust accumulation for natural dust.

For comparison purposes, Figure 6.7 shows the experimental data and the exponential curve fitting developed for the fine and coarse test dust. It can be seen that the fine Arizona Road Test Dust behaved similarly to the natural dust. Natural dust degraded the emissivity of the radiant barrier faster than the coarse Arizona Test Dust. The presence of soot, hydrocarbons and other natural pollutants with properties much different than the test dust, could be responsible for this larger than expected emissivity.

The correlation of the experimental results with the model developed in this research is the subject of the next section.

7. MODEL VALIDATION

7.1. Introduction

An evaluation of the performance of the model is performed in this section. The model developed in this research was validated using the experimental data gathered using the natural dust and the Arizona Road Test Dust. The validation was done in two forms: (1) using the dust coverage area-absorptivity data found in the electron microscope analysis and (2) using the dust loading-absorptivity data obtained with the natural dust and the test dust. Good agreement was found between the model and the experimental analysis. In this section, the relationship between dust loading, the barrier's absorptivity, and the barrier's effectiveness are evaluated.

7.2. Sensitivity Analysis

The model developed in section 5 was tested to determine its sensitivity with respect to different input parameters. The model was sensitive to the dust size distribution and dust density. The resulting absorptivity of the dusty radiant barrier varied from the absorptivity of the clean barrier to the absorptivity of the dust.

7.2.1. Sensitivity to the Dust Density

The model showed a dependence upon the dust density. This sensitivity was explained by the fact that low-density dust would cover more area of the radiant barrier than high-density dust. In Figure 7.1 it can be seen that the dusty barrier absorptivity increased when the dust density decreased.

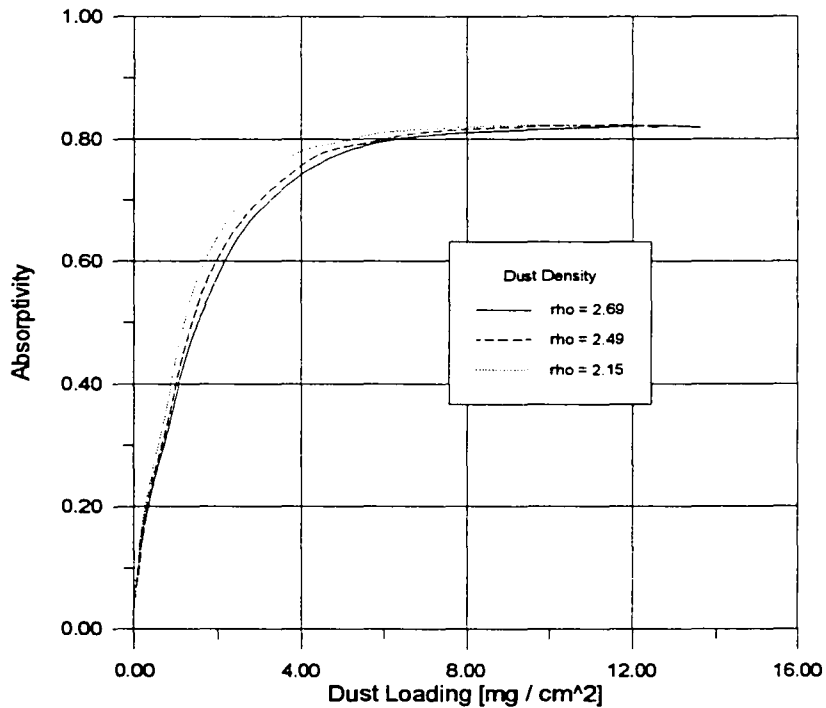


Figure 7.1. Absorptivity vs. dust accumulation with dust density as parameter.

7.2.2. Sensitivity to the Particle Size Distribution of the Dust

The model was sensitive to the particle size distribution of the dust. As explained earlier, the electron microscopic analysis showed that small particles tend to lay in between the other particles, thus effectively increasing the barrier's absorptivity. In contrast, large particles tended to overlap, which did not increase the area of dust coverage as rapidly. Figure 7.2 shows the absorptivity of the dusty radiant barrier as a function of the dust loading for both the fine and coarse dust.

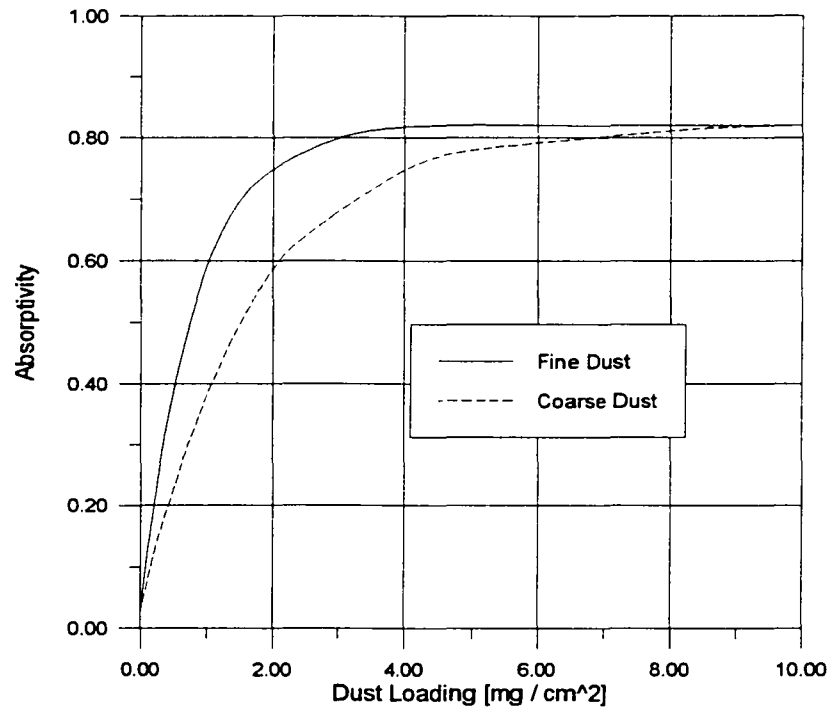


Figure 7.2. Absorptivity vs. dust loading for the coarse and fine dust.

7.3. Model Validation Using the Data of Fraction of Foil Area Covered by Dust

To compare the calculated absorptivity with the experimental data, the experimental fraction of area covered by dust, found using the electron microscope analysis, was used as input of the model to find a calculated absorptivity of the sample. The results were plotted in a X-Y plot against the experimental absorptivity of the sample. Figure 7.3 shows the results of this comparison for the barrier samples with natural dust. Figure 7.4 shows the same comparison for the barrier samples with Arizona Road Test Dust. Figure 7.5 shows all the data together.

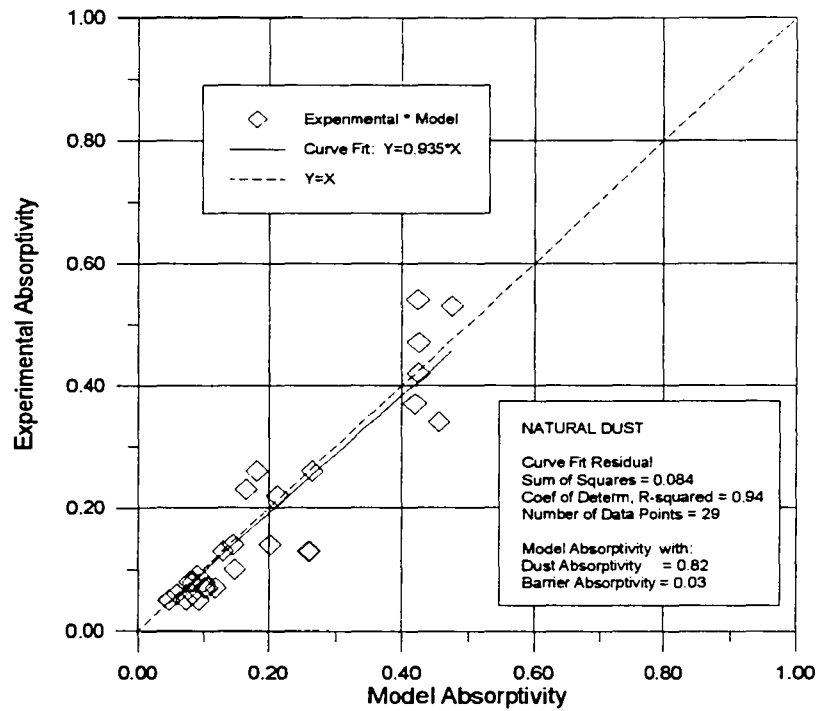


Figure 7.3. Experimental vs. calculated absorptivity for radiant barrier samples with natural dust.

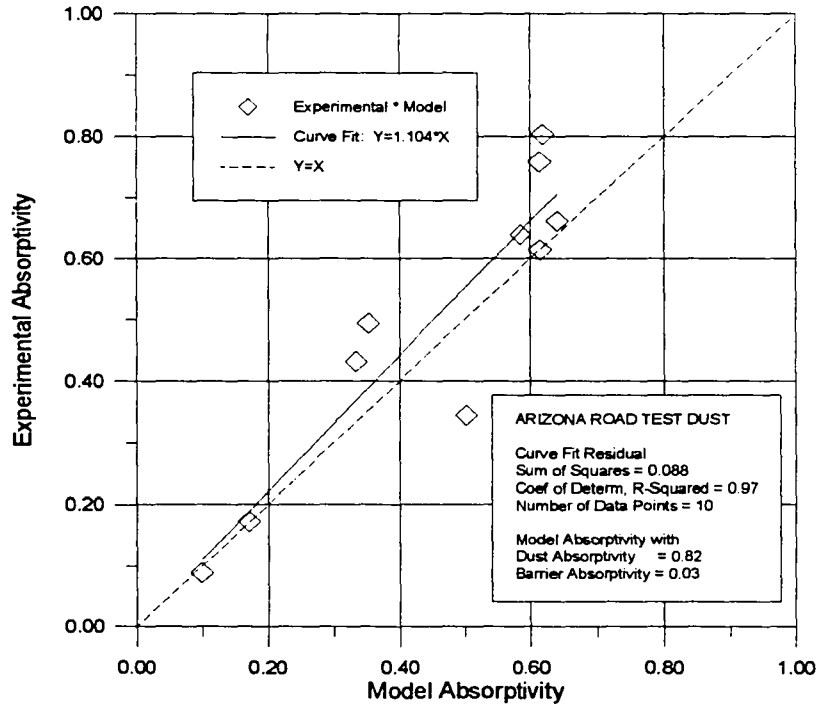


Figure 7.4. Experimental vs. calculated absorptivity for radiant barrier samples with Arizona Road Test Dust.

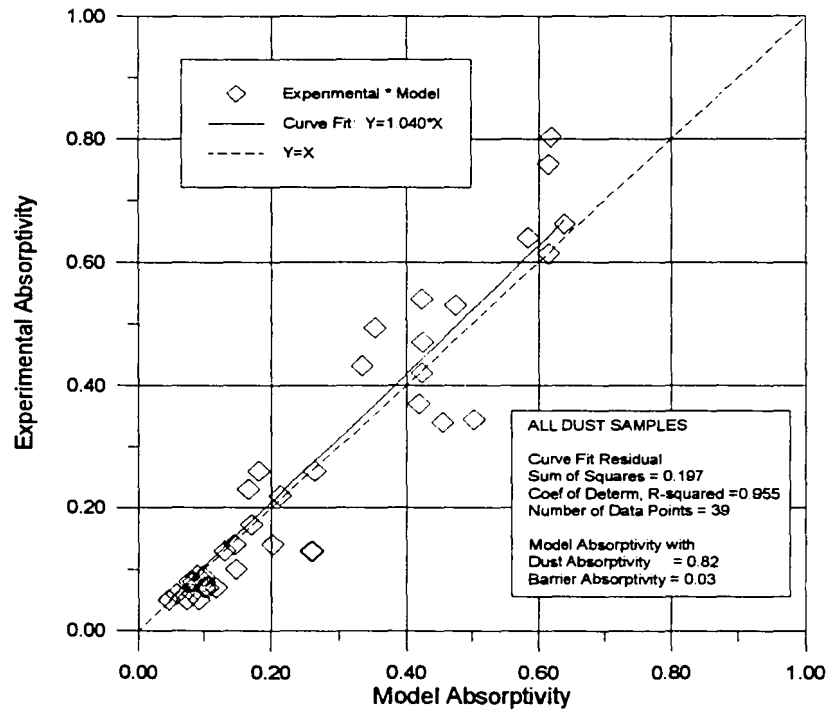


Figure 7.5. Experimental vs. calculated absorptivity for all the radiant barrier samples.

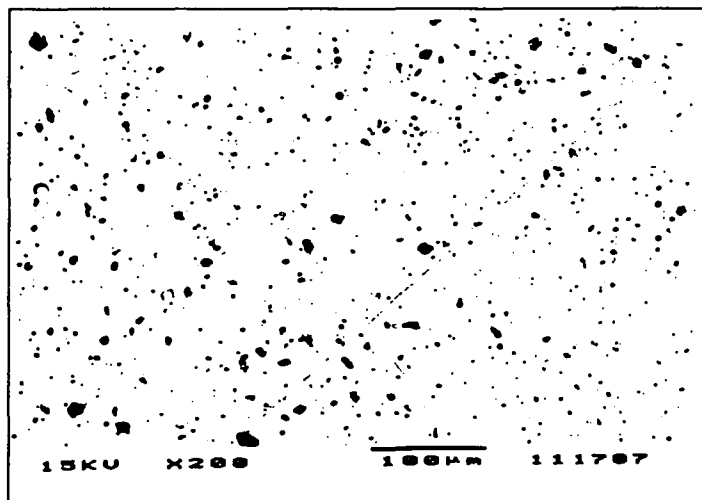
Figures 7.3 through 7.5 show the correlation between the experimental data and the calculated values, a curve fit of the data points to a straight line passing through the origin, and a line $X = Y$. The statistical data illustrate the good agreement between the experimental and the calculated values. R-squared was the square of the multiple correlation coefficient. For a one variable regression it was equivalent to the square of the correlation between the dependent variable and independent variable (Freund and Littell, 1991). In each case, the R-squared values obtained were greater

than 0.95. Figure 7.3 also shows that the Arizona Road Test Dust and the natural dust both degrade the absorptivity of the radiant barrier in a similar way, showing little difference in their radiative properties. Thus the Arizona road dust proved to be a good test material for the purposes of this research.

Some of the variation on the data corresponding to Figures 7.3 through 7.5 was attributed to the methodology followed to find the fractional area of foil covered by dust particles, which, as explained in paragraph 6.9.3, introduced an error of about 16 %.

The largest absorptivity of the barriers with natural dust was about 0.45, corresponding to a sample that had been collecting dust for about six years and two months (2272 days) in an attic in a College Station house. The lowest absorptivity corresponded to four samples collected from three different locations and with four months (123, 124, and 125 days) of dust collection.

Figures 7.6 through 7.9 show a graphical comparison of the experimental results using the electron microscope image and the model for two different dust loadings. The predicted values of fraction of foil covered by dust (f_p) and absorptivity were calculated as a function of the measured dust loading (L).



Sample #7
123 days of dust
accumulation.

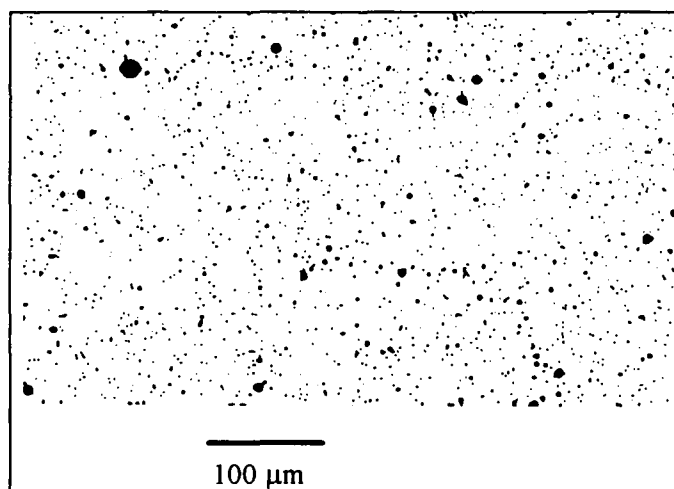
Measured:

$$L = 0.01 \text{ mg/cm}^2$$

$$\alpha_{\text{db}} = 0.05$$

$$f_p = 0.0218$$

Figure 7.6. Electron microscope photograph and measured loading, absorptivity and fraction of foil covered by dust for sample #7.



Simulation

$$n_p = 5,300$$

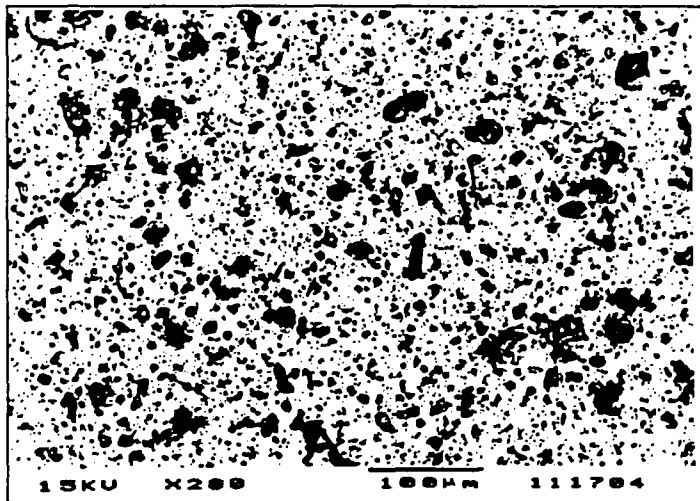
$$\text{Area} = 1 \text{ mm}^2$$

$$L = 0.01 \text{ mg/cm}^2$$

$$\alpha_{\text{db}} = 0.04$$

$$f_p = 0.014$$

Figure 7.7. Simulation of 5,300 dust particles with data of measured loading, calculated absorptivity and fraction of foil covered by dust.



Sample #5
2272 days of dust
accumulation.

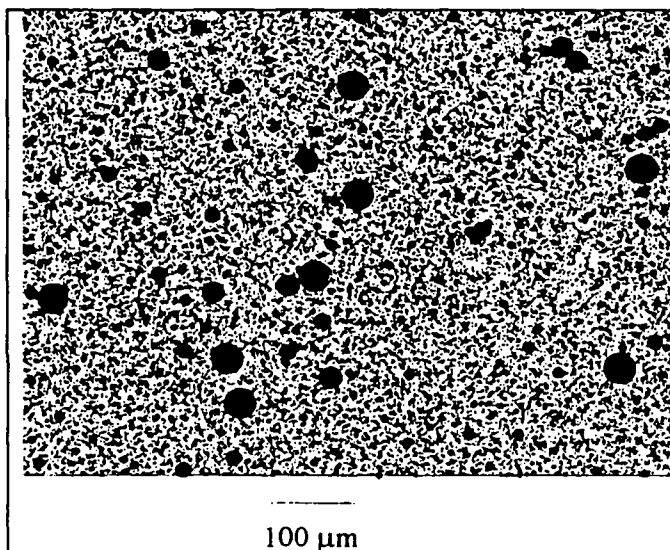
Measured:

$$L = 0.739 \text{ mg/cm}^2$$

$$\alpha_{\text{db}} = 0.46$$

$$f_p = 0.563$$

Figure 7.8. Electron microscope photograph and measured loading, absorptivity and fraction of foil covered by dust for sample #5.



Simulation

$$n_p = 138,500$$

$$\text{Area} = 1 \text{ mm}^2$$

$$L = 0.739 \text{ mg/cm}^2$$

$$\alpha_{\text{db}} = 0.39$$

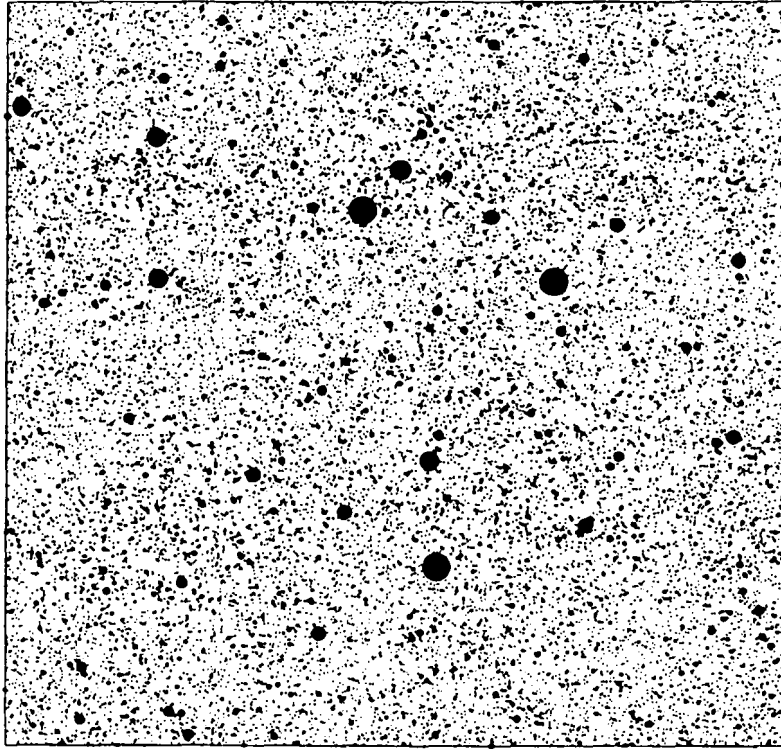
$$f_p = 0.421$$

Figure 7.9. Simulation of 138,500 dust particles with data of measured loading, calculated absorptivity and fraction of foil covered by dust.

Figures 7.6 through 7.9 show a comparison between the experimental and the model dust accumulation for two dust loadings, 0.01 and 0.739 mg / cm². The similarity between the photomicrograph and the model is apparent. In the electron microscope photographs there were more large size particles and less low size particles. This appearance was due in part to the resolution of the photographic film used in the image processing. Also, Figures 7.7 and 7.9 appeared darker than they actually were because the resolution of the printer used. The smallest particles (which are the majority) are smaller than what they appear relative to the larger ones. Also it is worth noticing that the largest particle in Figure 7.9, a 26.5 μm radius particle, covered an area equal to the area covered by 1433 particles with radius 0.7 μm. In the pictures, it was also possible to note that even though all the drawn particles were circles, due to the superposition, sometimes they appeared as irregular surfaces.

Figures 7.10 through 7.13 show the simulation of dust accumulation for an increasing number of particles from 20,000 to 80,000 particles. Tables 7.1 through 7.4 show the results of the model for the corresponding simulations. The sample size was one square millimeter and the corresponding fraction of foil covered by dust particles, loading and absorptivity are shown in the accompanying tables.

Figures 7.10 through 7.13 show the model representation of increasing dust loading. In this series of figures, one could notice the large difference in the probability of finding smaller size particles with respect to larger ones. It was not until the model placed 80,000 particles that one 37.5 μm particle appeared. In these figures, it was also possible to notice the much larger area that one large particle covered in comparison with the smaller particles.

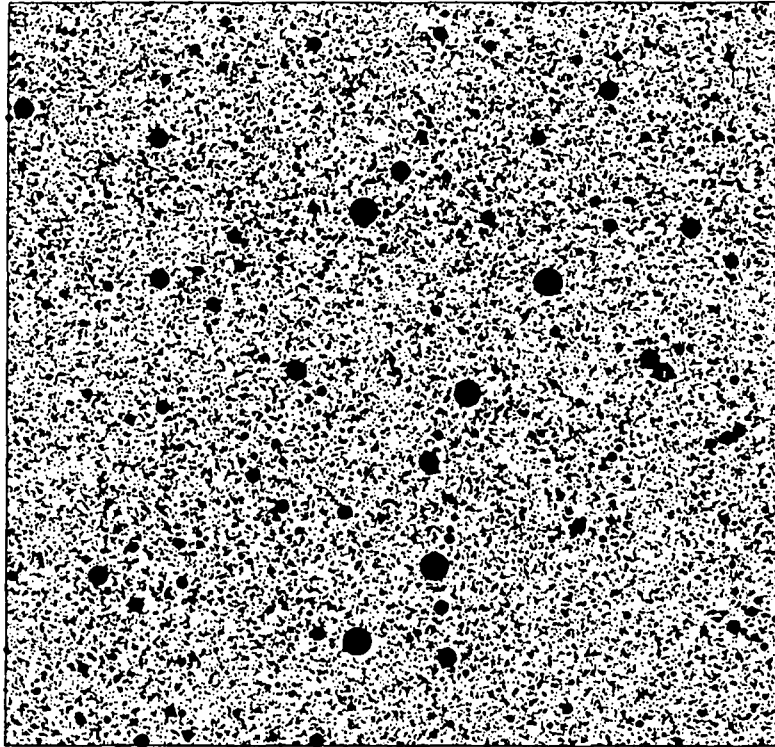


Coarse 100 microns

Figure 7.10. Simulation of 20,000 particles on top of a 1 mm² sample.

Table 7.1. Results of modeling 20,000 particles on top of a 1 mm² sample.

n_p	= 20,000
Area	= 1 mm ²
L	= 0.067 mg / cm ²
f_p	= 0.073
α_{db}	= 0.09

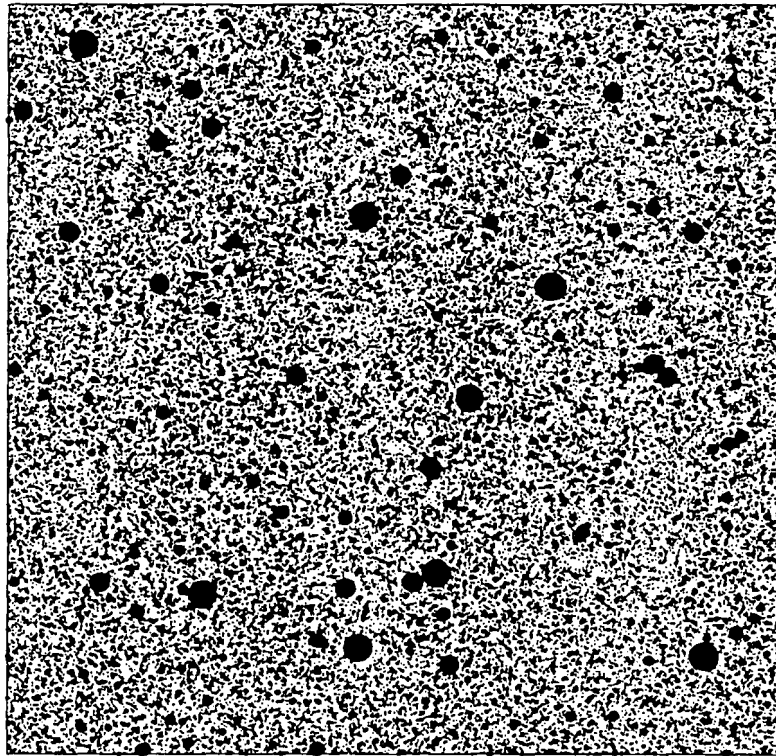


Coarse 100 microns

Figure 7.11. Simulation of 40,000 particles on top of a 1 mm² sample.

Table 7.2. Results of modeling 40,000 particles on top of a 1 mm² sample.

n_p	= 40,000
Area	= 1 mm ²
L	= 0.135 mg / cm ²
f_p	= 0.141
α_{db}	= 0.14

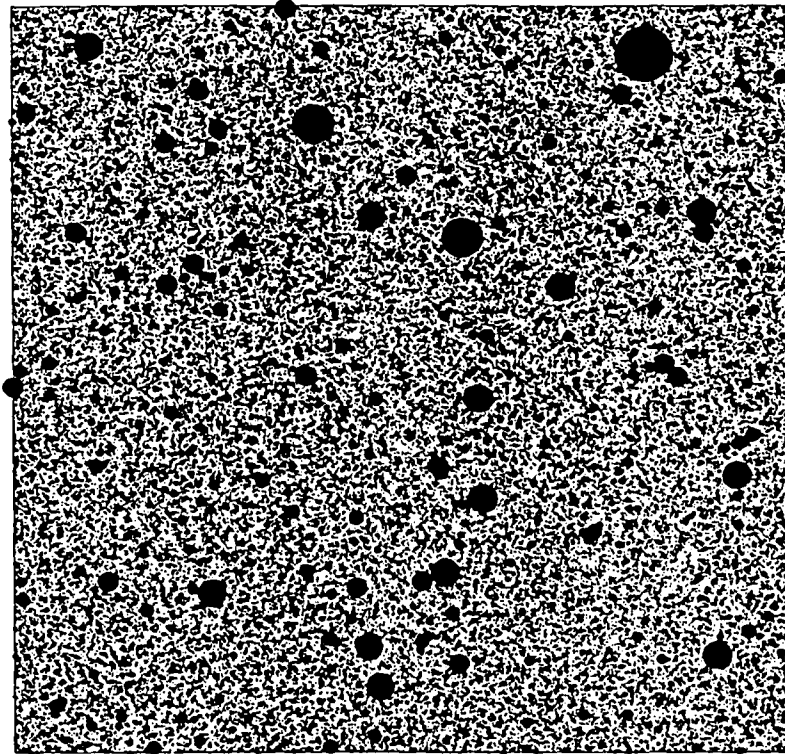


Coarse 100 microns

Figure 7.12. Simulation of 60,000 particles on top of a 1 mm² sample.

Table 7.3. Results of modeling 60,000 particles on top of a 1 mm² sample.

np	= 60,000
Area	= 1 mm ²
L	= 0.243 mg / cm ²
f _p	= 0.205
α _{db}	= 0.19



Coarse 100 microns

Figure 7.13. Simulation of 80,000 particles on top of a 1 mm² sample.

Table 7.4. Results of modeling 80,000 particles on top of a 1 mm² sample.

n_p	= 80,000
Area	= 1 mm ²
L	= 0.351 mg / cm ²
f_p	= 0.268
α_{db}	= 0.24

7.4. Model Validation with Dust Loading-Absorptivity Data

The results from the model developed in section 5 were compared with the experimental data obtained from the research. Figure 7.14 shows the comparison for the coarse dust. Even though the measured density was equal to 2.7 g / cm^3 , the model showed better agreement with the experimental data provided the dust density was set to 2.5 g / cm^3 . This correction factor agreed with the early finding made in section 3. The analysis made in that section showed that the assumption of the particles as plane circles underestimated the effective area of the particles to absorb and emit radiation by about 20 % which is in the range of the correction factor applied to the dust density.

Figure 7.14 shows the agreement between the model and the experimental data. The plot can be divided into three regions. In the first, which occurred at low dust loadings, the absorptivity increased fast with small increases of dust loading. This region was characterized by little overlapping of dust particles which led to a increase of the absorptivity (emissivity) by most of the particles deposited on top of the barrier. The second region was characterized by a decrease in the slope of the absorptivity versus loading curve. This region was the result of an increasing number of particles overlapping on top of each other. Thus, the rate of increase of the barrier absorptivity decreased. Finally, the third region occurred when most or all of the barrier's surface was already covered by dust. Any further addition of dust had little effect on the barrier absorptivity, and the absorptivity remained equal to the absorptivity of the dust.

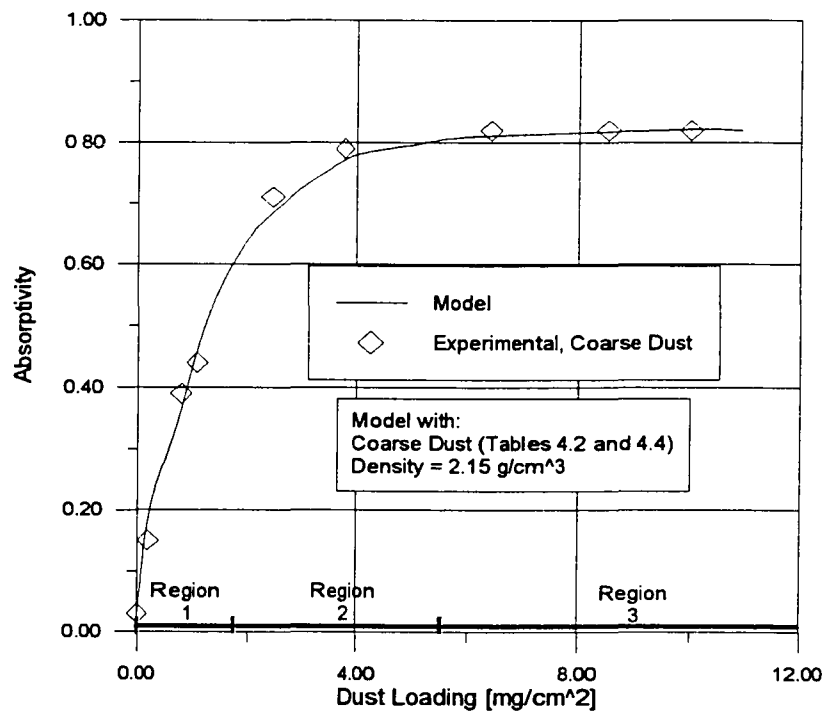


Figure 7.14. Comparison of experimental with predicted absorptivity vs. dust loading for coarse dust.

7.5. Comparison of the Present Model with the Early Model

Figure 7.15 shows a comparison of the experimental data with the prediction results using both the early (Noboa, 1991) and the present model. It can be seen that in the early model the absorptivity curve for small dust loadings, showed a linear increase because that model did not consider dust particle overlapping when the mean diameter was smaller than the distance between two adjacent nodes in the array (see section 3.4), whereas the present model does consider dust overlapping for any dust loading.

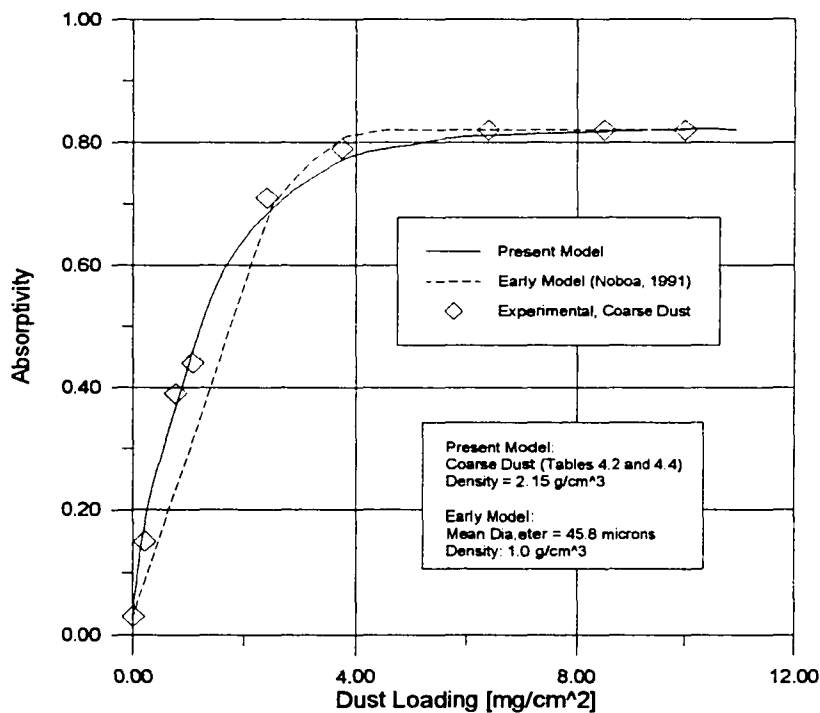


Figure 7.15. Comparison of experimental with predicted absorptivity vs. dust accumulation for coarse dust. Simulation using the early and the present models.

7.6. Dust Influence on the Radiant Barrier Effectiveness

The net effect of the dust deposited on top of the radiant barrier was to increase the barrier's absorptivity. This change led to the decrease of the radiant barrier's effectiveness as defined by Equation (2.1). To assess the influence of the dust

on the radiant barrier's effectiveness, the "Transient Heat and Mass Transfer Model of Residential Attics to Predict Energy Savings Produced by the Use of Radiant Barriers" (Medina, 1992) was used. A parametric study was conducted to find the ceiling heat load reduction as a function of the dust loading. The simulation used weather data from July 3 to July 6 of 1991 in Central Texas. Details of the experiments can be found in Medina (1992). Figure 7.16 shows the results of this study. Dust loading effects on both the barrier absorptivity and effectiveness were as expected: dust loading increased the emissivity of the barrier, which in turn decreased its effectiveness to reduce the ceiling heat flux.

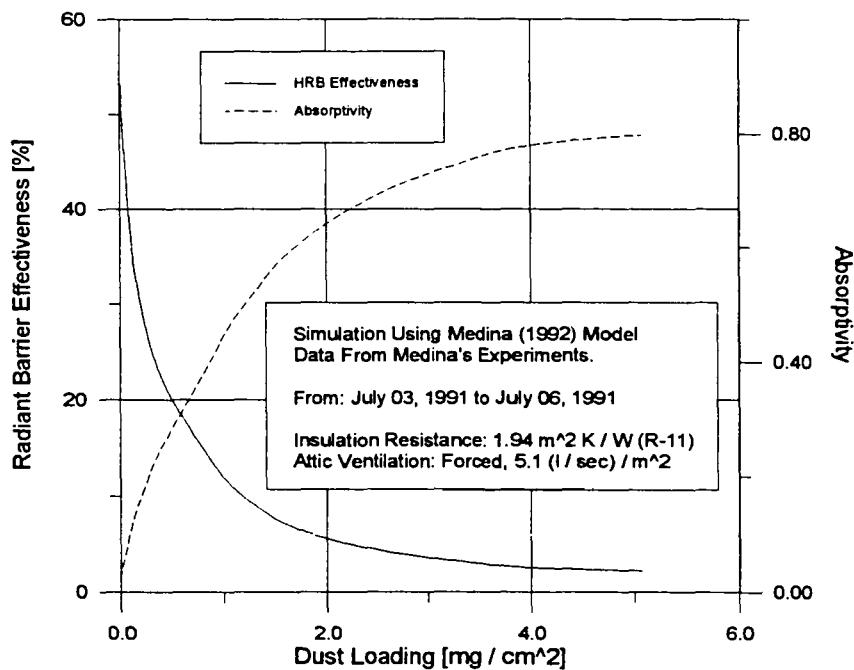


Figure 7.16. Radiant barrier effectiveness vs. dust loading.

This study showed that dust had a strong influence on the radiant barrier's effectiveness, in opposition to Hall's (1988a) remarks in which he stated that dust accumulation appeared to have very little effect on the radiant barrier's performance. Cooling season results indicated that the seasonal effectiveness of the radiant barrier dropped dramatically as the absorptivity increased as a result of the dust loading. For

example, a clean HRB installed on top of 8.9 cm. (3.5 in.) of fiberglass insulation had an effectiveness equal to 45 %. The seasonal effectiveness of the radiant barrier dropped to approximately 11% when the absorptivity increased to 0.46, corresponding to a dust loading of 1.06 mg / cm². The effectiveness of the radiant barrier decreased asymptotically to 1.85 % which is the effectiveness of the barrier having an absorptivity of 0.82, equal to the dust absorptivity.

7.7. Time Dependence on the Radiant Barrier Absorptivity

To study the temporal dependence of the change in the barrier's absorptivity, the absorptivity data were plotted against the elapsed time from the barrier installation on the attic. The data showed a linear trend. In the regression analysis it was possible to find a statistically significant correlation from the data to a linear model. The data were normalized with respect to the initial absorptivity of the clean radiant barrier to be able to fit the experimental data to a line crossing the origin. The result of this research is shown in Figure 7.8, and the statistical analysis is shown in Table 7.5.

Table 7.5. Regression analysis results of experimental vs. model absorptivities for all the barrier samples.

Fit 1: $Y=B*X$, through origin Equation: $Y = 0.000187981 * X$ Number of data points used = 32 Average X = 936.719 Average Y = 0.170938 Residual sum of squares = 0.109244 Coef of determination, R-squared = 0.940965 Residual mean square, $\sigma\text{-hat-sq'd}$ = 0.00352399

Table 7.5 shows that the statistics R-squared was equal to 0.94, indicating a strong linear correlation between the absorptivity change and the time.

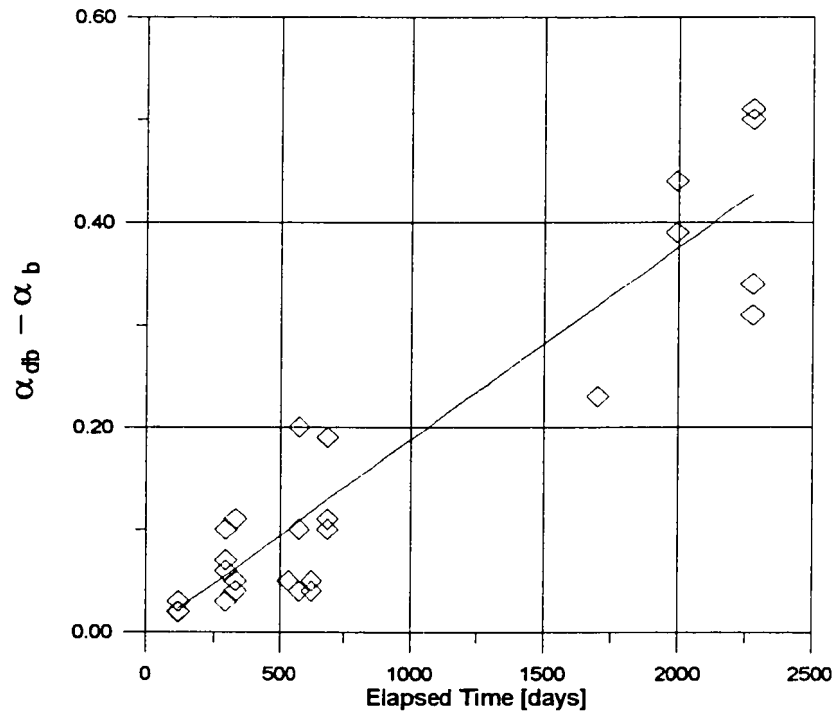


Figure 7.17. Change in absorptivity as a function of time.

7.8. Location Dependence on the Radiant Barrier Absorptivity

During the research it was clear that in attics with open vents, the barrier samples collected from locations near the vent of the attic were in general more heavily dusted than the samples away from the attic's vents. In closed attics, the samples collected about the same amount of dust in any location in the attic. Even though this trend was not very strong, Figure 7.18 shows that in the attic subject to analysis, in which the only vent was at the north side of the house, the samples collected near the vent were more likely to have an absorptivity higher than the mean for that time collection.

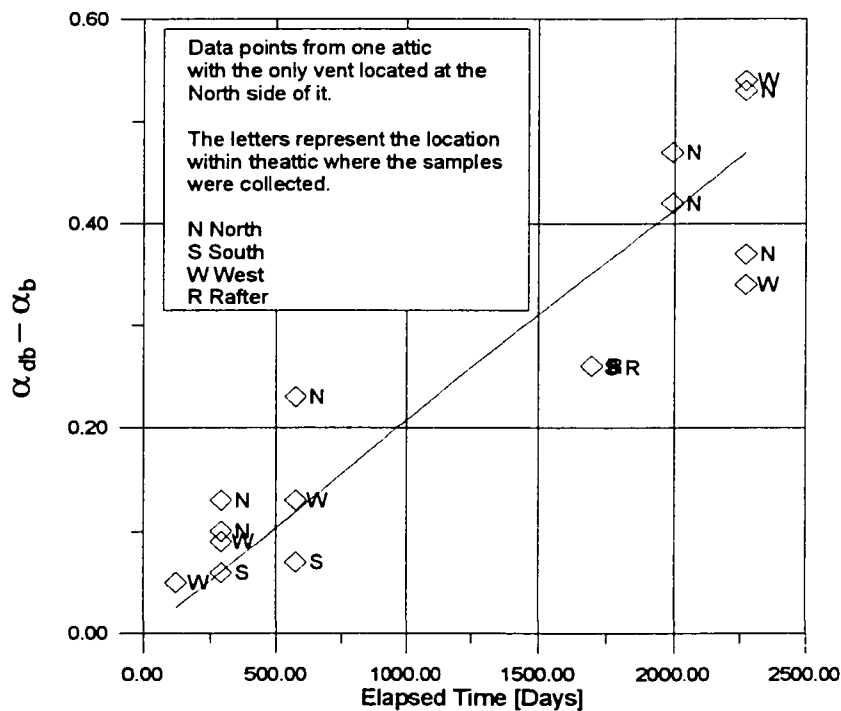


Figure 7.18. Location dependence on the radiant barrier absorptivity.

To explain why more dust accumulated on top of the samples near the vents of the attic, it was necessary to understand that the dust particles traveling with the air entering the attic were decelerated after entering the attic. The friction forces that hold large particles airborne dropped below the minimum necessary for the particles

to remain in the air. This caused them to fall near the entrance to the attic. Small particles, required much lower velocities to remain in the air. Thus, they traveled farther inside the attic before depositing on the barrier. Future research could be done to model the air velocity inside the attic, which would be useful to predict the patterns of dust accumulation inside the attic.

7.9. Summary

The comparison of experimental and calculated values of absorptivity using the measured fraction of foil covered by dust particles demonstrated that Equation (3.35) represented the natural phenomena accurately.

The model developed in section 5 was able to predict accurately the increase of the absorptivity of the horizontal radiant barriers due to dust accumulation on top of it. The model predicted that low-mass-density dust would increase faster the absorptivity than high-mass-density dust for the same dust loading expressed in milligrams of dust per square centimeter of barrier. The model could be used to predict the radiant barrier effectiveness as a function of the dust loading.

Using an empirical curve fit, it was also possible to correlate the time elapsed from the installation of the radiant barrier to a predicted absorptivity of the radiant barrier for a given geographical location. Similar correlations could be developed for any site, if the appropriate data is collected for each geographical location. This relationship could be used for long term analysis of the performance of the radiant barriers.

8. SUMMARY, CONCLUSIONS, AND RECOMMENDATIONS

8.1. Summary and Conclusions

The purpose of this project was to model and quantify the increase of the absorptivity of the radiant barrier due to dust accumulation. This model was needed to improve the prediction capability of existing computer programs to calculate the long term effectiveness of the radiant barriers. The degradation process of the radiant barrier properties could be quantified and correlated to the overall reduction of the thermal effectiveness of the building over time.

A literature review was conducted in which many confusing and sometimes contradictory concepts and remarks were found, for example the contradictory remarks of Hall (1988a) where he stated that dust accumulation appeared to have very little effect on the radiant barrier's performance. Yarborough (1987) was the first to quantify the effect of dust on the absorptivity of radiant barrier. Cook et al. (1990) in an experimental study, recognized the linear relationship expressed by Equation (3.35) between the fraction of barrier covered by the particles and the absorptivity of the barrier. Noboa (1991) went one step further to perform an energy balance in the attic enclosure. On the basis of the analytical work, he arrived to the same linear relationship, which has been a part of the theoretical foundation of this research.

This research was the continuation of previous work by the author at Texas A&M University as part of a Master's Thesis. A radiation energy balance inside the attic enclosure was developed, and the dust particles were treated as individual surfaces in the enclosure. That early model assumed that the dust particles lay in the nodes of a uniform array on top of the radiant barrier. The particles were treated as flat, circular planes, all having the same radii, and the energy analysis was carried out considering the Net Radiation Method as described by Siegel and Howell (1981). The solution of the system of equations led to the determination of the absorptivity of the dusty radiant barrier and further analysis of the results provided the analytical tools to develop Equation (3.35) from this analytical approach.

This work started by analyzing the assumptions made in the early work that applied to the new model. It was found that the assumption of treating the dust particles as plane circles underestimated the effective area of the particles by about 20 %. The model was corrected by using a scaling factor to the dust density which more closely matched the experimental data. Measurements made on a barrier with dust particles indicated that the dust particles achieved the same temperature of the radiant barrier. Thus, the assumption of the dust being at the same temperature as the barrier which was made in the early model was consistent with the data.

The present research pointed to two important limitations of the previous model. The model assumed all particles had the same diameter. Second, it was assumed that they were deposited in the nodes of a regular array on top of the radiant barrier. Both assumptions were corrected in the new model. Using Equation (3.35), the dust particles were simulated as flat circular planes having random radii and laying in random locations within the radiant barrier surface.

The new model calculated the fraction of radiant barrier area covered by particles using a digital array in which the clean barrier was represented as zeroes and the dust particles were represented as an orderly set of ones appropriately dimensioned inside the array. Dust particle superposition was in this way naturally achieved. The algorithm changed the zeroes representing clean barrier by ones, and if a particle came to lay on top of another particle, the ones remained as such. The model counted the number of ones in the array and the fraction of the radiant barrier area covered by dust was equal to the ratio of the total number of ones to the number of elements of the array.

The algorithm had to be made in a bit basis because the resolution needed in the model required that the array contained more than half a billion elements. This characteristic made the program somewhat more complicated, but utilized the full capacity of the machine to store and process the information.

The effect of dust on the absorptivity of the radiant barrier was as expected; larger amounts of dust applied to the barrier increased the absorptivity of the barrier so that the absorptivity of the barrier asymptotically approached the absorptivity of

the dust. The model predicted that the curves of absorptivity versus dust loading were different for the different types of dust. The prediction of the model agreed with the experimental data. For equal dust loadings, fine dust increased the absorptivity more rapidly than the coarse dust. This phenomena was explained by the fact that smaller particles have a greater probability of filling the spaces between particles, whereas large particles have a greater probability of overlapping.

The model showed that low-mass-density dust produced a higher radiant barrier absorptivity than high-mass-density dust for a given dust loading. This was explained by the fact that low-density dust covered more area than higher density dust.

An experimental procedure was developed to assess the model validity. The experimentation used natural dust collected upon radiant barrier samples located inside attics in the College Station area, in Central Texas and also used Arizona Road Test Dust, a commercially available dust commonly used to test air filters. The test dust proved useful for simulating natural dust in any loading. Using an infrared emissometer, the absorptivities of the clean and dusty barriers were measured and using an electronic scale, the dust loadings were measured.

An electron microscope was used to experimentally find the fraction of radiant barrier covered by the dust particles. Using Equation (3.35), the experimentally found absorptivity was correlated with the experimentally found fraction of dust coverage. Good agreement was found in this test. The experimental data were also used to test the model validity and a very good agreement was found in the absorptivity-dust loading relationship between the experimental and the model curves.

The limited experimental data available were also used to correlate the emissivity of the dusty radiant barrier with the time of dust accumulation. A linear relationship was found that can be applied to predict future barrier effectiveness based upon the rate of dust accumulation for a given location.

Finally, it was also found that in attics with vents, the radiant barrier near the openings of the attic accumulated more and larger particle dust than the barrier away

from the vents. This was explained by the ability of air to maintain dust particles in suspension. The larger the air velocities, the larger the size of the particles that can be traveling with the air stream. Once the air current enters the attic, it reduced its velocity to adjust to the dimensions of the attic. This effect in turn determined that the larger particles must fall down and deposit near the air intake. Smaller particles required lower air velocities to remain airborne, allowing them to travel larger distances inside the attic and covering every corner of the enclosure. Not enough data were collected to allow the development of a valid correlation. In attics without vents, no differences were found between the samples collected in different places of the attic.

The research was a contribution to help clarify early concepts about dust influence on the absorptivity (emissivity) of radiant barriers. It was shown that dust had a profound impact on both the radiant barrier absorptivity (emissivity) and the barrier's effectiveness to block the heat transfer inside the attic. With the rate of dust deposition observed in the Central Texas area of study, one could expect to find reductions on the barrier effectiveness of as much as 50 % in a 6 year period of time, if the radiant barrier is installed horizontally, and no cleaning is performed during that time (barrier used in conjunction with nine centimeters of fiberglass insulation).

The method to calculate the ratio of foil area covered by dust particles achieved a resolution that allowed the modeling of particles less than one micron in radius laying in a twenty five millimeter square barrier sample. This algorithm could be adapted to calculate areas of any shape with great precision.

One important recommendation in this matter is to use the truss-mounted radiant barrier instead of the horizontal barrier, because the truss radiant barrier does not accumulate dust; thus, the emissivity remains unchanged and the effectiveness of the barrier remains at a maximum over time.

8.2. Recommendations

There is a lack of knowledge of the dependence of the location of the barrier inside the attic and the pattern of dust accumulation on top of the radiant barrier. There is also a lack of knowledge of the dependence of time on the dust accumulation

and the absorptivity degradation of the radiant barrier. These deficiencies are because there is not enough understanding of the air movement and mixing inside the attic. It would be necessary to develop a mass and heat transfer model in three dimensions inside the attic to be able to predict the air velocity in all the points of the enclosure. This task does not seem trivial, but the solution of this problem would help to obtain more accurate modeling of the air velocities and this in turn would help to predict the dust distribution in the attic floor. The accurate prediction of the air velocities inside the attic would also improve the models of heat and mass transfer inside the attic to predict the energy savings due to the use of radiant barriers.

REFERENCES

ASHRAE, 1989, *Handbook of Fundamentals*, American Society of Heating Refrigeration, and Air Conditioning Engineers, Atlanta, GA.

Avallone, E. A., and Baumeister III, T., 1986, *Mark's Standard Handbook for Mechanical Engineers*, Ninth Edition, McGraw-Hill, New York, NY.

Bachman, L. R., 1985, "Rain on the Roof - Evaporative Spray Roof Cooling," *Second Annual Symposium on Improving Building Energy Efficiency in Hot and Humid Climates*, Texas A&M University, Energy Management Group, Department of Mechanical Engineering, pp. 195-202.

Cook, J. C., Jr., Yarbrough, D. W., and Wilkes, K. E., 1989, "Contamination of Reflective Foils in Horizontal Applications and the Effect on Thermal Performance," *ASHRAE Transactions*, VA-89-8-4, pp. 677-681.

Devices & Services Co., 1981, "Emissometer Model AE Operating Instructions," Devices & Services, Dallas, TX.

Energy Information Administration, 1991, "Annual Energy Outlook 1991 With Projections to 2010," Energy Information Administration, Office of Energy Markets and End Use, US. Department of Energy, Washington, DC.

Fairey, P. W., 1983, "Effect of Infrared Radiation Barriers on the Effective Thermal Resistance of Building Envelopes," *Proceedings, ASHRAE/DOE Conference on Thermal Performance of the Exterior Envelopes of Buildings II*, ASHRAE SP 38.

Fairey, P. W., 1985, "The Measured Side-by-Side Performance of Attic Radiant Barrier Systems in Hot, Humid Climates." *Proceedings, 19th International Thermal Conductivity Conference*, Cookeville, TN.

Fairey, P. W., Swami, M., and Beal, D., 1988, "RBS Technology: Task 3 Report (Draft)," Sponsored by Florida Power & Light Company and the U. S. Department of Energy, Florida Solar Energy Center, Cape Canaveral, FL.

Freund, R. J., and Littell, R., C., 1991, *SAS System for Regression*, Second Edition, SAS Institute Inc., SAS Campus Drive, Cary, NC.

Goldstein, J. I., Newburry, D. E., Echlin, P., Joy, D. C., Fiori, C., and Lifshin, E., 1981, *Scanning Electron Microscopy and X-Ray Microanalysis. A Text for Biologists, Material Scientists, and Geologists*, Plenum Press, New York, NY.

Goss, W. P., and Miller, R. G., 1989, "Literature Review and Predictions of Reflective Building Insulation System Performance, 1900-1989," *ASHRAE Transactions*.

Gregg, J. L., 1932, "Properties of Metal Foil as an Insulating Material," *Refrigerating Engineering*, May, pp. 279-283.

Hall, J., 1986, "Performance Testing of Radiant Barriers," *Third Annual Symposium on Improving Building Energy Efficiency in Hot and Humid Climates*, Texas A&M University, Energy Management Group, Department of Mechanical Engineering, pp. 57-67.

Hall, J., 1988(a), "Performance Testing of Radiant Barriers (RB) with R11, R19 and R30 Cellulose and Rock Wool Insulation," *Fifth Annual Symposium on Improving Building Energy Efficiency in Hot and Humid Climates*, Texas A&M University, Energy Management Group, Department of Mechanical Engineering, pp. 174-185.

Hall, J., 1988(b), "Radiant Barrier Testing to Assess Effects of Dust Accumulation, Attic Ventilation, and Other Key Variables." TVA Report TVA/OP/EDT--88/25, Tennessee Valley Authority, Office of Power, Division of Energy Demonstrations and Technology.

Hardy J. S., and Moon, J. W., 1989, "Roof Insulations," *Sixth Annual Symposium on Improving Building Systems in Hot and Humid Climates*, Texas A&M University, Energy Management Group, Department of Mechanical Engineering, Seminar Notes, pp. D17-D21.

Hughes Aircraft Company, 1991, "Probeye Thermal Video System Series 3000 Operation Manual," Hughes Aircraft Company Instrument Operation Manual.

Joy F. A., 1958, "Improving Attic Space Insulating Values," *ASHRAE Transactions*, Vol. 64, pp. 251-266.

Kahn, H., 1956, "Application of Monte Carlo," Report No. RM-1237 (AEC No. AECU-3259), Rand Corp., April.

Katipamula S., and O'Neal D. L., 1986, "An Evaluation of the Placement of Radiant Barriers on their Effectiveness in Reducing Heat Transfer in Attics." *Proceedings, Third Annual Symposium on Improving Building Energy Efficiency in Hot and Humid Climates*, Texas A&M University, Energy Management Group, Department of Mechanical Engineering, pp. 68-77.

Katipamula, S., O'Neal, D., Turner, W. D., and Murphy, W. E., 1987, "Experimental Study of Heat Transfer in Attics with a Small-Scale Simulator," *ASHRAE Transactions*, Vol. 93, pp. 122-134.

Katipamula, S., Turner, W. D., Murphy, W. E., and O'Neal, D. L., 1985, "Influence of Infrared Radiation on Attic Heat Transfer," *Second Annual Symposium on Improving Building Energy Efficiency in Hot and Humid Climates*, Texas A&M University, Energy Management Group, Department of Mechanical Engineering, pp. 211-217.

Lear, W. E., Barrup, T. E., and Davis, K. E., 1987, "Preliminary Study of a Vented Attic Radiant Barrier System in Hot, Humid Climates Using Side-by-Side, Full-Scale Test Houses," *Proceedings of the Fourth Annual Symposium in Improving Building*

Energy Efficiency in Hot and Humid Climates, Texas A&M University, Energy Management Group, Department of Mechanical Engineering, pp. 195-198.

Levins, W. P., and Hall, J. A., 1990, "Measured Effects of Dust on the Performance of Radiant Barriers Installed in Top of Attic Insulation," *ASHRAE Summer Meeting*, St. Louis, Missouri, June 24-28, CONF-9006117--3, DE90 008911, 26 p.

Levins W. P., and Karnitz M. A., 1986, "Cooling Energy Measurements of Unoccupied Single-Family Houses with Attics Containing Radiant Barriers," ORNL/CON-200, Oak Ridge National Laboratory, Oak Ridge, TN.

Levins W. P., and Karnitz M. A., 1987(a), "Heating Energy Measurements of Unoccupied Single-Family Houses with Attics Containing Radiant Barriers," ORNL/CON-213, Oak Ridge National Laboratory, Oak Ridge, TN.

Levins W. P., and Karnitz M. A., 1987(b), "Cooling Energy Measurements of Single-Family Houses with Attics Containing Radiant Barriers in Combination with R-11 and R-30 Ceiling Insulation," ORNL/CON-226, Oak Ridge National Laboratory, Oak Ridge, TN.

Levins W. P., and Karnitz M. A., 1987(c), "Energy Measurements of Single-Family Houses with Attics Containing Radiant Barriers," Presented at the ASHRAE Summer Meeting, Nashville, TN.

Levins W. P., and Karnitz M. A., 1988, "Heating Energy Measurements of Single-Family Houses with Attics Containing Radiant Barriers in Combination with R-11 and R-30 Ceiling Insulation," ORNL/CON-239, Oak Ridge National Laboratory, Oak Ridge, TN.

Levins, W. P., Karnitz, M. A., and Hall, J. A., 1990, "Cooling Season Energy Measurements of Dust and Ventilation Effects on Radiant Barriers," Oak Ridge National Laboratory, ORNL/M-1067, DE90 007190, February, 57 p.

Levins W. P., Karnitz M. A., and Knight D. K., 1986, "Cooling Energy Measurements of Unoccupied Single-Family Houses with Attics Containing Radiant Barriers," *Proceedings, Third Annual Symposium on Improving Building Energy Efficiency in Hot and Humid Climates*, Texas A&M University, Energy Management Group, Department of Mechanical Engineering, pp. 78-87.

Lotz, F. J., 1964, "The Effect of Dust on the Efficiency of Reflective Metal Foil Used as a Roof-Ceiling Insulation," *National Building Research Institute Bulletin 33*, Council for Scientific and Industrial Research Report #212, Pretoria, South Africa.

Mason, R. B., 1933, "Thermal Insulation with Aluminum Foil," *Industrial and Engineering Chemistry*, Vol. 25, No. 3, March, pp. 245-255.

McQuiston, F. C., Der, S. L., and Sandoval, S. B., 1984, "Thermal Simulation of Attic and Ceiling Spaces." *ASHRAE Transactions*, Vol. 90, Part I, pp. 139-163.

Medina M. A., 1992, "Development of a Transient Heat and Mass Transfer Model of Residential Attics to Predict Energy Savings Produced by the Use of Radiant Barriers," Ph. D. Dissertation, Texas A&M University, College Station, TX.

Medina M. A., O'Neal D. L., and Turner D. W., 1992(a), "Effects of Radiant Barrier Systems on Ventilated Attics in a Hot and Humid Climate," *Proceedings, Eight Annual Symposium on Improving Building Energy Efficiency in Hot and Humid Climates*, Texas A&M University, Energy Management Group, Department of Mechanical Engineering, pp. 47-52.

Medina M. A., O'Neal D. L., and Turner D. W., 1992(b), "Radiant Barrier Performance During the Heating Season," *Proceedings, Eight Annual Symposium on Improving Building Energy Efficiency in Hot and Humid Climates*, Texas A&M University, Energy Management Group, Department of Mechanical Engineering, pp. 53-58.

Nichols, P., 1921, "Air Space Transmission," *ASHVE Transactions*, pp. 783-790.

Noboa H. L., 1991, "Influence of Dust on the Emissivity of Radiant Barriers," Master's Thesis, Texas A&M University, College Station, TX.

Ober D. G., and Volckhausen T. W., 1988, "Radiant Barrier Insulation Performance in Full-Scale Attics with Soffit and Ridge Venting." *Proceedings, Fifth Annual Symposium on Improving Building Energy Efficiency in Hot and Humid Climates*, Texas A&M University, Energy Management Group, Department of Mechanical Engineering, pp. 174-185.

Peavy, B. A., 1979, "A Model for Predicting the Thermal Performance of Ventilated Attics," *Summer Attic and Whole House Ventilation*, NBS SP. 548, pp. 119-149.

Queer, E. R., 1932, "Importance of Radiation in Heat Transfer Through Air Spaces," *ASHVE Transactions*, Vol. 38., pp. 77-96.

Shad, L. W., 1931, "Insulating Effect of Successive Air Spaces Bounded by Bright Metallic Surfaces," *ASHVE Transactions*, Vol. 37.

Siegel, R., and Howell, J. R., 1981, *Thermal Radiation Heat Transfer*, Hemisphere Publishing Corporation, New York, NY.

Smith, J. L., and Smith, J. C., 1985, "Theory vs. Practice in Direct Evaporative Roof Spray Cooling," *Second Annual Symposium on Improving Building Energy Efficiency in Hot and Humid Climates*, Texas A&M University, Energy Management Group, Department of Mechanical Engineering, pp. 203-210.

Tripp, W., Hwang, C., and Crank, R. E., 1962, "Radiation Shape Factors for Plane Surfaces and Spheres, Circles or Cylinders," Special Report 16, *Kansas State University Bulletin*, vol. 46, no. 4., 23 p.

United States Bureau of Census, 1991, "Annual Housing Survey: Components of Inventory Change 1973-1983, United States and Regions. Current Housing Reports," PB91-238915, U. S. Bureau of Census, Washington, DC, Prepared for: Department of Housing and Urban Development, Washington, DC.

Weiss, E. L., and Frock, H. N., 1976, "Rapid Analysis of Particle Size Distributions by Laser Scattering," *Powder Technology*, 14, pp 287-293.

Wilkes, G. B., 1939, "Reflective Insulation," *Industrial and Engineering Chemistry*, Vol. 31, No. 7, July, pp. 832-838.

Wilkes, G. B., and Peterson, C. M. F., 1937, "Radiation and Convection Across Air Spaces in Frame Construction," *ASHVE Transactions*, Vol. 43, pp. 351-366.

Wilkes, G. B., Hechler, F. G., and Queer, E. R., 1940, "Thermal Test Coefficients of Aluminum Insulation for Buildings," *Heat, Piping, and Air Conditioning*, Jan., pp. 68-72.

Wilkes, K. E., 1988, "Modeling of Residential Attics with Radiant Barriers," *Fifth Annual Symposium on Improving Building Energy Efficiency in Hot and Humid Climates*, Texas A&M University, Energy Management Group, Department of Mechanical Engineering, pp. 161-168.

Wilkes, K. E., 1989, "Thermal Modeling of Residential Attics with Radiant Barriers: Comparison with Laboratory and Field Data," *Conference on Thermal Performance of the Exterior Envelopes of Buildings IV*, CONF-891202--2, DE89 016287, December 4-7, 31 p., Orlando, FL.

Wilkes, K. E., 1983, "Dynamic Thermal Performance of Walls and Ceilings/Attics," *Proceedings of the ASHRAE/DOE Conference on Thermal Performance of the Exterior Envelopes of Buildings II*, ASHRAE SP. 38, pp. 131-159.

Winiarski D. W., 1992, "A Quasi-steady State Model to Predict Attic Heat Transfer and Energy Savings in Residences Using Radiant Barriers," Master's Thesis, Texas A&M University, College Station, TX.

Yarbrough, D., Cook, J., and Wilkes, K., 1989, "Contamination of Reflective Foils in Horizontal Applications and Its Effect on Thermal Performance," *ASHRAE Annual Meeting*, Vancouver, BC, Canada, June 25-28, 1989. 20p.

VITA

Homero Luis Noboa was born on November 29, 1955 in Quito, Ecuador. He attended public school in Quito where he graduated from Colegio Benalcázar. He attended Escuela Politécnica Nacional of Quito, where he received a Bachelor of Science in Mechanical Engineering (Ingeniero Mecánico) in 1981. He attended Texas A&M University where he received a Master of Science degree in Mechanical Engineering in 1991. He works for Escuela Politécnica Nacional, Mechanical Engineering Department of Quito since 1980 where he lectures in Thermal Sciences. Homero Noboa is married to the former Mónica Pazmiño and they have two children, Anita María and Felipe Homero. His permanent address is: San Gabriel 241 y Carvajal, La Granja. Quito-Ecuador.